ABSTRACT

Title of Dissertation: THE ROLE OF SOIL HYDRO-PHYSICAL PROPERTIES IN LAND-ATMOSPHERE INTERACTIONS AND REGIONAL CLIMATE

Eli Dennis
Doctor of Philosophy, 2021

Dissertation Directed by: Dr. E. Hugo Berbery
Department of Atmospheric and Oceanic Science

Soil hydro-physical properties are necessary components in weather and climate simulation; yet, the parameter inaccuracies introduce considerable uncertainty in the representation of surface water and energy fluxes. The surface fluxes not only affect the terrestrial water and energy budgets, but through land-atmosphere interactions, they can influence the boundary layer, atmospheric stability, moisture transports, and regional precipitation characteristics. This set of three experiments explores aspects of soil hydro-physical properties, and their impact on coupled regional climate simulations in the North American region.

In the first two experiments, two soil datasets are considered: State Soil Geographic dataset (STATSGO) and Global Soil Dataset for Earth System Modeling (GSDE). Each dataset's dominant soil category allocations differ significantly at the model's resolution. Large regional discrepancies exist in the assignments of soil category, such that, for instance, in the Midwestern United States, there is a systematic reduction in soil grain size. Because the soil grain size is regionally biased, it allows

for analysis of the impact of soil hydro-physical properties projected onto regional scales.

In the first experiment, in areas of reduced soil grain size, there is also a reduction in latent heat flux and an increase in sensible heat flux following the physical understanding of soil properties. These differences in surface fluxes affected low-level thermodynamics, and PBLH. The second experiment analyzed soil-induced differences in the general circulation, emphasizing horizontal moisture transports, vertically-integrated moisture flux convergence, and regional precipitation. It found that soil-induced differences in surface fluxes influenced each term of the atmospheric water budget via both thermodynamic and dynamic means.

The third experiment assesses the impact of soil hydro-physical parameters on surface fluxes, and the atmospheric response. The default soil hydro-physical parameter table is replaced with a modernized soil parameter table. The findings indicate that the role of each soil hydro-physical parameter is sensitive to both climatic regimes (i.e., arid vs. temperate), and vegetation assignment.

Collectively, this series of experiments improves our understanding of the physical mechanisms that link the soil to the atmosphere in the coupled land-atmosphere system. The improved understanding will inform the development of the next generation of land surface models.

THE ROLE OF SOIL HYDRO-PHYSICAL PROPERTIES IN LAND-ATMOSPHERE INTERACTIONS AND REGIONAL CLIMATE

by

Eli Dennis

Dissertation submitted to the Faculty of the Graduate School of the
University of Maryland, College Park in partial fulfillment
of the requirements for the degree of
Doctor of Philosophy
2021

Advisory Committee:
Res. Prof. E. Hugo Berbery, Chair/Advisor
Prof. Eugenia Kalnay
Prof. Da-lin Zhang
Asst. Prof. Jon Poterjoy
Dr. Alfredo Ruiz-Barradas
Prof. Michael Evans, Dean's Representative

Acknowledgments

I would like to acknowledge and sincerely thank my advisor Dr. E. Hugo Berbery. Without his knowledge, patience, and guidance, this degree would not have been possible. I will carry many of his lessons forward in my career, and I hope to embody his uncompromising attention to detail in my future endeavors. I would like to thank my parents for their undying love and support, even though I'm still not positive they know what I study or how I study it. They are always behind me no matter what happens. And, lastly, I would like to thank my wife, Katie Dennis, for her love and patience during this process. It's hard to be married to a PhD student, (let's see how she likes being married to a post-doc..), but she has dealt with my strange schedule, periodic frustration, and long journey with grace, compassion, unending support, and love, which I will try forever to return.

Table of Contents

List of Tables

List of Figures

Chapter 1: General Introduction

1.1 Background

The land surface is intertwined with the atmosphere through the water and energy cycles [Sorooshian et al., 2005], and soil moisture is fundamental to understanding these physical relationships. Persistent soil moisture anomalies (or "soil moisture memory") can serve as a source of atmospheric predictability [Song et al., 2019]. It allows the land surface to retain characteristics of past precipitation events, and use them to influence future precipitation events [Dirmeyer et al., 2009; Sörensson and Berbery, 2015; Yang et al., 2018].

In general, reduced soil moisture leads to reduced latent cooling and increased surface temperatures [Fischer et al., 2007; Santanello et al., 2011]. High air temperatures then lead to drying soils by increasing the evaporative demand. Through this mechanism, land–atmosphere (L-A) interactions can impact drought persistence [Roundy et al., 2013; Roundy and Wood, 2014], and lead to the initiation, maintenance, or demise of heat waves [Dirmeyer et al., 2021].

Land-atmosphere interactions and coupling can lead to sustained, enhanced or more frequent precipitation events, as well. A moist land surface with ample soil moisture can experience high levels of ET, saturating the boundary layer and

lowering the LCL and the LFC creating an environment more conducive to initiation of convection [Dirmeyer et al., 2009; Gentine et al., 2013]. However, dry soils can also lead to increased convection. Dry soils correspond to increased sensible heat flux. Increased sensible heat flux instigates turbulent eddies, which cause the PBL to grow. If the PBL grows sufficiently to intersect the LFC, convection can be initiated [Weckwerth and Parsons, 2006; Ziegler and Rasmussen, 1998]. Additionally, the land surface, through L-A interactions, can maintain and even enhance land falling hurricanes leading to prolonged emergency scenarios [Andersen and Shepherd, 2014; Nair et al., 2019; Shepherd et al., 2021].

It has been shown that L-A interactions occur preferentially in certain regions, but among an ensemble of global climate models (GCMs) representing these processes, large variability is found [Koster et al., 2004]. Land-atmosphere coupling in both regional climate models (RCMs) and GCMs is shown to be sensitive to choice of parameterizations and the interplay between model components and parameter tuning [Dirmeyer et al., 2006]. Recently, it has been shown that some this variability could be related to model-specific configurations, such as GCM resolution [Müller et al., 2021], or land cover definition [McDermid et al., 2019; Singh et al., 2018]. Land surface properties alter the partitioning of surface fluxes, affecting the overlying atmosphere (exchange of heat, moisture, momentum, turbulence, stability, and dynamics) [Gentine et al., 2010, 2011, 2013]; therefore, they too influence variability in representing L-A interactions.

Despite substantial improvements in land surface modeling capabilities over the last two decades, many common land surface models remain dependent on

empirically-derived parameters, some of which are both poorly observed in nature and not scale-aware. Recognition of the role of land surface properties via discussion of land use and land cover change (LULCC) has been well-documented [i.e., Mahmood et al., 2010], leading to a Chapter in the latest IPCC Special Report [Jia et al., 2019]. Land use-Land cover changes have been shown to influence precipitation [Chen et al., 2017; Lee et al., 2018], extreme heat events and droughts [Findell et al., 2017; Hirsch et al., 2015], and the general circulation [Lee and Berbery, 2012; Lee et al., 2013]. These studies have mostly focused on the role of surface parameters like albedo and surface roughness that are associated with changing the land cover. However, some of the most impactful and hydrologically-relevant parameters are those associated with soil physics [Cuntz et al., 2016], which have received less attention. Through their physical properties, soils control the vertical and horizontal movement of water beneath the surface. They can retain moisture, thus restricting root uptake and the resulting evapotranspiration. By doing so, they strongly influence the distribution of soil moisture and soil moisture availability near the surface and at deeper levels. Therefore, it is necessary to improve our understanding of the physical processes related to linking soil properties to surface fluxes and L-A interactions.

1.2 Objectives

This work is aimed at investigating the role of soil hydro-physical parameters in land-atmosphere coupling and regional climate. Uncertainty related to the rep-

resentation of soil processes in coupled land surface modeling stems from multiple sources, including: soil texture assignment in each grid space, and soil hydro-physical parameter variability. These sources of uncertainty are discussed with more comprehensive and specific background and context at the beginning of each chapter, but the general objectives are as follows:

- Improve our understanding of the physical processes that link soil hydro-physical properties to L-A coupling (Chapters 2–4).
- Investigate the role of soil texture class assignments in local thermodynamic coupling (Chapter 2).
- Explore the dynamic implications of changing soil texture assignments on integrated atmospheric moisture transports and the atmosphere water budget (Chapter 3).
- Examine the variability in empirically-derived soil hydro-physical parameters, and evaluate the sensitivity of the coupled L-A system to changing those parameters (Chapter 4).

The experiments in the subsequent chapters utilize limited-area regional climate model simulations to test the coupled land-atmosphere system sensitivity to choices of soil parameters. Coupled modeling will always present certain challenges. It is useful for testing the responses of complex non-linear systems to small changes in parameters or in conditions, but it cannot be done without some uncertainty. A different approach would be to use an uncoupled land surface model, however, these

experiments attempt to address the coupled implications specifically, necessitating a coupled strategy. Like many questions in science, these experiments would benefit from supplementary projects utilizing both uncoupled land surface model simulations, as well as, coupled global model simulations. It is often best to approach questions from multiple angles. That being said, the contributions made through these experiments are focused on the responses of the coupled land-atmosphere system to changes in how soils are represented.

The following chapters represent published work (Chapter 2), work that is undergoing peer-review (Chapter 3), and work that is in late-stage production (Chapter 4). Chapter 5 will present our final thoughts and future directions.

Chapter 2: The Role of Soil Texture in Local Land–Atmosphere Interactions

The work in this chapter has been published in the Journal of Hydrometeorology as Dennis and Berbery [2021].

2.1 Introduction

It has long been understood that the land surface is a critical component of the climate system and that soil moisture is a key factor for determining land surface–atmosphere interactions and coupling [Koster et al., 2004; Sellers et al., 1996; Seneviratne et al., 2010]. The strength of the coupling between soil moisture and other variables depends on the time scale, ranging from daily-to-weekly time scales [Santanello et al., 2011; Tawfik and Dirmeyer, 2014], to monthly–to–annual timescales [Dirmeyer, 2011; Roundy and Wood, 2014], and extending into climate scales [Koster et al., 2006; Seneviratne et al., 2010]. Similarly, land surface–atmosphere coupling depends on the spatial extent of a phenomena, ranging from local-scales [Santanello et al., 2018] to basin-scales [Betts, 2009; Ferguson et al., 2012; Weaver, 2004]. Soil moisture affects the partitioning of surface energy fluxes that control the vertical stability and the evolution of the planetary boundary layer (PBL).

In certain synoptic regimes, the effects of soil moisture have been shown to modify the quantity and timing of precipitation events [Baur et al., 2018; Song et al., 2015; Welty and Zeng, 2018]. For instance, increased precipitation may result from wet soil conditions, in which, enhanced latent heat flux (LHF) will moisten the boundary layer, thereby reducing the height of the LCL. If the LCL and LFC lower sufficiently that they intersect the PBL, convective precipitation can be triggered [Aires et al., 2013; Findell and Eltahir, 2003; Gentine et al., 2013; Song et al., 2015]. Yet, dry soil conditions can also trigger convective precipitation, via thermal eddies interacting with the appropriate mesoscale boundaries such that surface-based parcels intersect the level of free convection (LFC) and initiate localized convection [Gentine et al., 2013; Holt et al., 2006a; Weckwerth and Parsons, 2006]. Whether an increase in soil moisture leads to increased or decreased precipitation depends on spatiotemporal scales, season, and region.

Soil moisture, which may feedback into future precipitation events, can provide a 'memory' of past precipitation events, thus presenting potentially useful information regarding seasonal-to-interannual variability and prediction [Koster et al., 2000]. Further, certain regions are predisposed to stronger influence of the land surface relative to other precipitation forcing mechanisms [Dirmeyer and Halder, 2017; Koster et al., 2004; Luo et al., 2007]. While the distribution of soil moisture is crucial to simulating the processes at the land surface, the states and changes of soil moisture are strongly dependent on the soil hydro-physical properties. These properties, as well as properties related to vegetation, control the evolution of soil temperature and evapotranspiration (ET), as well as the quantity and timing of runoff.

State-of-the-art LSMs, running in either uncoupled or coupled mode, contain extensive functionality to include the effects of hydrology, biology, chemistry and radiation that are important to simulating weather and climate [Kennedy et al., 2019; Kumar et al., 2006; Lawrence et al., 2019; Niu et al., 2011]. Analysis of four modern LSMs using the NLDAS-testbed [Xia et al., 2013] reveal that each model has both strong attributes and shortcomings. Specifically, the Variable Infiltration Capacity (VIC) had the best performance reproducing observed streamflow, the Community Land Model version 4 (CLMv4) indicated an increased ability to partition ET into components, and the Noah-Multiple Physics (Noah-MP) provided improved soil moisture variability [Cai et al., 2014]. Other studies have compared performance regarding individual components of the hydrological cycle: streamflow [Bai et al., 2016; Xia et al., 2012], ET [Lawrence et al., 2007; Nearing et al., 2016; Robock et al., 2018; Xia et al., 2015], soil moisture [Godfrey and Stensrud, 2008; Nearing et al., 2016; Zhuo et al., 2019], and additionally, performance related to local land–atmosphere interactions [Santanello et al., 2012], and climate-scale soil moisture-precipitation interactions [Dirmeyer et al., 2006; Ferguson et al., 2012]. Every available LSM is imperfect, but each can provide utility in analyzing land surface behaviors. Many of the LSM shortcomings can be related to the large number of parameters required to represent both soil and vegetation processes, which are often poorly constrained by observations and not scale-aware. Because soil properties are difficult to define, lookup tables have been constructed to provide mean soil hydraulic properties for each USDA soil type. In this way, only the percent sand, silt, and clay is needed for regional to global simulations.

To accurately account for land surface processes, LSMs require the prescription of empirically-derived soil hydro-physical properties based on soil texture (i.e., the proportions of sand, silt, and clay). The identification of soil texture categories originated from a need to group soils with similar properties by subjective mechanical analysis, (i.e., grain size and feel), for consistency in agriculture [Davis and Bennett, 1927; Hobbs, 1941]. Similar classes are still used at present for lack of more detailed in-situ measurements. Regional and global databases containing gridded values of sand, silt, and clay have been constructed using a combination of campaigns to survey soil profiles and statistical procedures [Chaney et al., 2019; Hengl et al., 2017].

The use of a soil texture map paired with a lookup table is a practical solution for enabling large scale land surface modeling and a standard practice at operational forecast centers either coupled or uncoupled. The lookup table is an important constraint since it assumes a uniform hydraulic behavior for each soil category anywhere in the world. In recent years, the soil sciences community has been working intensely to advance the development of Pedotransfer Functions (PTFs) that should improve current simplifications of soil processes [PTFs; see van Looy et al., 2017, for a review]. PTFs vary markedly in complexity; some use advanced mathematical techniques like machine learning and neural networks, while others use physically-based relationships that allow soil properties to more accurately reflect the environmental conditions. Advanced versions of the PTFs are being developed which will improve the representation of water flow through the intricate soil-vegetation system.

Soil hydro-physical properties vary widely within each soil texture category

(especially, as a function of the type of clay present), and there is significant uncertainty in the PTF-derived parameters themselves, suggesting that both the soil hydro-physical parameter values and the soil texture categorizations are imperfect [He et al., 2016]. Conventional ground-based measurements of soil properties become unrealistic at regional to global scales due to the meter-scale variability of soil properties [Montzka et al., 2017]. Organic carbon is an additional factor exhibiting a strong influence on the soil-water interface [Lannoy et al., 2014; Rawls et al., 2003]. Further, Duan et al. [2006] question the transferability from one region to another of a priori parameter estimation techniques used for many LSM parameters—questions which extend to include soil hydro-physical parameters, but also to include vegetation parameters, which can be just as important as soil hydro-physical parameters.

Differences in soil texture category assignments yield related differences in the empirically-derived hydro-physical parameters assigned to each category. Because the soil hydro-physical parameters exhibit strong controls on the evaporative fraction [Betts and Ball, 1995; Dy and Fung, 2016; Seneviratne et al., 2010], the classification of soil type can be critically important to the land–atmosphere interactions. However, soil hydro-physical properties are not the only parameters or mechanisms that dictate the behavior of the land surface. Vegetation plays an important role in determining surface characteristics: it modulates the albedo, intercepts falling water, shades the soil, the roots interact with the soil, and it directly impacts transpiration.

While studies like Nearing et al. [2016] have shown that prediction uncertainties due to the forcing data are larger than uncertainties due to model parameters, the uncertainties in soil texture estimation need to be assessed. If properties as-

sociated with soil texture drive the availability of soil moisture, and soil moisture affects the magnitude and timing of SHF and LHF, then, it is hypothesized that soil texture could also influence the evolution of the PBL and atmospheric stability. Given that important differences exist between soil texture databases, the impacts of using one versus another on simulated ET and sensible weather forecasts should be understood and quantified. Accordingly, there is a need to know the spatial distribution of soil classification uncertainty.

In this study, we compare the results of two WRF simulations with different soil classification datasets: the State Soil Geographic (STATSGO) dataset from USDA [NRCS Soil Survey Staff, USDA, 2012] and the Global Soil Dataset for use in Earth System Models (GSDE) from Beijing Normal University [Dai et al., 2019b; Shangguan et al., 2014]. The goal is to investigate the physical processes that link soil texture to the surface and near-surface states and fluxes influencing PBL height (PBLH) evolution and their sensitivity to soil texture classification. The experimental methods and the specific differences in available soil texture databases will be discussed in Section 2. Section 3 will focus on the soil texture-induced thermodynamic differences in the modeled climate in two contrasting regions. Section 4 will present our concluding remarks.

2.2 Data and Methods

2.2.1 The model setup

The Weather, Research and Forecasting–Advanced Research (WRF-ARW) Model version 3.9 [Skamarock et al., 2008] is employed to test and evaluate the role of soil texture in regional climate. WRF is a non-hydrostatic, full-physics numerical weather prediction model commonly used in similar research applications. The model was configured with a 15-km horizontal grid spacing and 51 vertical layers; thirteen of which are clustered in the lowest one kilometer to ensure a better representation of the PBL structure and dynamics. To realistically represent the surface layer, the lowest model level is close to 10 m AGL (i.e., the level of commonly observed winds), which is helpful for improving the realism of the surface layer [Zhang and Wang, 2003; Zhang et al., 2014].

The LSM coupled to WRF for this experiment is the Community Land Model version 4 [CLM; Lawrence et al., 2011] available from NCAR. CLM is a widely-used LSM originally developed to be used either coupled to the Community Earth System Model (CESM) or in stand-alone (uncoupled) mode. It has since been converted for use with other NWP models, such as WRF. CLMv4 has 10 vertical soil levels increasing in thickness with depth. The WRF version of CLM can accept up to 4 independent soil columns per grid space. This is different from the version of CLM directly from NCAR, which is designed to incorporate a telescoping structure (i.e., multiple plant functional types inside one soil column, multiple soil columns inside

one land use category, and multiple land use categories per grid space). Instead, some of that functionality was removed in WRF to make it compatible with the WRF Preprocessing System (WPS) (K. Oleson 2019, personal communication).

The passage of water within the soil column is controlled by a version of Richard's Equation. CLM handles vegetation within the context of the water cycle and the radiation budget in very fine detail including the effects of canopy shading, albedo, carbon chemistry, phenology, root density and depth, among others. Zhuo et al. [2019] compare CLM, Noah, and Noah-MP functionality and structure, (summarized in their Table 1). CLM is favorable in terms of number of active soil layers, deeper active soil layers, and greater heterogeneity per grid space. For a complete description, see the CLM User Guide [Oleson et al., 2010].

The PBL scheme for each simulation is MYNN2, a second-order closure, local PBL scheme [Nakanishi and Niino, 2006] along with the compatible MYNN surface layer scheme. Due to the horizontal grid spacing, a convective parameterization is necessary—the Betts Miller Janjić (BMJ) was selected [Janjić et al., 2001]. Other parameterizations include the single-moment Thompson microphysics scheme [Thompson et al., 2008], and the Rapid Radiation Transfer Model [RRTM; Iacono et al., 2008]. The horizontal domain covers the majority of North America, as well as Central America (See Figure 1). The boundary condition data are taken from the GFS Final Analysis (GFS-FNL) [for Environmental Prediction/National Weather Service/NOAA/U.S. Department of Commerce, 2015] at 6-hour intervals.

Model output for each simulation is written at 3-hourly intervals for 92 days, over 3 summers: 1 June–31 August, 2016–2018. The purpose of doing an "ensemble"

of three years is to reduce the dispersion among the individual years that may be related to boundary conditions. The multi-year strategy allows us to more effectively isolate the forcing related to the land surface characteristics amidst the complex internal model variability. Three years is not enough to isolate the internal forcing completely, but it is more robust than a single year.

Observational datasets are used to validate (but not calibrate) the model simulations at a basic level because the goal is to emphasize the potential implications of changing the soil characteristics on the land surface–atmosphere coupling without an attempt to rank the accuracy of the simulations. The approach used in this study does not constrain the simulations to observed variables, but rather allows the simulations to evolve free of constraint. This is a typical approach when the interest is to explore how free simulations divert depending on the changes to an internal factor (in this case, soil texture).

2.2.2 Soil texture

The FAO produced was the first global soil dataset, developed through both surveying and by combining coarse soil texture datasets into a single database with a scale of approximately 1:5 000 00 [FAO/UNSECO, 1971]. STATSGO, which is provided at 1-km resolution, evolved from FAO's soil map, by including datasets from multiple high-resolution sampling campaigns complemented with LANDSAT information over the conterminous US (CONUS), Alaska, Hawaii, and Puerto Rico. STATSGO has been defined over the CONUS and US territories; Outside CONUS

the source of data continues to be FAO.

Recently, other datasets have been developed which are comparable to STATSGO, including GSDE at about 1 km horizontal resolution. GSDE is also based on the FAO Soil Map of the World but uses advanced statistical methods and complex mapping techniques to harmonize multiple sources of soil information into a single high-resolution global dataset of soil type, organic matter, and nutrient contents [Shangguan et al., 2014]. GSDE and STATSGO each provide multiple vertical levels, but for uses in WRF they are processed into two levels each. During the pre-processing, the percentages of sand, silt, and clay are calculated by weighted averaging, with soil layer thickness used as the weight, and the soil is then classified into soil categories on the determined model grid in accordance with the USDA 16-class soil classification system. The soils data is fixed to two layers: a top (0–30cm depth) and bottom layer (30 cm–bottom of soil column), despite the differences in vertical resolution [Dy and Fung, 2016].

Figures 1a, b depict the top-layer soil texture classifications of WRF default STATSGO and GSDE soil datasets, respectively over the study domain. Note the differences in heterogeneity between the two, particularly throughout Mexico, the Central United States, and the Mississippi/Ohio River Basins. In the STATSGO soil dataset (Fig. 1a), loam (red) is dominant throughout Central Mexico and the mountain west, while silt loam (green) occupies much of the Midwest. In contrast, the GSDE dataset (Fig. 1b) exhibits a larger variety of soil types, with sandy loam (light green), sandy clay loam (light orange), and clay (brown) occupying much of Central Mexico. Likewise, over large portions of the U.S. Great Plains (hereafter,

GP) clay loam (light purple) and silty clay loam (orange) dominate in the GSDE dataset.

The specific differences are highlighted by category in Fig. 2. Figs 2a, b show the proportions of each category in two pie charts, and Fig. 2c shows the number of grid points associated with each category in both datasets. Categories along the y-axis of Fig. 2c are from the STATSGO dataset, and categories along the x-axis are from the GSDE dataset. The two largest differences between these two datasets are 3361 grid cells transitioning from STATSGO loam to GSDE clay loam, and 3309 grid cells transitioning from STATSGO loam to GSDE sandy loam. The former describes a decrease in average grain size (from loam to clay loam), while the latter is an increase in average grain size (from loam to sandy loam). The diagonal represents grid points that have the same soil category in the two datasets. If the two datasets are identical, there would be values only along the diagonal and zeros elsewhere. Zero values mean that there are no dataset transitions between the corresponding soil texture categories represented (e.g., no transitions from STATSGO sand to GSDE silt). The comparison of these two datasets for land-only points over this domain shows that only about 33% of the classification values are the same at 15 km modeled resolution, representing substantial uncertainty. Although some transitions may reflect only minor changes in the hydro-physical properties.

The dataset disagreements are not randomly distributed but tend to be spatially coherent and consistent, leaving a signal at regional scales. Figure 3 illustrates where the seven most common soil type differences occur. The STATSGO-to-GSDE

transitions representing increases in average grain size [loam-to-sandy loam (grey) and silt loam-to-loam (blue)], are primarily located in the western US, throughout Central Mexico, and in the Northeast. The remainder of the most common transitions characterize decreases in grain size and occurred throughout GP, Western US, the Mississippi and Ohio river Valleys, and the Atlantic Coast states.

2.2.3 Soil properties

Soil properties are the critical controllers of soil water infiltration, retention and availability to plants. In NWP, the use of soil parameter look-up tables is common practice. Select parameters from the WRF look-up table are presented in Table 1 and Fig. 4. In both Table 1 and Fig 4., the soil texture classes are organized by decreasing saturated hydraulic conductivity, which closely aligns with decreasing grain size. Saturated hydraulic conductivity is a measured quantity [Weil and Brady, 2017] that describes the efficiency at which a volume of saturated soil can transmit a volume of water (See values in Table 1, and Fig 4a).

In unsaturated soils, a primary restricting force for water movement is matric potential (hereafter, MP) [Weil and Brady, 2017], which describes the energy deficit that needs to be overcome before water can be removed from the soil system.Matric potential implicitly accounts for the effects of the pore size spectrum, the capillary action within the soil, and the adhesive properties of individual soil grains. Cosby et al. [1984] determined matric potential from 1448 soil samples by fitting a power-function, given by:

$$\Psi_m = \Psi_s \left(\frac{\theta}{\theta_s} \right)^{-b} \tag{2.1}$$

where Ψ_s is the matric potential at saturation, θ_s is volumetric soil moisture at saturation (or porosity), θ represents the actual volumetric soil moisture content, and b is an empirical parameter. The porosity describes the percentage volume of pore space in a volume of soil [Weil and Brady, 2017]. Physically, as the soil grain sizes decrease, the porosity decreases. The parameter, b, is highly variable, such that its value in some categories is smaller than the standard deviation of its value in other categories [Cosby et al., 1984].

As soil moisture decreases, the amount of energy needed to overcome the effects of matric potential increases (i.e., it requires more energy for roots to uptake soil moisture, and it requires more energy to evaporate moisture from the surface). Matric potential is shown here as a negative quantity, and when it exceeds (in magnitude) the wilting point, sometimes defined as matric potential $= -1500$ J kg^{-1}, it often reduces root consumption to zero and halts transpiration for most plant functional types [Stensrud, 2009].

Another important parameter is the field capacity (See values in Table 1 and Fig 4). The field capacity is the value of soil moisture remaining after free drainage occurs. The amount of water that can exist for a prolonged period in a soil profile is restricted to a finite range between the wilting point and the field capacity, called the extractable water. The extractable water is a useful metric in estimating the total soil water reservoir [Ritchie, 1981]. Figure 4 graphically displays the wilting

point, field capacity, saturated hydraulic conductivity, and matric potential as a function of soil texture. It can be seen that the wilting point and the field capacity both generally increase as grain size decreases, and so does the extractable water.

Figure 4b displays the matric potential at four soil moisture values, which are calculated as percentages of the extractable water range. For example, 25% of the extractable water range (EWR, below) is given by:

$$25\%\ EWR = \frac{0.25 \times \left(\theta_{fc} - \theta_{wp}\right) + \theta_{wp}}{\theta_s} \tag{2.2}$$

where, θ_{fc} is the field capacity, θ_{wp} is the wilting point, and θ_s is, again, volumetric soil moisture at saturation. Note that for larger grain soils, the matric potential is near zero (i.e., little energy is required before evaporation can occur), but for smaller grain soils like clay, the matric potential gets strongly negative (i.e., significant energy is required before evaporation can occur). Fig. 4b shows that two categories (i.e, clay and silty clay) have started to experience the exponential decrease of matric potential at 25% saturation (dotted line), such that plants could likely no longer extract water from a clay profile at this saturation. As the saturation percentage increases, all categories approach 0 J kg^{-1}, which permits evaporation to occur with only little activation energy required.

2.2.4 Soil texture and hydroclimate uncertainty

The impact of the soil properties on ET is susceptible to shifts in hydroclimate. At low moisture content ($< 20\%$ saturation, likely the case in "dry regimes"), matric

potential decreases for all categories, and the uncertainties in soil hydro-physical properties will have little consequence to WRF simulations. Similarly, at higher soil moisture contents ($> 60\%$, likely the case in "wet regimes"), matric potential approaches 0 J kg^{-1} in all soil texture categories (Fig. 4). It is at moderate values of soil water content that uncertainties in soil hydro-physical properties can play a pivotal role in determining the accuracy of surface water and energy fluxes.

At mid-range soil moisture values in smaller-grained soil, instead of LHF occurring, the available incoming energy would be partitioned into sensible heat flux (SHF). Enhanced SHF would lead to increased temperatures above the surface. Furthermore, increasing the temperature at and above the surface would decrease the relative humidity, increase the localized buoyancy, enlarge the turbulent convective eddies mixing the boundary layer, and increase the planetary boundary layer height (PBLH). This series of processes can be linked to the land and further linked in part to soil texture. The connection of physical properties described here follows the local "process chain" in land–atmosphere (L–A) interactions [e.g., Santanello et al., 2011]—a way to systematically view the linkages between the land and the atmosphere from a physical perspective.

2.3 Results

2.3.1 WRF verification

The WRF simulations are assessed by comparing the 2016–2018 JJA seasonal mean 2-m air temperature with gridded surface observations from the 2016–2018 monthly

mean Global Historical Climatology Network version 2 and Climate Anomaly Monitoring System [GHCN-CAMS; Fan and van den Dool, 2008]. The GHCN-CAMS data is bi-linearly interpolated from its native 0.5° resolution to the model grid, and displayed in Fig. 5a. The observations show the warmest temperatures along the Gulf Coast of the US and Mexico, in the desert southwest, and along the Gulf of California in Mexico. Temperatures in the central-western United States and throughout Central Mexico are cooler as a result of the significant terrain features, notably the Rocky Mountains, and the Sierra Madre Mountains, respectively. Finer-scale features, such as the depression in values along the Appalachian Mountains and enhancement of temperature along the interior of California, lend credence to the quality of the dataset.

For comparison, Figs. 5b and c show the average 2-m temperature for the STATSGO and GSDE simulations, respectively, for the three year JJA period. The differences between the model simulations and the observations are calculated for WRF-STATSGO and WRF-GSDE in Figs. 5d and 5e, respectively. The large scale-patterns of 2-m temperature suggest that in both cases the model does a reasonable job in reproducing many features of the observed pattern. Overall, the simulated features correspond well to the observed features. Both models show a moderate warm bias (+2 K) throughout the GP, the Gulf Coast states and east of the Appalachian Mountains, with the STATSGO simulation (Fig. 5d) performing slightly better in those regions. A cool bias of ~ 1.5 K is found in the high deserts of Nevada, east of the Sierra Nevada Mountains.

Given the role of the diurnal radiative cycle on land–atmosphere (L–A) in-

teractions, it is important to evaluate the modeled diurnal cycle of near-surface atmospheric variables. Observations for JJA 2016–2018 are collected from about 220 stations from the Integrated Surface Database [Smith et al., 2011] throughout the GP region (approx. latitude: 32–41° N, longitude: 91–102° E). The timing of the maximum and minimum temperature are consistent with observations of diurnal cycle of 2-m temperature (Fig. 6a). The model simulations exhibit a +3 K warm bias throughout this region (slightly larger during daytime, smaller at night). The magnitude of the bias agrees with the mean fields shown in Fig 5. The difference between the model simulations at this time-averaged scale is minor in Fig. 6. Nevertheless, understanding the impact of soil texture should lead to a better understanding of the physical processes involved in the land surface–atmosphere coupling. Fig. 6b shows similar patterns in the 2-m dew point temperature—consistent timing in the occurrence of the maximum and minimum values, but exhibiting a larger persistent negative bias of approximately 4 K. Both model environments are warmer and drier than observations by similar margins.

The diurnal onset of observed 10-m wind speeds (Fig. 6c) is, again consistent between the model simulations and the station observations. The magnitude of the peak diurnal winds is greater than the observed values in both simulations by about 2 m s^{-1}, while the minimum values are closer to the station observations. Again, both simulations exhibit minor differences from observations, but have similar performances to each other.

In an effort to validate the WRF/CLM simulations against satellite-based hydrological variables, we compared the model simulations to GLEAM (version 3)

ET [Martens et al., 2017; Miralles et al., 2011]. Both WRF/CLM simulations exceed GLEAM ET [Martens et al., 2017; Miralles et al., 2011] estimates by about 1.5 mm day^{-1} (not shown). Further, the overestimation of total ET in CLM relative to other LSMs has been noted in a global intercomparison of LSM performance [i.e., Ferguson et al., 2012].

GLEAM includes the partitioning of ET into components: bare soil evaporation, transpiration, and evaporation from canopy interception. The ratio of canopy-intercepted evaporation to total evaporation is small and similar in both GLEAM and WRF/CLM. The WRF/CLM bare soil evaporation accounts for about 40–45% of the total ET, and transpiration accounts for about 30-35%. GLEAM, on the other hand, assigns about 90% of ET to transpiration. Either the WRF/CLM simulations place too much emphasis on bare soil evaporation [i.e., Lawrence et al., 2007], or GLEAM puts too much weight on transpiration [Or and Lehmann, 2019, Appendix C]. The correct quantity may lie somewhere in the middle of the two. These differences in partitioning seem large, but they are a significant improvement on the CLM3 formulation and are reasonable values compared to previous studies [e.g., Lawrence et al., 2007]. The differences between the two WRF/CLM simulations are smaller than the differences between either simulation and the GLEAM product. When the specific parameters, differing equations and model structures are considered, this is perhaps unsurprising. Additional analysis comparing these WRF/CLM simulations to a calibrated hydrological dataset suggests that total ET compares quite well to an LSM-produced ET climatology, but SM tends to be more model specific. This analysis is presented in Appendix B.

2.3.2 Modeled sensitivity to soil texture classification

2.3.2.1 Generalized domain differences

We will examine next the changes in the soil-water system that result from changing the input soil classification dataset (GSDE vs STATSGO). Fig. 7a shows the differences (WRF-GSDE minus WRF-STATSGO) in JJA 2016–2018 averaged top 30-cm volumetric soil moisture, and Fig. 7b–d show the corresponding differences in porosity, field capacity and wilting point, respectively. The differences in soil moisture are wide-spread throughout the model domain, but with prominent positive values along the southern Atlantic coast, and prominent negative differences on the south-facing coast of southern Mexico. Field capacity, and wilting point increase with decreasing soil grain size (though, at differing rates), meaning positive differences indicate a reduction in grain size from STATSGO to GSDE within that grid space. Note the majority of positive values throughout the Midwest and the dominant (though, minor) negative differences in Central Mexico, consistent with Fig. 3. The differences in soil moisture (Fig. 7a) are highly correlated to the differences in both wilting point and field capacity. Calculating the Spearman Rank Corrleation Coefficient between the fields in Fig. 7a and Fig. 7d yields $\rho = 0.927$, suggesting that the mean soil moisture is highly related to the assigned parameters.

Porosity is not so straightforward, showing negative differences throughout the Midwest. This is because the range of porosity values (with the exception of sand) is small (See Table 1), and therefore, the values in the Midwest, though negative, are

very minor. Differences in the long-term average of soil moisture are most similar to the differences in the assigned wilting point. Between rainfall events, as the soil dries, the soil moisture has a propensity to return to the wilting point and rarely goes below it. This behavior explains why the differences in soil moisture mirror the differences in assigned wilting point, and it emphasizes the importance of assigning hydro-physical properties via the placement of soil texture.

Figure 8 presents JJA-averaged differences (WRF-GSDE minus WRF-STATSGO) in relevant surface fluxes and variables. The corresponding differences can be predominantly attributed to changes in the soil physical properties. Wherever GSDE has finer grains than STATSGO, e.g. over the Midwest, the soil moisture will be nearer to the wilting point at a higher value leading to slightly positive or neutral differences in SM (Fig. 7a) but mostly negative differences in LHF (Fig. 8a). Larger negative values in LHF are collocated with larger positive SHF values (Fig. 8b). On the contrary, areas of coarser grains in GSDE, e.g., over central Mexico, exhibit an increase in LHF (positive values in Fig. 8a) and a corresponding decrease in SHF (Fig. 8b).

Surface fluxes directly impact conditions within the PBL. Over the Midwest, where WRF-GSDE has smaller surface LHF, the 2-m moisture also has smaller values (Fig. 8c). Over central Mexico and western US, the opposite is true: The coarser grain sizes/smaller matric potential (in magnitude) lead to an increase in LHF and a corresponding increase the 2-m moisture content. A similar analysis of the SHF and 2-m temperature is possible. Incoming energy that could not remove moisture from the surface due to the matric potential constraints is instead parti-

tioned into SHF. Therefore, Figure 8b,d shows an increase in SHF in the Midwest and a corresponding near surface warming. The opposite is true in Central Mexico, where the decrease of SHF yields reduced temperatures at 2 m. Note that the patterns of differences in 2-m temperature and 2-m mixing ratio do not correspond exactly to those of the fluxes. The net radiation (R_{net}) and ground heat flux (G) were investigated as a potential cause of these discrepancies, but the diurnal cycle of R_{net}, G, and the component terms of the radiation budget did not show any substantial differences (not shown). The differences in the spatial distribution of 2-m temperature and 2-m moisture are likely related to the dynamic effects of advection that are implicitly included above the surface (not discussed here).

Changes in the SHF induce changes in the turbulent eddy growth and thus affect the PBL height (PBLH). Because soil texture modulates the placement and intensity of SHF, this sequence of processes corroborates the idea that the PBLH is sensitive to changes in the soil texture. As a result, Figure 8f shows that PBLH increases over the Midwest and decreases over central Mexico—a pattern consistent with that of SHF (Fig. 8b) responding to changes in soil grain sizes (Fig. 3).

Precipitation in models is an inherently integrative process involving appropriate thermodynamic conditioning, dynamic lifting, as well as a triggering mechanism. The reference profiles for the BMJ convective scheme are calculated by lifting parcels from the boundary layer, and their time dependence responds directly to the land surface forcing. Patterns of precipitation in Fig. 8e do exhibit an impact from changes in the soil properties. Although these results do not necessarily imply a cause-effect behavior, differences in precipitation are likely due to the ET compo-

nent of land–atmosphere (L–A) interactions.

2.3.2.2 Great Plains regional differences

WRF-GSDE minus WRF-STATSGO soil texture differences over the GP show the prevalence of three major category changes that represent a decrease in grain size. The region delimited by 91–102° W, 32–41° N (see Fig. 9a) has 468 grid spaces that shift from silt loam to silty clay loam, 338 from loam to clay loam, and 247 from silt loam to clay loam. Together, they account for about 25% of the total grid cells in this region. The locations of these differences are shown in Fig. 8a (along with some additional less frequent category changes). The changes in grain size from one category to another are not uniform. For example, the difference in grain size between silt loam and clay loam is much smaller than the difference in grain size between sandy loam and clay loam. Consequently, differences in the corresponding hydro-physical parameters over the region will also be non-uniform.

Decreasing the soil grain size reduces soil water availability to ET due to changes in matric potential (Fig. 9b; See Eq. 1). The fine-grained soils retain soil moisture more vigorously than coarse grain soils and thus more energy will be required to extract this moisture. Fig. 9b shows averaged differences in matric potential for each of the soil texture transitions in Fig. 9a calculated using the seasonally-averaged volumetric soil moisture. Changes in matric potential suggest that in one soil category ET could be occurring while in the other category it is likely that ET would not be occurring. For example, in the case of silt loam to

silty clay loam (dark green), if the simulation with silt loam (WRF-STATSGO) had matric potential values conducive to ET, and the simulation with silty clay loam (WRF-GSDE) in those same grid spaces had matric potential values not conducive to ET, then $\Delta\Psi$ would be greater than zero. The $\Delta\Psi_m$ was positive in each of the 468 grid spaces that underwent this transition.

According to Fig. 9c, the differences in wilting point are positive for coarse-to-fine transitions, and negative for fine-to-coarse transitions. The same is true for differences in field capacity (Fig. 9d), which follow a similar pattern as the wilting point. It is apparent that the differences in wilting point and field capacity will change depending on which categories are compared. Certain transitions [i.e., sandy loam to loam, (red)] denote a minor shift in grain size with relatively small differences in the parameters' values. Other shifts in categories (i.e., sandy loam to clay loam) represent a considerable shift in grain size, resulting in large differences in the parameters. These differences are further noted in the b-parameter (Fig. 9e), the exponential term in Eq. 1. The differences in b between certain categories, such as between sandy loam and loam are very small, while between other categories (e.g., sandy loam-to-clay loam) the differences are substantial. In areas where the soil grain size decreases, it is expected that the average value of the LHF (Fig. 9g) in that area will also decrease. The decreases in LHF are compensated by increases in SHF (Fig. 9h), which is apparent in the category-averaged differences. As a result of the partition between the two heat fluxes, Figs 9g and 9h are similar but of opposite sign.

Not all reductions in soil grain size are as intuitive, however. The differences in

parameter values (Figs. 9c–e) are much larger for the transition from sandy loam to clay loam than they are for the other most common transitions, yet, the differences in the matric potential for sandy loam to clay loam are only moderate (Fig. 9b) compared to the other categories. This alludes to the definition of matric potential (Eq. 1), which considers both the hydro-physical parameters and the value of soil moisture (Fig. 9f). In the case of the sandy loam to clay loam transition, the large differences in parameter values and the large differences in soil moisture (Fig. 9f) result in a competing effect that reduces the differences in matric potential rather than enhancing it. Further, the moderate differences in matric potential yield only moderate differences in the LHF (Fig. 9g), and, likewise, only moderate differences in SHF (Fig. 9h). One would expect large differences in LHF corresponding to large differences in soil moisture. However, the sandy loam to clay loam transition supports the assertion that neither soil moisture, nor soil properties solely control surface fluxes, but rather it is the combination of the two that dictate the surface fluxes. For that matter, it is not only the soil characteristics but a combination of all surface hydro-physical characteristics (including the effects of vegetation) and soil moisture that determine the nature of the L–A coupling. Furthermore, changes in the PBL characteristics and stability may affect precipitation processes.

The effect of grain sizes on the surface variables is further analyzed by examining the diurnal cycle in the two WRF simulations (Fig. 10). The solid lines are area-averages over the GP region, while dashed lines correspond to averages in grid spaces that underwent a certain transition: silt loam (WRF-STATSGO) to silty clay loam (WRF-GSDE). The evolution of the variables throughout the day

has the same shape, but with important differences in magnitude. Nighttime values of LHF and SHF are close to zero. LHF rises up to a maximum at noon of about 150-200 W m^{-2}, while noontime SHF is about 250-300 W m^{-2}. These values are of the same order of magnitude as those reported in the literature from observations in Oklahoma [e.g., Marshall et al., 2003]. According to Fig. 10a, LHF (dashed, blue) achieves the largest values for the WRF-STATSGO simulation where silt loam (the coarser grains) dominates. LHF is reduced when STATSGO silt loam classification is replaced with GSDE silty clay loam classification. The smaller soil grains in the WRF-GSDE simulation lead to a higher energy requirement to extract water from the soil system, and thus the reduction in LHF. Differences between the two specific soil types are as large as 50 W m^{-2} at 1300 LT, which is about 10–20% of the daily peak, while the effect of the changed soil classification over the entire GP is only about 10 W m^{-2} at 1300 LT (Fig. 10). Regardless of the magnitudes, uncertainties in estimating LHF and SHF exist and can be related to soil hydro-physical properties.

Changes in the diurnal cycle of SHF (Fig. 10b) are consistent with the changes in LHF Fig. 10a. The WRF-GSDE simulation with its finer grain sizes (silty clay loam) displays increased values of SHF over the WRF-STATSGO simulation with its coarser silt loam. Again, this is noticed both in the area averages over the specific categories (dashed lines) as well as over the whole GP (solid lines). The diurnal cycle of 2-m temperature (Fig. 10c) follows similar patterns to SHF: greater values over finer soils, and largest differences in the afternoon, though now the separation between soil texture classes and the regional averages is not as great

because the dynamic effects of advection are implicitly incorporated. Lastly, during daytime, with well-mixed conditions, differences between the PBLH over silty loam (STATSGO) and silty clay loam (GSDE) average 75 m (Fig. 10d), indicating that even PBLH can be partially related to the soil hydro-physical properties.

2.3.2.3 Central Mexico regional differences

Contrary to the changes in the GP, in Central Mexico the change from STATSGO to GSDE implies the largest coherent increase in average grain size in the full model domain (See Fig. 3). While this region represents a convenient contrast in grain size, it also contains significant terrain features such as the Sierra Madre Occidental, the Sierra Madre Oriental, and the high plateaus of central Mexico that are more complex than the relatively flat terrain that is present in the GP. Also, there are precipitation differences present in Central Mexico in the full simulation mean, as well as in the individual years (not shown). Due to its location, this region is susceptible to influence from the North American Monsoon and the ITCZ, which influence precipitation and add additional complexity to the environment.

Figure 11a depicts the distribution of soil texture differences (GSDE to STATSGO) in the central Mexico sub-domain, showing that the most common shift is from loam to sandy loam, an increase in grain size representing a small change in the soil hydro-physical properties (Fig 11c–e). Particularly, the differences in matric potential between loam and sandy loam are about 100–200 J kg $^{-1}$—large enough to modulate LHF values, but not exceedingly large. These differences in matric

potential contribute to the differences in LHF (Fig. 11g), which are positive in that category consistent with the increase in soil grain size. Correspondingly, the averaged differences in SHF are negative (Fig. 11h).

Another noteworthy aspect of this analysis is that despite the categories undergoing reductions in grain size having increased average soil moisture (Figs. 9f and 11f), those categories experience reductions in LHF (Fig. 9g and 11g). This phenomena can be related to the assigned wilting point in each category. During dry down, finer grain soils have higher wilting points meaning they have an increased minimum value for soil moisture (excluding extreme circumstances). Therefore, despite consistently elevated soil moisture, these grid spaces will also experience reduced LHF because the soil moisture will achieve its minimum value during dry down at a greater soil moisture value.

Contrary to the GP, where the three most common transitions were of the same sign (i.e., decreases in grain size), in Central Mexico, the second most common shift, from loam to clay, represents a reduction in grain size instead of an increase. Therefore, in principle, the competing effect of both increasing and decreasing the soil grain size within the region should mitigate the regionally-averaged differences in the surface fluxes between the simulations. The loam-to-clay transition towards the south of the region (dark green, Fig 11a) exhibits considerable differences in the hydro-physical properties (θ_{wp}, θ_{fc} and b; Fig 11c, d, and e, respectively). The corresponding differences in soil moisture (Fig. 11f) are also large. Despite the significant differences in hydro-physical parameters and the relatively large differences in soil moisture (Fig. 11f) and matric potential (Fig. 11b), this transition results

in only modest differences in the surface fluxes. While the differences in surface fluxes are consistent in sign with the differences in hydro-physical properties and in soil moisture, the magnitude of the surface flux differences (Fig. 11g and 11h) is smaller than expected, considering the differences in hydro-physical properties. Again, while soil hydro-physical properties are important in determining surface fluxes, so are other surface hydro-physical characteristics, such as those associated with vegetation, topography, and land cover type.

2.4 Summary and Conclusions

The effects of soil moisture on weather and climate have been widely discussed in recent decades, though the underlying role of soil texture and corresponding properties in that relationship has only recently started to be considered. The capacity of soil to retain moisture depends on its hydro-physical properties, which are dictated in part by the size of the soil grains. This article discusses the implications of soil properties, via the assignment of soil texture, for the computation of surface variables relevant to the PBL structure. Two widely used soil texture datasets were compared (the STATSGO dataset from the United States Department of Agriculture, and the GSDE dataset from Beijing Normal University). In comparison to the STATSGO dataset, the GSDE dataset exhibits a spatially coherent decrease in soil grain size over the Midwest, while over Central Mexico it has a spatially coherent increase in soil grain size. This study contrasts WRF 2016–2018 JJA simulations employing the STATSGO soil texture dataset against similar simulations using the

GSDE soil texture dataset. This study does not intend to evaluate the accuracy of either dataset. Rather, it seeks to understand how modeled surface and near-surface variables are affected by the use of one dataset versus the other.

It has been shown that the changes in soil texture and corresponding properties affect the soil moisture content, since it is highly correlated to the wilting point. In the Midwest, the GSDE simulation with its finer grains results in a reduction in LHF, and an increase in SHF. The change in surface fluxes leads to enhanced warm and dry conditions in the multi-year average. Consistent with the impacts of soil grain size, the opposite is true over Central Mexico. There, GSDE identifies larger size grains than STATSGO, resulting in an increase in LHF with a corresponding decrease in SHF.

The changes in surface fluxes due to soil hydro-physical properties lead to differences in the thermodynamic structure of the PBL. The decrease of LHF over fine soils is consistent with the decrease in low-level humidity, while the increase in SHF corresponds to an increase in low-level atmospheric temperature. Furthermore, the PBL height is a function of turbulent eddy growth, which can be closely related to SHF. In the Midwest, the increase in SHF over the smaller-grain soils of the GSDE experiment lead to a deeper PBL. The opposite is true for Central Mexico, where the PBL becomes shallower. Notably, the use of finer grains over the Midwest results in a reduction of the mean precipitation while the use of larger grains over Central Mexico tends to increase it. The mechanisms by which these changes occur are the subject of a follow-up article.

The surface fluxes are a crucial element of land-atmosphere feedbacks acting

through different mechanisms. The most common discussed in the literature involves vegetation properties, which are not discussed here. This paper highlights the role of soil hydro-physical properties in those exchanges. At present most models do not represent processes that link vegetation with soil properties. The combined effects of soil and vegetation on surface fluxes warrant further investigation.

The analysis of the individual contributions of each soil type reveals that the soil properties themselves do not alone dictate the surface fluxes, but rather, it is a combination of soil properties and soil moisture that do it. The choice of soil texture database, as well as the soil parameter values in the look-up table should be made with care, as they can have considerable consequences on simulated regional climate.

2.5 Final Summary of Physical Relationships

This chapter has focused on the physical relationships that connect the land surface to the atmosphere through the lens of soil texture representation in LSMs, and differences in the associated soil hydro-physical properties. When parameterizations are called within a land surface model grid space, soil parameters are extracted from the look-up table and input into the model equations based on the soil texture category in that grid space. It has been shown that the location of these soil texture categories in reality is very uncertain, and between two premier datasets only few grid spaces are assigned the same soil texture categories. Therefore, the land surface model equations receive different soil hydro-physical parameters depending on the

assigned soil texture categories, which leads to differences in the results of those equations.

Figure 2.12 is a schematic depicting these relationships with coarse soil grains on the left (a) and fine soil grains on the right (b). Differences in soil hydro-physical parameters, such as wilting point and field capacity, dictate different behaviors of soil layers in the land surface model. Both WP and FC are based on a term called matric potential (Eq. 2.1). Inverting Eq. 2.1 to solve for θ allows calculation of both WP and FC,

$$\theta_{wp,fc} = \theta_s \left(\frac{\Psi_m}{\Psi_s} \right)^{\frac{-1}{b}} \tag{2.3}$$

with FC occurring at Ψ_m = -33 J kg^{-1}, and WP occurring at Ψ_m = -1500 J kg^{-1}. Matric potential describes an energy barrier that needs to be overcome before moisture is removed from a volume of soil. It is due to the adsorptive properties and capillary forces between individual soil grains. The movement of moisture within the surface is based on the vertical gradient of matric potential as represented in Richards equation. Water travels towards layers with strongly negative matric potential. Therefore, it is much easier to remove water upwards through evaporation and transpiration, and downwards through gravitational drainage in coarse-grained soils like sand, which usually have matric potential values close to zero. On the other hand, fine grained soils like clay, which can have matric potential values $< -10^4$, retain moisture, and restrict moisture movement within the soil column.

This difference in behavior based on soil grain size has implications for the coupled land-atmosphere system. In areas denoted by a reduction of soil grain

size from STATSGO to GSDE, there was a reduction in associated latent heat flux in the ensemble mean differences. This reduction in latent heat flux is due to stronger (more negative) matric potential in finer soil grains which restricts both the evaporation of water from bare soils, and the uptake of water by root systems leading to a reduction in transpiration. Because latent heat flux is reduced due to soil behavior, the energy that could not remove moisture form the soil was partitioned into sensible heat flux instead. A schematic comparison between idealized grid spaces with the same value of soil moisture is available in Fig. 2.12. Grid spaces with coarse grains experience elevated latent heat flux and reduced sensible heat flux, while grid spaces with fine soil grains experience the opposite behavior.

The responses of the surface latent and sensible heat fluxes then affect low-level thermodynamic variables (i.e., T2m, and q2m). In areas of reduced latent heat flux, there is an associated reduction in low-level moisture (i.e., q2m). In those same areas, because the latent heat flux is reduced and the sensible heat flux increased to compensate, there was an increase in 2-m temperature (i.e., T2m). This leads to warm and dry biases above the surface in areas with finer soil grain sizes. Also, in areas of increased sensible heat flux there was an associated increase in the height of the PBL (i.e., PBLH). The response of PBLH is expected due to the close relationship between sensible heat flux, turbulent kinetic energy, and the growth and decay of the PBL.

Therefore, it has been shown through these physical mechanisms that differences in soil grain size and the related differences in soil hydro-physical properties can affect the connection between the land surface in the atmosphere. The soil's

effect on the land-atmosphere connection is manifested in the effects of soil hydrophysical properties on the movement of moisture within the soil column and the movement of moisture between the land surface and the atmosphere by way of latent heat flux. The main takeaway is that at a given value of soil moisture, fine soil grains retain moisture more strongly, than coarse soil grains do. This can lead to differences in latent heat flux, and therefore, differences in the surface energy balance and land-atmosphere coupling.

soil texture category	K_s $(\times 10^4)$	Ψ_s	θ_s	b	θ_{wp}	θ_{fc}
sand	0.466	0.069	0.339	2.79	0.010	0.192
loamy sand	0.141	0.036	0.421	4.26	0.028	0.283
sandy clay	0.0722	0.098	0.406	10.73	0.100	0.338
sandy loam	0.0523	0.141	0.434	4.74	0.047	0.312
sandy clay loam	0.0445	0.135	0.404	6.77	0.069	0.315
loam	0.0338	0.355	0.439	5.25	0.066	0.329
silt loam	0.0281	0.759	0.476	5.33	0.084	0.36
clay loam	0.0245	0.263	0.465	8.17	0.103	0.382
silt	0.0218	0.955	0.484	3.86	0.061	0.347
silty clay loam	0.0203	0.617	0.464	8.72	0.120	0.387
silty clay	0.0134	0.324	0.468	10.39	0.126	0.404
clay	0.00974	0.468	0.468	11.55	0.138	0.412

Table 2.1: Select soil hydro-physical parameter values extracted from the WRF model look-up table, SOILPARM.TBL. Saturated hydraulic conductivity (K_s), matric potential at saturation (Ψ_s), porosity (θ_s), the b-parameter, wilting point (θ_{wp}), and field capacity (θ_{fc}) are shown. See text for details.

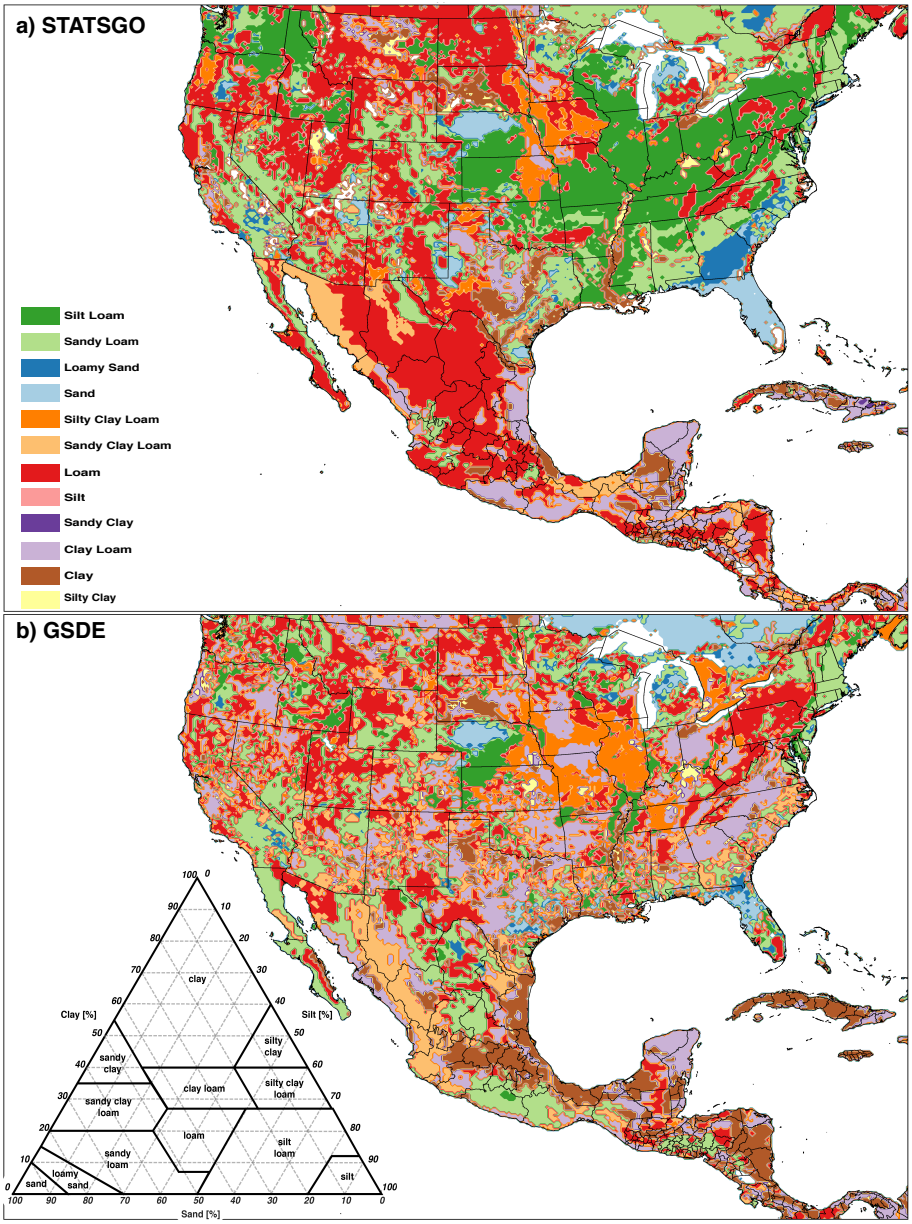

Figure 2.1: Dominant top-layer soil texture classification in this study's model domain at 15-km horizontal resolution according to (a) the STATSGO soil texture database (default in WRF) and (b) the GSDE soil texture database. The categories in both maps follow the key in (a). The categorical soil texture triangle has been provided (lower left corner of b).

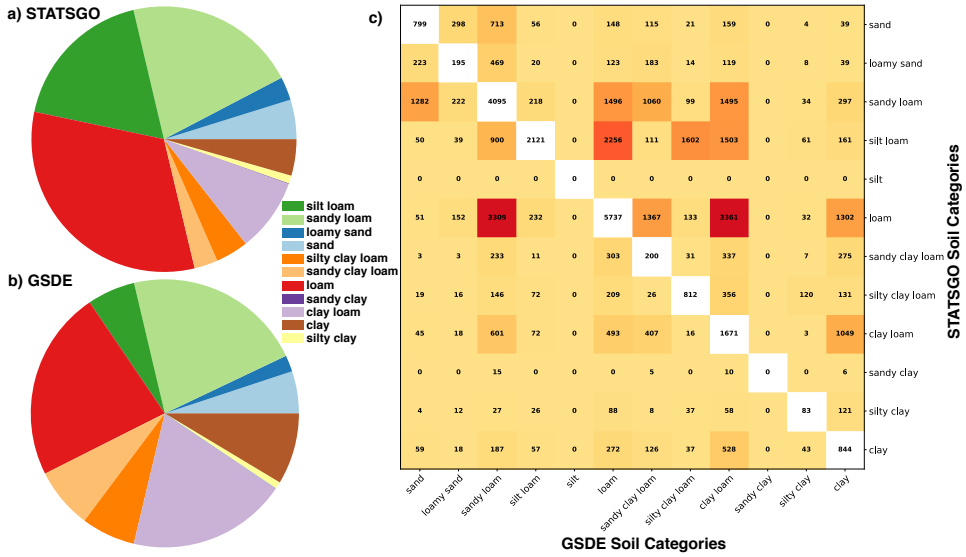

Figure 2.2: Pie charts depicting the proportion of each soil category for each (a) STATSGO, and (b) GSDE, and (c) count of grid spaces at 15-km resolution with given soil texture transitions from the STATSGO category (vertical axis) to the GSDE category (horizontal axis) (e.g., 3361 loam grid spaces in STATGSO transitioned to clay in GSDE). In addition to the digits, white boxes denote classification consensus between the two datasets; the higher number of transitions the greater the color intensity (i.e., darker hues show more common occurrences).

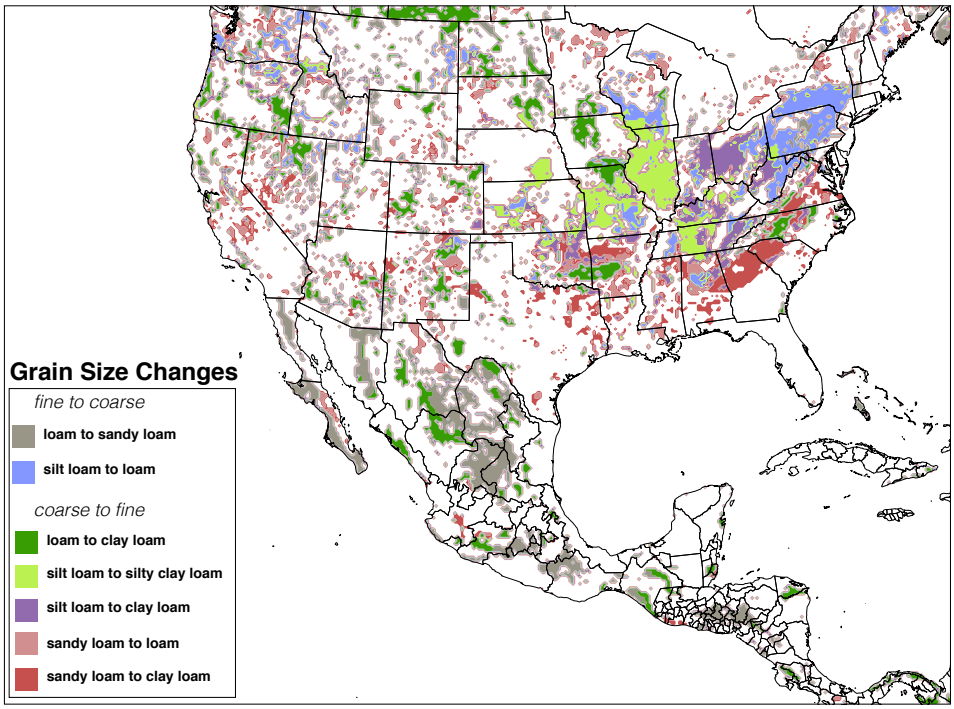

Figure 2.3: Locations of the seven most common soil texture category transitions from STATSGO to GSDE for the model domain. Loam to sandy loam (gray), and silt loam to loam (blue) represent increases in grain size. Loam to clay loam (dark green), silt loam to silty clay loam (light green), silt loam to clay loam (purple), sandy loam to loam (pink), and sandy loam to clay loam (red) represent decreases in average grain size.

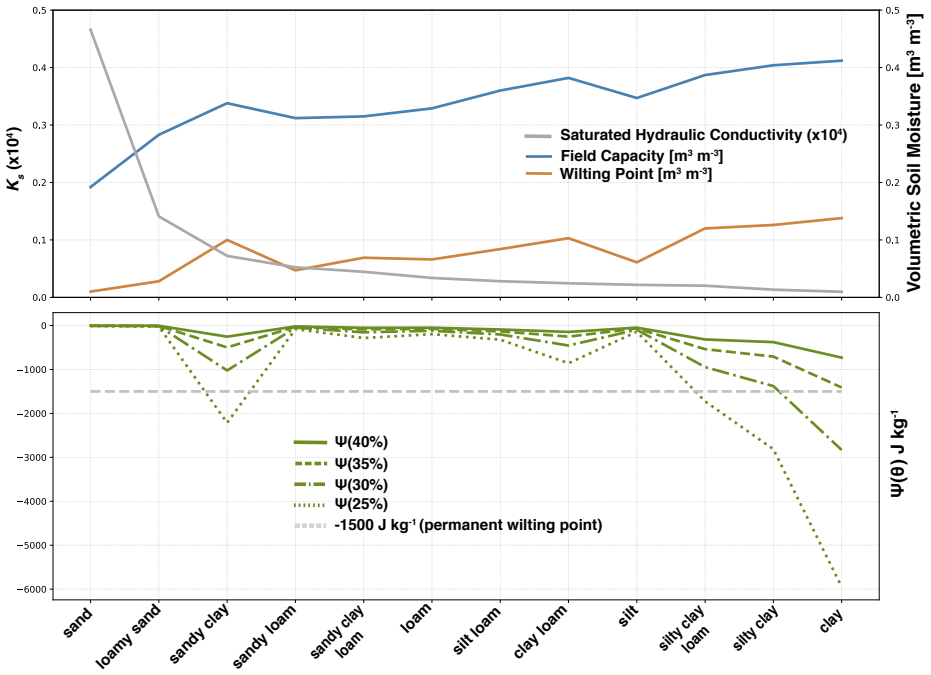

Figure 2.4: Prescribed parameter values for each soil texture category from the default look-up table in the WRF model. Top panel: Field capacity (blue) and wilting point (orange) have units of volumetric soil moisture [m^3 m^{-3}; top right axis]. Saturated hydraulic conductivity (gray) is a unitless quantity [shown x10^4; top left axis]. Bottom panel: matric potential (units: J kg^{-1}) calculated according to a percentage of the extractable water range as given by Eq. 2: 40% (solid green), 35% (dashed green), 30% (dashed-dotted green), and 25% (dotted green).

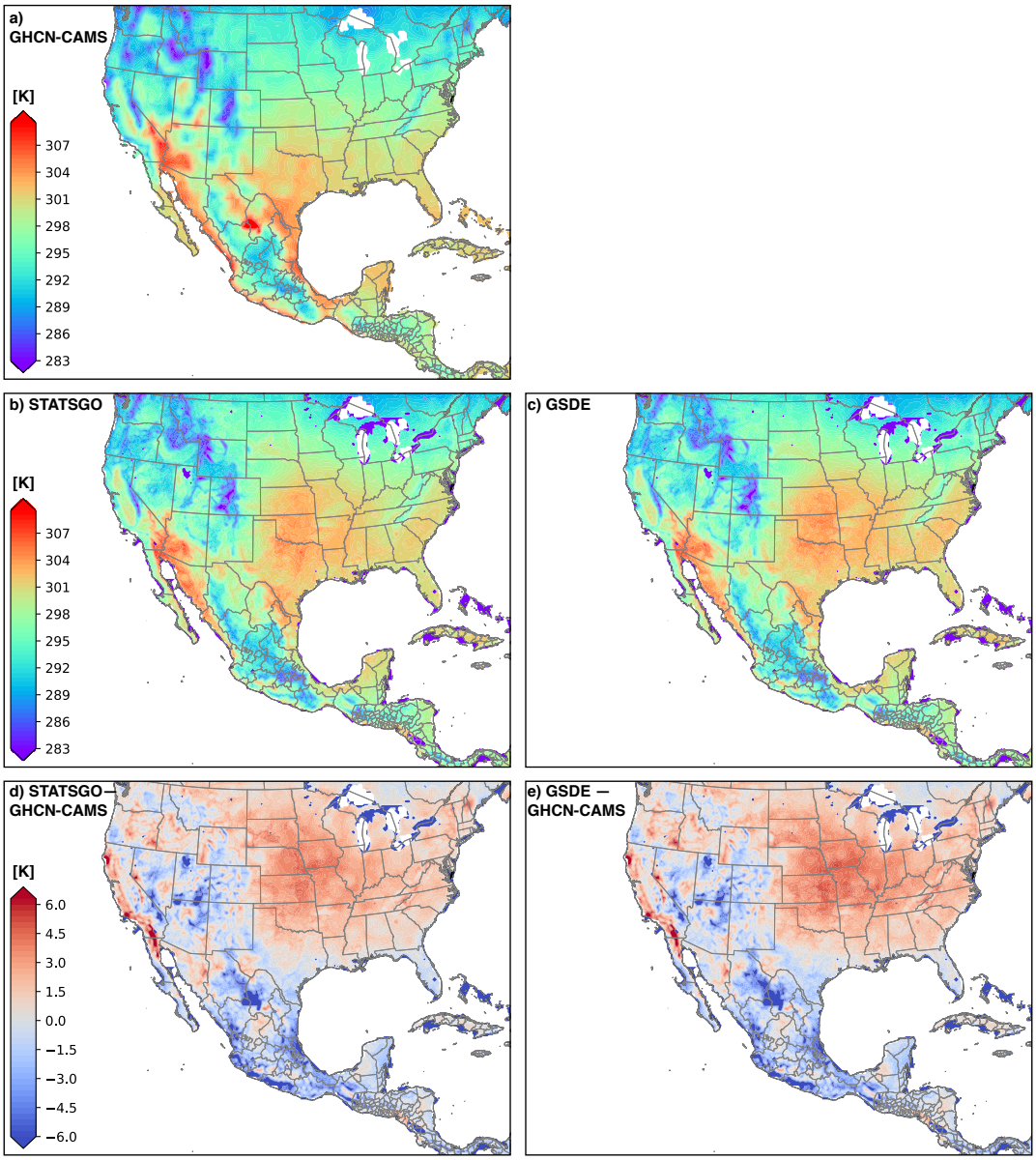

Figure 2.5: Two-meter air temperature (T2m) and model-minus-observational differences averaged over the period JJA 2016–2018. (a) GHCN-CAMS gridded T2m, (b) the WRF-STATSGO T2m, (c) the WRF-GSDE T2m, (d) differences between the WRF-STATSGO and GHCN-CAMS T2m, and (e) differences between the WRF-GSDE and GHCN-CAMS T2m.

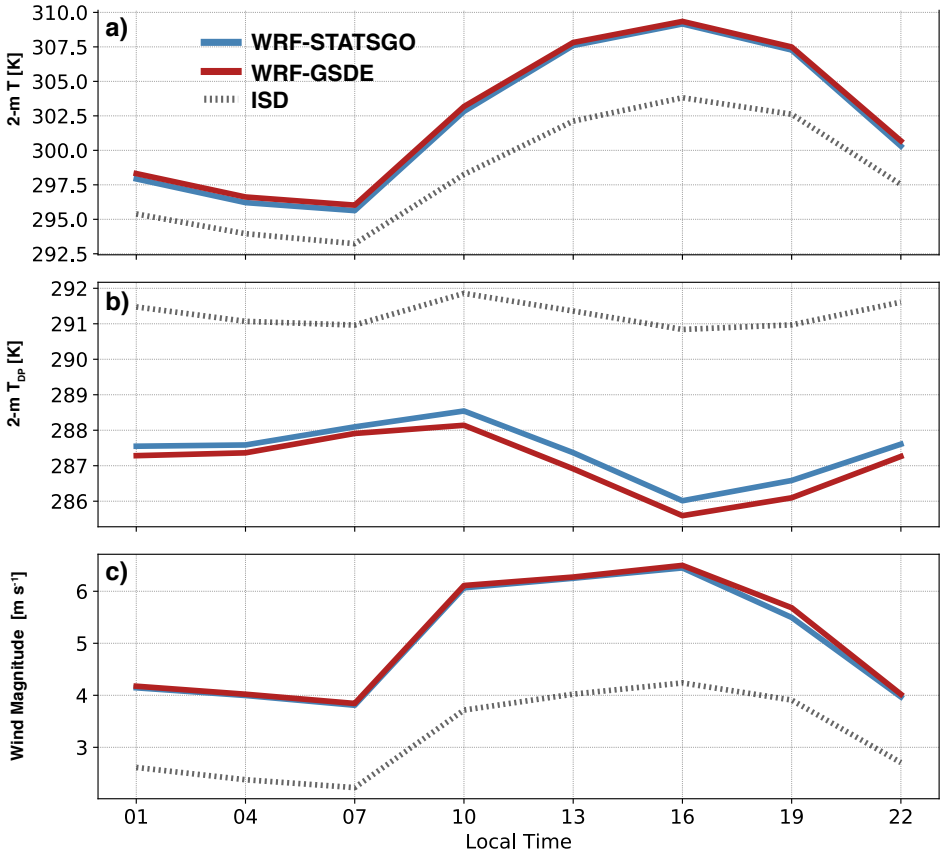

Figure 2.6: Mean (JJA 2016–2018) diurnal cycles from model grid spaces collocated with 220 NOAA Integrated Surface Database (ISD) stations in the GP region (approx. latitude: 33–42° N, longitude: 92.5–102.5° W) of (a) 2-m temperature [K], (b) 2-m dew point temperature [K], and (c) 10-m wind speed magnitude. The WRF-STATSGO simulation is in blue, the WRF-GSDE simulation is in red, and ISD sites are black dotted. The region is shown in Fig. 9a.

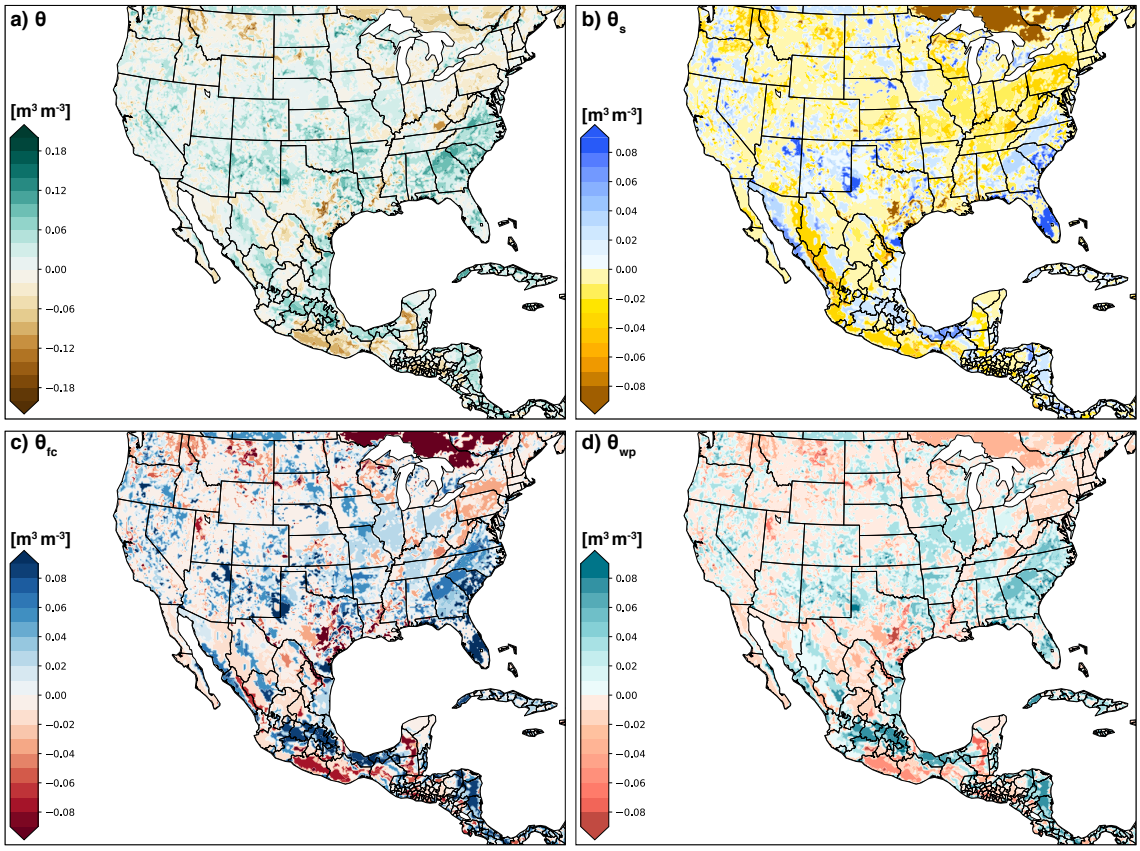

Figure 2.7: Differences (WRF-GSDE minus WRF-STATSGO) in (a) top 30-cm JJA 2016–2018 averaged volumetric soil moisture, and the assigned values of (b) θ_s, (c) field capacity, and (d) wilting point.

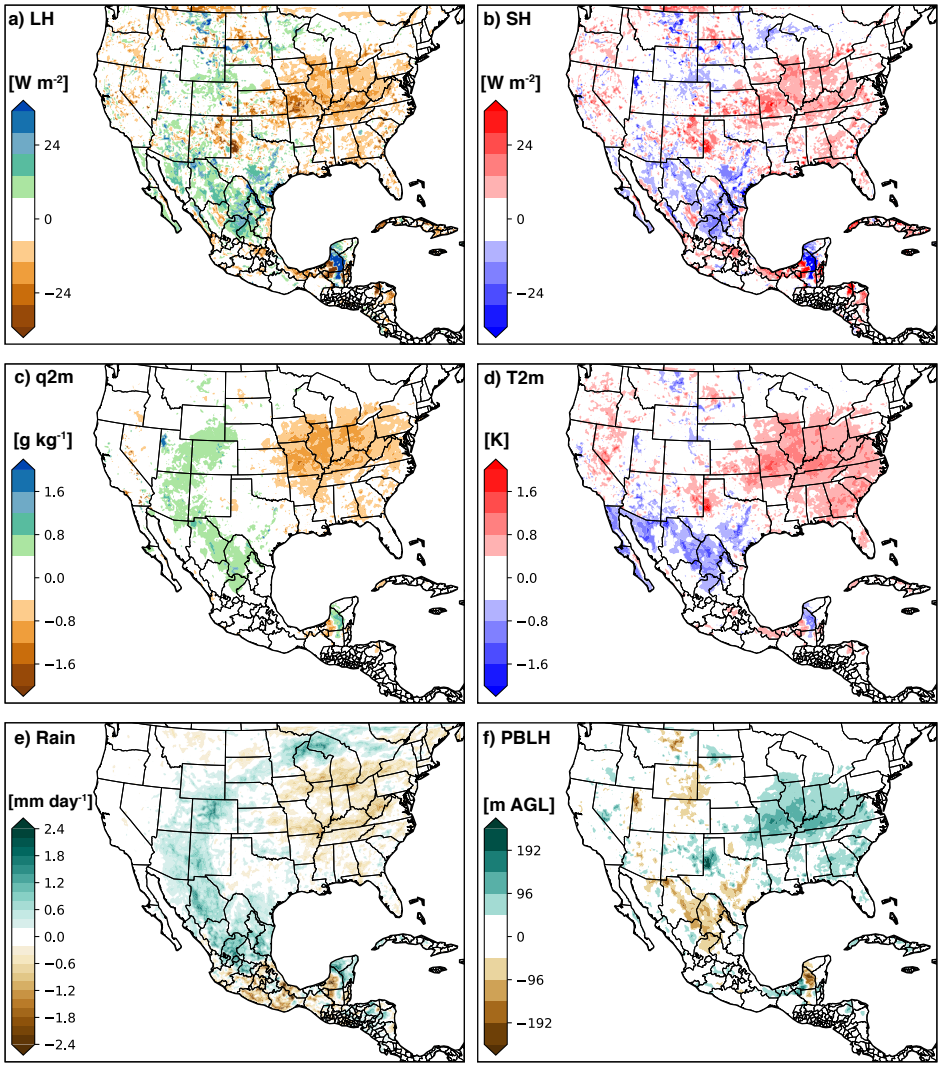

Figure 2.8: Three-year averaged JJA (2016–2018) model simulation differences (WRF-GSDE minus WRF-STATSGO) of (a) surface LHF (W m^{-2}); (b) surface SHF (W m^{-2}); (c) 2-m specific humidity (g kg^{-1}), (d) 2-m temperature (K); (e) precipitation (mm day^{-1}); and (f) PBLH (m AGL).

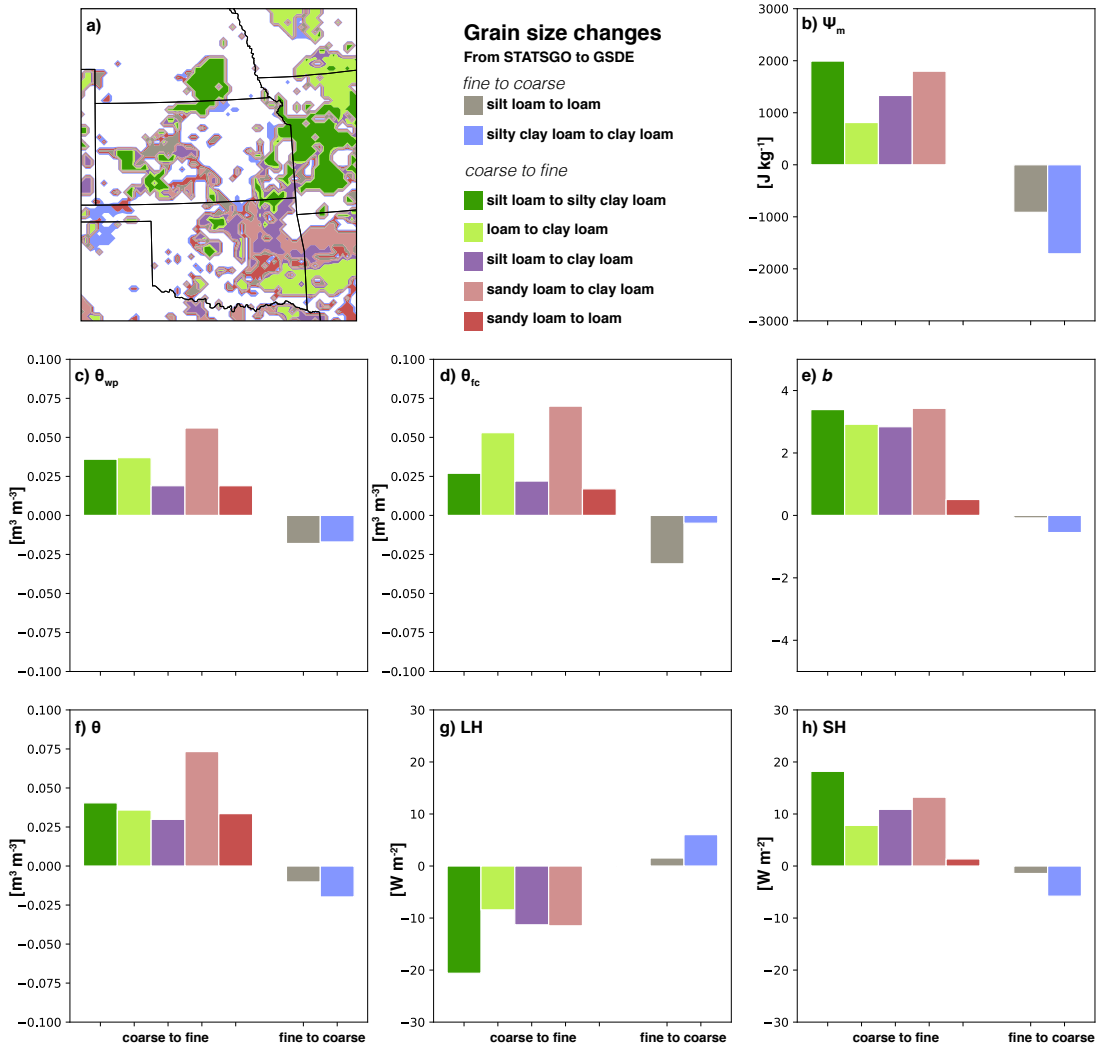

Figure 2.9: WRF-GSDE minus WRF-STATSGO differences averaged over seven specific soil category transitions most common in the GP sub-domain (approx. latitude: 32–41° N, longitude: 91–102° W). Changes in soil parameters: (a) soil categories (similar to Fig. 3); (b) matric potential (J kg^{-1}) calculated following Eq. 1 using average top layer soil moisture and appropriate parameters; (c) wilting point (m^3 m^{-3}); (d) field capacity (m^3 m^{-3}); and (e) the b parameter. Differences in the JJA 2016–2018 averages of: (f) volumetric soil moisture (m^3 m^{-3}); (g) LHF (W m^{-2}); and (h) SHF (W m^{-2}).

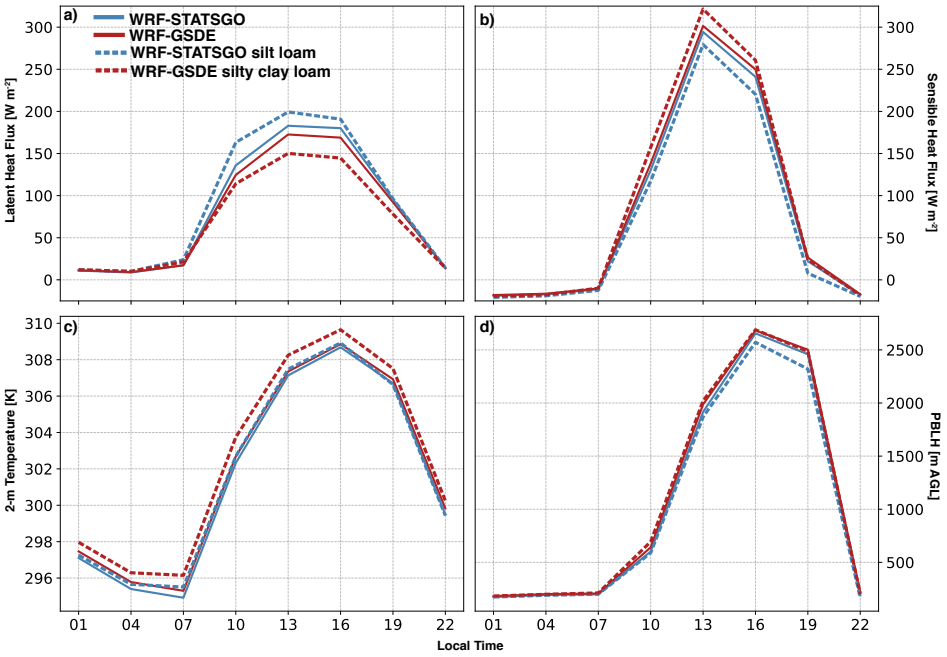

Figure 2.10: Area-averaged JJA 2016–2018 diurnal cycles of (a) LHF [W m^{-2}]; (b) SHF [W m^{-2}]; (c) 2-m temperature [K]; and (d) PBLH [m AGL] over the GP sub-domain shown in Fig. 9a. The full-region mean values for the WRF-STASGO simulation is shown in solid blue, while the full-region means for the WRF-GSDE simulation is in solid red. Dotted lines represent area averages only over the 468 grid spaces that transitioned from WRF-STATSGO silt loam (dotted blue), to WRF-GSDE silty clay loam (dotted red).

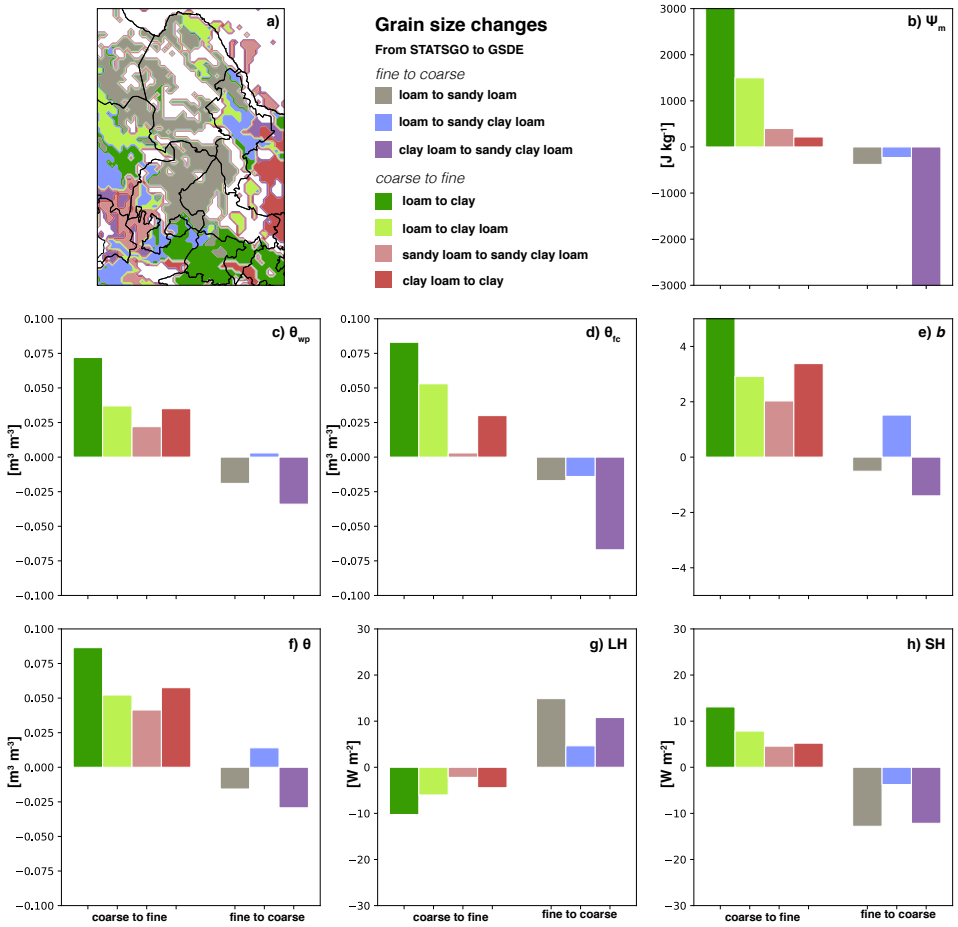

Figure 2.11: Similar to Fig. 9, except for the Central Mexico region (approx. latitude: 20–30° N, longitude: 98–105.5° W).

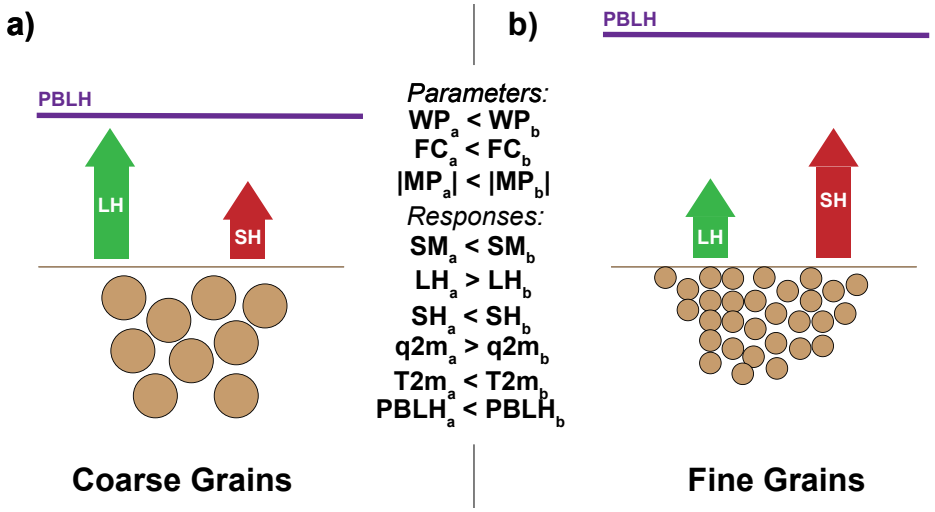

Figure 2.12: A schematic depicting the physical relationships established in Chapter 2. Coarse grain soils (a) are shown, along with (b) fine grain soils. Wilting point [WP; m^3 m^{-3}] and field capacity [FC; m^3 m^{-3}], and matric potential [MP; J kg^{-1}] are chosen as key parameter differences. Soil moisture [SM; m^3 m^{-3}], latent heat flux [LH; J kg^{-1}], sensible heat flux [SH; J kg^{-1}], 2-m mixing ratio [q2m; kg kg^{-1}], 2-m temperature [T2m; K], and planetary boundary layer height [PBLH; m AGL] are shown as comparative responses between both (a) coarse grains and (b) fine grains. The green arrows symbolize latent heat flux and the red arrows symbolize sensible heat flux.

Chapter 3: The Effects of Soil Representation in the WRF/CLM on the Atmospheric Water Budget

This chapter is currently under-going peer review in the Journal of Hydrometeorology.

3.1 Introduction

Soil science plays an increasingly prominent role in Hydrology and Earth System Science, partially motivating the creation of the International Soil Modeling Consortium [Vereecken et al., 2016], which, among other activities, promotes the study of soil processes within Earth system modeling frameworks. However, many challenges still exist: the implementation of soil processes in land surface models (LSMs) has been shown to introduce further GCM dependence on resolution [Bosilovich and Sun, 1998], while high variability is shown between the use of different combinations of soil textures, soil parameters, and hydraulic parameterizations [Verhoef and Egea, 2014]. Other results increasingly suggest that soil hydro-physical properties [Kishné et al., 2017] are regionally specific. The solutions to these challenges necessitate simultaneous observations of soil moisture, surface fluxes, and multiple horizons of soil properties [Mu et al., 2021]—an observational dataset that is not globally

achievable.

Despite these obstacles, the evolving soil sciences community has made remarkable strides in developing high-resolution global soil datasets [Hengl et al., 2017; Lannoy et al., 2014; Shangguan et al., 2014]. Estimates of soil hydro-physical properties have been compiled from novel regional measurement techniques Lu et al. [2020], physics-based relationships [Lehmann et al., 2018; Or and Lehmann, 2019; Zhang et al., 2018], and statistical mechanisms such as random forests Szabó et al. [2019] and other Pedotransfer Functions [PTFs; van Looy et al., 2017]. These are used to derive high-resolution soil hydro-physical property maps [Chaney et al., 2019; Dai et al., 2019a], which can be used to enhance coupled and uncoupled land surface model (LSM) simulations. See Dai et al. [2019b] for a review of global soil datasets used in Earth System models.

Despite the availability of global high-resolution soil hydro-physical property datasets, many LSMs remain dependent on look-up tables to associate soil textural categories with empirically derived hydro-physical properties. Look-up tables, while computationally efficient, require soil hydro-physical properties to remain discrete and linked to broad estimates of soil texture rather than continuous evolving quantities. Furthermore, the usage of a look-up table assumes (a) that soil properties are globally transferable, which often is not the case, and (b) that it is dependent on soil texture maps. Thus, at typical coupled modeling resolutions, the prescriptive soil texture categories can vary significantly between prominent datasets.

Furthermore, in the context of coupled modeling, soil hydro-physical properties and the choice of PTFs have been shown to impact soil moisture that in turn

affects surface water and energy fluxes [Ek and Cuenca, 1994; Weihermüller et al., 2021], surface heat fluxes [e.g., Peters-Lidard et al., 1998, etc.], and PBL evolution [Breuer et al., 2012; Kim and Entekhabi, 1998; Pan and Mahrt, 1987]. Further, land-atmosphere (L-A) interactions [Dirmeyer, 2011; Koster et al., 2004; Santanello et al., 2018; Seneviratne et al., 2010] are dependent on surface water and energy fluxes; therefore, if soil hydro-physical properties influence surface fluxes, they can also influence L-A interactions. The so-called "terrestrial leg" of L-A coupling links soil moisture via surface processes [Dirmeyer, 2011] to surface latent and sensible heat fluxes, while the atmospheric portion expands that relationship to describe the effect of surface fluxes on PBL evolution, clouds, and precipitation [Dirmeyer et al., 2014]. The specific role of surface properties in L-A coupling (including the role of soil texture and soil hydro-physical properties) has received less attention than, for instance, the relationship between soil moisture and precipitation [Eltahir, 1998; Findell and Eltahir, 1997; Hohenegger et al., 2009]. Though it has been shown that soil moisture alone does not dictate L-A coupling, but rather, it is the combined effect of soil moisture and surface characteristics that do it [Dennis and Berbery, 2021].

At and beneath the surface, soil hydro-physical properties can play a vital role in the terrestrial water budget, affecting evapotranspiration, and runoff. Clayey soils, with a lower infiltration rate, require more time to percolate water to lower levels, which can lead to increases in runoff immediately following a precipitation event[Duffková, 2013]. Sandy soils, on the other hand, quickly absorb moisture after rainfall. By a similar mechanism, after precipitation clayey soils can lead to pooling,

ponding and the associated increase in evaporation of standing water [Duffková, 2013]. However, if similar amounts of precipitation fall on dry naturally-compacted soils, it will be the coarse-grained soils that experience more evapotranspiration over time due to the effects of matric potential [Dennis and Berbery, 2021]. Sub-surface runoff generally increases for non-vegetated surfaces versus vegetated surfaces [Liao et al., 2016], and for compacted soil surfaces versus aerated and natural surfaces [Prats et al., 2021]. These mechanisms work to distribute soil moisture, which is critical to linking the land surface with the atmosphere.

After soil moisture is distributed, land–atmosphere interactions have been shown to create environments more (or less) conducive for convection to occur. Soil moisture conditions have been shown to affect thermodynamic instability [Holt et al., 2006b; Yin et al., 2015] and develop cross-boundary mesoscale circulations providing vertical motion and preferred initiation locations [Avissar and Liu, 1996; Lee et al., 2019; Zheng et al., 2021]. Similarly, the land properties can enhance or diminish the horizontal transport of moisture [Lee and Berbery, 2012; Lee et al., 2013; Yang and Dominguez, 2019], affecting vertically integrated moisture flux convergence, which is a critical component in the atmospheric water budget to evaluate continental water transport and partitioning [Rasmusson, 1968; Roads et al., 1994; Trenberth et al., 2007]. While these impacts have been studied from a general land surface perspective, the role of soil texture in these relationships has not been examined as much.

The role of soil texture in the terrestrial water budget has received quite a bit of attention, where-as the role of soil texture and its role in the coupled (L-A)

effects on the atmospheric water budget has not. This study aims to connect the atmospheric portion of L–A coupling to the impact of soil texture-modulated surface fluxes. It is hypothesized that the soil's hydro-physical properties, via their influence on surface fluxes will affect the thermodynamic instability (i.e., CAPE/CIN), as well as the dynamic moisture transports (i.e., atmospheric circulation), and ultimately influencing the atmospheric water budget.

Dennis and Berbery (2021) examined the soil properties' role on surface water and energy fluxes and near-surface states in a first study. This study advances their analysis of the impact on PBL evolution, thermodynamic environments for precipitation (i.e., atmospheric stability), dynamic precursors to precipitation (i.e., moisture transports), and atmospheric water budget. To this end, we compare the two sets of summer WRF simulations described in Dennis and Berbery (2021; hereafter DB21) using different soil texture datasets: one using the State Soil Geographic Dataset [STATSGO; NRCS Soil Survey Staff, USDA, 2012] soil texture dataset and the other using the Global Soil Dataset for Earth System Modeling [GSDE; Shangguan et al., 2014]. The experimental design is outlined in Section 2, followed by descriptions of the soil texture datasets. Section 3 will validate the model simulations using in-situ measurements and reanalysis. Section 4 will highlight the soil parameter-induced differences in the thermodynamic and dynamic environment and relate those differences to the atmospheric water cycle. Finally, section 5 provides our concluding remarks.

3.2 Experimental Setup

3.2.1 Model Design

The model configuration and simulations are the same ones used by DB21. We used WRF's Advanced Research version [WRF-ARW v. 3.9; Skamarock et al., 2008] to carry out simulations over three summers (JJA 2016–2018) to examine near-surface processes related to soil physics. In this study, we investigate how atmospheric processes can be related to soil physics. The model domain covers the continental United States (CONUS), Mexico, northern Central America, and southern Canada (See Fig. 1) at a 15-km horizontal resolution. There are 51 vertical layers, with 13 of them occurring in the lowest 1-km to improve boundary layer representation. The model parameterizations include a single-moment microphysics scheme [Thompson et al., 2008], the Rapid Radiation Transfer Model [Iacono et al., 2008], and the Betts-Miller-Janjić convective parameterization scheme [Janjić et al., 2001]. The PBL is represented using MYNN2, a second-order closure, a local PBL scheme [Nakanishi and Niino, 2006], and the compatible MYNN surface layer scheme to account for the interface between the land surface and the PBL.

As discussed in DB21, WRF is coupled with the Community Land Model version 4 (CLMv4 hereafter CLM). CLM is a land surface model developed and maintained by NCAR for use with the CESM1 global climate modeling system and has since been adapted for use coupled to WRF. CLM interacts with the atmospheric model to establish the lower boundary conditions related to the surface water and

energy budgets. CLM includes relevant hydrological variables and the partitioning of incoming radiation into its surface energy components. CLM incorporates the effects of vegetation, soil, and land use. It represents the soil-atmosphere-vegetation nexus using a resistance formulation and accounts for soil hydraulics using a classical understanding of fluid movement within porous media (e.g., Richards 1931). CLM has ten vertical soil layers increasing in thickness with depth and extending down to 3.42 m. A full technical description of CLM can be found in [Oleson et al., 2010]. CLM's performance has been reported thoroughly in the literature. First, against the NLDAS testbed experiment [Cai et al., 2014; Xia et al., 2017, 2012]. Second, in both offline and coupled mode (to CAM3.0) for climate-scale processes [Lawrence et al., 2007]. Third, in full offline mode examining parameterization improvements [Lawrence et al., 2011]. Lastly, the CLM coupled to WRF was evaluated to explore landslide detection and prediction [Zhuo et al., 2019] and assess the impact of soil properties on land-atmosphere coupling (DB21).

Representing soil physics requires knowing their hydraulic—or hydro-physical —properties. In models, they are usually derived as parameters specific to a soil texture classification. Then, a look-up table with parameters that correspond to each soil texture category is used. The look-up table parameters are based on empirical relationships obtained in laboratory experiments [e.g., Cosby et al., 1984]. This method assumes that categories are universal (i.e., sand in one area is the same as sand everywhere) and that they can be transferable to the real world—a topic that is becoming increasingly important for soil science research. The approach has the advantage that only the soil texture maps and the look-up table are needed to define

all the soil's hydro-physical properties; therefore, it is computationally inexpensive. However, the soil system and the land-atmosphere coupling do become dependent on the external soil texture databases.

Our goal is to determine the impact of these soil databases via their soil hydro-physical properties on land-atmosphere interactions and the atmospheric water budget. It is well understood that vegetation has a significant effect on surface fluxes, as well. Therefore, the simulations have been given the same vegetation assignments to avoid vegetation dependencies when assessing the impact of soil hydro-physical properties. This approach allows us to isolate the effect of the soils more easily despite the presence and role of vegetation.

3.2.2 Soil Databases

During the pre-processing stage for WRF the model's grid is defined. Its static fields are assigned to each grid space (i.e., soil type, vegetation type, topographical features) based on the provided databases. For a complete description of this process, please refer to DB21 and the supporting literature. For instance, land cover classes are defined by Moderate Resolution Infrared Spectrometer International Geosphere-Biosphere Programme (MODIS IGBP) data in default WRF settings. The default soil texture classifications in WRF are provided using the USDA STATSGO soil dataset [NRCS Soil Survey Staff, USDA, 2012]. For regions outside of the United States, the Food and Agriculture Organization (FAO) Soil Map of the World [FAO/UNSECO, 1971], which is about 5-km grid spacing, is employed.

Within the US, STATSGO is used. STATSGO was based initially on the FAO Soil Map of the World. Still, since then, it has expanded to include multiple additional high-resolution surveying campaigns supplemented with LANDSAT data over CONUS and US territories, where its current resolution is about 1-km.

As in DB21, the second soil texture database in this study, GSDE, was also based initially on the FAO Soil Map of the World. It uses numerous global surveying campaigns complemented with advanced statistical re-gridding procedures and machine learning to infer the soil parameters in under-surveyed regions [Dai et al., 2019a; Shangguan et al., 2014]. It is provided at 1-km globally and provides eight vertical levels of soil characteristics. GSDE offers a global 1-km resolution as opposed to STATSGO's 1-km resolution only over CONUS and US territories.

These datasets have many uses, but in modeling systems such as the WRF/CLM suite, the primary use is to determine the spatial distribution of soil textural classes that will link grid spaces to parameters in the accompanying look-up table. DB21 showed that the differences in soil classification between these two datasets are not randomly distributed, but, instead, they exist in coherent areas of reduced/increased soil grain size, which allows their impacts to be projected onto regional scales (See Fig. 1c).

Figures 1a and 1b present the model soil classifications as portrayed by the STATSGO database and the GSDE database. As shown in DB21, the primary soil classification in the Midwestern United States (hereafter, Midwest) is silt loam (green) in the STATSGO map. In contrast, in the GSDE map, many categories can be identified: silty clay loam (orange), sandy loam (light purple), and loam

(red). Each of these differences, or 'transitions,' represents a change in soil hydro-physical properties (i.e., a difference in how the soil interacts with water). Many differences can be identified between Fig 1a and Fig 1b, but the ten most common transitions are highlighted in Fig 1c. Notice a continuous area of transitions in Fig 1c that extends from the Texas-Arkansas border northeastward into Pennsylvania, the area here referred to as the Midwest. The majority of these transitions represent a decrease in average soil grain size.

Fig. 1 also shows the distribution of selected soil hydro-physical parameters as they have been assigned from the look-up table. Fig 1d and 1e show the wilting point (i.e., the lower limit for soil water storage under normal conditions). GSDE has the higher wilting point values (Fig. 1e, lighter yellow colors) throughout Missouri, Illinois, Indiana, Kentucky, and Ohio, as compared to the lower values in the same area in the STATSGO dataset (Fig. 1d, mostly orange colors). Similarly, the third row in the figure shows the field capacity (i.e., the maximum amount of moisture a soil can hold after free drainage occurs). Notice the higher field capacity values in GSDE (Fig. 1h, mostly blue colors) throughout the same region as the wilting point example compared to the lower values in the STATSGO dataset (Fig. 1g, light green colors).

The smaller size grains in GSDE imply that both field capacity and wilting point increase. Therefore, the majority of the map (Fig. 1f, 1i) shows that the differences in GSDE minus STATSGO hydro-physical properties have positive differences. As with wilting point and field capacity, other hydro-physical properties are connected to each soil textural classification. Thus, when one changes the locations

of the soil texture categories, in actuality, one is changing the spatial distribution of soil hydro-physical properties, which affects the way the soil interacts with the surface and sub-surface moisture. In the next section, we assess the impact of using these two soil datasets in separate regional climate simulations to support this assertion.

3.3 Model Performance and Variability

Both model performance relative to observations. Performance of the model is examined at two time scales, first the model's ability to reproduce sub-daily scales that determine the PBL processes in the lower troposphere, more specifically the diurnal cycle of key components. Second, the model's skill to represent the mean seasonal scales. The first step will be to contrast the diurnal cycle of the model's surface fluxes against selected Ameriflux flux towers. Then, the evaluation of the mean fields is done by contrasting mean fields with observationally-based forcings employed in land data assimilation systems. In our study, the substance lies in the differences produced by changes in soil categories between the models themselves. Thus, it is not an attempt to determine which model configuration performs better. Instead, comparing point measurements to model simulations is helpful to assess if the model simulations are sufficiently realistic.

Additionally, the model internal variability is assessed to understand how the simulations vary month-to-month within individual ensemble members and year-to-year between ensemble members. During the summer period there is often variability

between June and August signals in terms of hydrological cycle active. An analysis of the deviation between monthly performance will improve our understanding of signals present in the ensemble mean values.

3.3.1 Ameriflux towers

The diurnal cycle of surface latent and sensible heat fluxes in the WRF experiments are contrasted against three Ameriflux tower data (Fig. 2). An inverse distance-weighted average was used to interpolate the model data to each flux tower's location. The sites were chosen based on availability and continuity of data over the Central United States. They are the US–ARM Central Facility in Oklahoma [Biraud et al., 2020], the US-MMS in central Indiana [Novick and Phillips, 2020], and the US-IB1 in the rural suburbs of Chicago, IL [Matamala, 2019]. Table 1 presents the characteristics of each tower location.

The US-ARM site has a soil texture identified as silt loam, with a land cover of cropland that cycles between winter wheat, alfalfa, and soybeans (see Table 1). The model's land use assignment for all experiments identifies the site as grassland. The WRF-STATSGO simulation, hereafter WRF_S, has the appropriate soil texture for that location (silt loam). In contrast, the WRF-GSDE simulation, hereafter WRF_G, specifies clay loam—a relative reduction in soil grain size. According to DB21, smaller soil grains can reduce latent heat flux and increase sensible heat flux relative to the simulation employing STATSGO. Fig. 2a shows the US-ARM flux tower's JJA 2016–2018 mean diurnal cycle of latent and sensible heat fluxes

and compares them to WRF_S and WRF_G simulations. In terms of latent heat flux (solid lines), both model and observed diurnal cycles experience consistent timing in the maximum and minimum values, with latent heat flux increasing throughout the morning hours from about 0700 LT until about 1200 LT and decreasing as the sun sets around 1800 LT. The WRF_S simulation with silt loam soil type experiences the greatest average latent heat flux at the diurnal maximum (about +300 W m^{-2} at 1200 LT). As discussed in DB21, the WRF_G simulation has a smaller soil grain assignment (i.e., clay loam is finer than silt loam), and it shows reduced average latent heat flux throughout the diurnal cycle compared to the WRF_S. In terms of sensible heat flux, the WRF_G simulation has an increased diurnal maximum compared to the WRF_S (+15 W m^{-2}) and the in-situ measurements (+50 W m^{-2}).

Interestingly, in Fig. 2a, despite having a different soil texture, the WRF_G simulation has a smaller latent heat flux bias (about +75 W m^{-2}) versus about 100 W m^{-2} in WRF_S) compared to the in-situ observations at the diurnal peak, possibly related to erroneous vegetation assignments in the model. In reality, the crops grow throughout the summer months and are largest and most impactful by the July–August time frame. In contrast, the model is assigned grassland, which does not evolve throughout the season resulting in different hydro-physical characteristics. In this case, the differences could be due to improper vegetation assignment in the model, rather than to the impact of soil properties.

Figure 2b, presents the US-MMS Ameriflux site (39.323, –86.413). This site's information does not include soil type, but it is located in a deciduous broadleaf forest, as the model's simulations also show (see Table 1). The diurnal cycle of

latent heat flux in both model simulations are very similar to the observations at this site, rising up to about 275 W m^{-2} at the peak and falling off to near 0 W m^{-2} during the nighttime hours. Sensible heat flux, however, shows more of a difference between the two model simulations and the in-situ measurements. According to [Bonan et al., 2018; Fisher et al., 2017], the non-linear characteristics of canopy shading and sub-canopy turbulence are difficult to account for in models. Forest dynamics could then contribute to the differences in sensible heat flux between the simulations and in-situ measurements.

The third site, US-IB1 (Fig. 2c), is located in a rural suburb of Chicago, with silty clay loam as the observed soil type and cropland as the observed vegetation coverage (corn and wheat; see Table 1). In this instance, GSDE has the appropriate soil type assignment (silty clay loam), while STATSGO's is somewhat different (silt loam). Curiously, WRF_G has a lower performance than WRF_S in terms of latent and sensible heat flux biases. Both simulations have similar timing of the diurnal cycle, but both overestimate the magnitude of sensible heat flux and underestimate the magnitude of latent heat flux at the diurnal peak. Fig. 2c shows that with finer soil grains in GSDE compared to STATSGO, the WRF_G simulation yields reduced latent heat flux values and subsequently increased sensible heat flux following the surface energy balance, consistent with DB21 findings.

3.3.2 NLDAS2 Forcing

It is also relevant to examine the spatial structure of the surface variables in the model simulations. To this end, we employ as a proxy for observations the North American Land Data Assimilation System Version 2 (NLDAS2) forced by a set of diverse observations that have been processed to fit the NLDAS2 grid [Cosgrove et al., 2003]. We selected the 2-m temperature, 2-m specific humidity, and precipitation to compare against the WRF model products from this dataset. Due to differences in grid spacing, the WRF model data were bilinearly interpolated to the NLDAS2 grid (12-km grid spacing).

The NLDAS2 non-precipitation forcing data are derived from the North American Regional Reanalysis [NARR; Mesinger et al., 2006] analysis fields but are spatially interpolated to the finer 1/8° NLDAS2 grid. Additionally, the forcing data are temporally disaggregated from the 3-hourly NARR data to the NLDAS hourly timestep. The NLDAS precipitation data are a temporal disaggregation of a CPC gauge-based daily precipitation [Xie et al., 2007](Xie et al. 2007), combined with Doppler RADAR data, CMORPH data, and 3-hourly NARR data in a way that reflects the strengths of each dataset on the NLDAS grid (Xia et al. 2009).

Figure 3a presents the distribution of mean (JJA 2016–2018) precipitation from the NLDAS forcing dataset. The western United States is mostly dry during this period, with most areas experiencing 1 mm day^{-1} or less. While the monsoon precipitation in northwestern Mexico is strongest in JAS, its signal is already detected in JJA. In the Central United States, the characteristic gradient of increasing

precipitation from the front range of Colorado eastward into the Midwest is present, along with slightly elevated precipitation values along the eastern and southern US coastal regions.

Most models tend to have more difficulties in reproducing summer precipitation due to their dependence on imperfect parameterizations. Models often overproduce precipitation in regions near stationary lifting mechanisms (i.e., topography). In addition, the propagation speed of convective systems is reduced, resulting in increased daily precipitation values, especially in mountainous regions [Navale et al., 2020; Tripathi and Dominguez, 2013; Yun et al., 2020]. This is also the case of the WRF model. The differences (WRF_S – NLDAS) in mean (JJA 2016–2018) precipitation are shown in Fig. 3b. The overall model precipitation pattern is similar to that in observations (not shown), but regional biases are noticed. The western mountain region exhibits positive precipitation anomalies, while the opposite is true in most of the United States east of the Continental Divide. Negative biases are also observed along the eastern and southern US coasts, reaching precipitation of about –2 mm day^{-1}.

Figure 3c depicts the (JJA 2016–2018) mean 2-meter temperature from the NLDAS2 forcing dataset. The climatological features show high temperatures in the south-central US and in the southwestern US desert regions, with cooler values in the Rocky Mountains and the Pacific Northwest. Comparing WRF_S to NLDAS2 Forcing (Fig. 3d), the WRF_S simulation has a warm bias (+1–2 K) in the eastern and central United States and a cool bias (–2–3 K) in the Rocky Mountains. Because the resolutions of NLDAS2 and the WRF simulations are similar, we expect differences

due to grid interpolation to be negligible, though in extreme topography areas (i.e., the Rocky Mountains) some differences may arise.

In Fig. 3e, the mean 2-meter specific humidity is shown from the NLDAS2 Forcing. The climatology shows a northwest-to-southeast gradient of increasing specific humidity across the CONUS region, with maximum values along the Gulf Coast and southern Atlantic Coast states. Compared to NLDAS2 Forcing, the WRF_S simulation reveals a widespread dry bias (–1–2 g $\text{kg}^{-1)}$ that occupies most of the eastern part of the United States, with smaller positive biases (+0–1 g kg^{-1}) existing in the Western States.

The Midwestern US environment in the WRF_S simulation is both slightly warmer and slightly drier than the NLDAS2 forcing data. Still, compared to other model simulations, it is within a reasonable range. The WRF_G simulation displays an environment more similar to WRF_S than it is to NLDAS, but with even warmer and drier conditions in the Midwest. Comparing these variables between WRF_S and WRF_G is shown in DB21 (See their Fig. 8). This study aims not to rank the simulations in terms of accuracy but instead to investigate the implications of their soil-induced differences on free-running simulations.

3.3.3 Model Variability

An advantage of using an ensemble strategy is that multiple instances of similar physical responses given different initial conditions is more robust than considering a single simulation of a single time period. Therefore, it is important to understand

how the individual ensemble members evolve to know whether an apparent signal is robust throughout the duration of a simulation or if values dominate it in a specific time period. Given the dependence of ensemble-mean values on the individual members, particularly in cases when there are fewer members, it is necessary to evaluate how the simulations compare with respect to key variables in both an intraseasonal and an interannual way to ensure that collectively they are representative of an adequate ensemble distribution.

Considering the intraseasonal variability, Figure 4 shows estimated probability distribution functions of daily mean values for both domain-averaged precipitation and domain-averaged latent heat flux. Concerning precipitation, each month reports similar distributions of daily values. July has the narrowest distribution (Fig. 4a), indicating the most similarity day-to-day, with mean values near 3 mm day-1. June experiences the widest distribution with daily values approaching 6 mm day-1 on the upper tail of the distribution and a cluster of non-precipitating days. While the daily mean values in August are the most similar to the entire simulation mean distribution (black line).

Intraseasonal daily latent heat flux (Fig. 4b) displays a different behavior compared to intraseasonal daily precipitation, with domain-averaged daily values decreasing as the season progresses: the highest likelihood of high values in June, mid-range values in July, and highest likelihood of lower latent heat flux values in August. Consistent with the multi-modular distribution between the months, the full simulation-average daily values (black line) has a reduced peak but is much broader to encompass the month-to-month variability.

Contrasting interannual variability instead (Fig. 4c-d), precipitation and latent heat flux show similar and related patterns. First, for precipitation, Fig. 4c shows that 2017 is skewed towards the lower end of daily mean precipitation values, while 2018 is skewed slightly towards the upper end of the distribution. The daily values or precipitation from 2016 represent the best estimate of the ensemble mean. The distribution of interannual daily latent heat flux (Fig. 4d) echoes the same pattern as the distribution of interannual daily precipitation with less latent heat flux occurring on average each day in 2017, while 2018 experiences slightly higher than normal latent heat flux each day. The distributions of daily mean precipitation and latent heat flux can be related in two ways: 1) If more precipitation occurs, there could be more moisture available to transmit from the land surface to the atmosphere, increasing latent heat flux, or 2) if more latent heat flux occurs, there could be more conducive conditions for precipitation to occur leading to increased precipitation likelihood.

The advantage of using an ensemble is that by considering multiple simulated environments rather than a single simulated environment, you increase the likelihood that the system's responses are due to imposed conditions, rather than due to an unknown factor. Even though this set of simulations is small relative to other ensembles, there are no prominent outlying ensemble members lending confidence that the systems are responding similarly to the imposed conditions despite different initial conditions.

3.4 Changes in the Environment

3.4.1 Thermodynamic Drivers

The thermodynamic forcing of summer precipitation processes is related to the distribution of atmospheric instability. Areas with more convective available potential energy (CAPE) and smaller convective inhibition (CIN) are more conducive environments for initiating and sustaining precipitating systems. CAPE and CIN are highly dependent on low-level temperature and moisture and on the evolution of the PBL; therefore, because soil properties affect the surface water and energy fluxes, they influence atmospheric stability also.

The spatial patterns of latent and sensible heat fluxes are shown in Fig. 5. The WRF_S simulation mean latent heat flux (Fig. 5a) exhibits lower Western United States values, with higher values in the eastern United States. In the Midwest, values approach 150 W m^{-2} (Fig.5a). The differences between the two simulations (WRF_G – WRF_S; Fig. 5b) are consistent with the reduction in soil grain size—smaller grains in GSDE lead to reduced latent heat flux, as illustrated in the Midwest by the negative differences of about –15 W m^{-2}, or about 10% of the climatological value. These differences lead to differences in 2-m specific humidity of about –2 g kg^{-1} in the same region (DB21; their Fig. 8c)

When incoming energy can no longer remove moisture from the soil, it is instead partitioned into sensible heat flux. Therefore, mean sensible heat flux displays a similar (but opposite) pattern in the WRF_S simulation (Fig. 5c): larger values

in the western United States and lower values in the eastern United States. Differences between the two simulations (Fig. 5d) reveal an increase in sensible heat flux collocated with the soil texture-related negative differences in latent heat flux in the Midwest region, approaching about 15 W m^{-2} or about 15–20% of the climatological value in that region. These differences in sensible heat flux are collocated with positive differences in 2-m temperature of about +2 K (DB21; their Fig. 8d).

As soon as model simulation differences arise in low-level thermodynamic variables such as 2-m temperature and 2-m specific humidity, instability quantities will also be affected (i.e., CAPE and CIN). CAPE and CIN quantities are more sensitive to low-level temperature and moisture; thus, we computed them from near-surface variables. The summer average CAPE (JJA, 2016–2018) computed from the daily WRF_S output (Fig. 6a) exhibits a gradient from northwest to southeast with minimal values west of the Rocky Mountains and maximum quantities along the eastern and southern coasts. The gradient of CAPE is most pronounced through the Great Plains region and in the Midwest states. The primary feature in the CAPE differences map (WRF_G–WRF_S; Fig. 6b) is an area of reduced mean daily CAPE in the upper Midwest of 150–200 J kg^{-1} (i.e., 15–20% of the climatological value in that region). The smaller soil grain sizes restrict evaporation, leading to reduced latent heat flux, and enhanced sensible heat flux values. Thus, negative differences in CAPE are collocated with both the negative differences in latent heat flux (coincident with negative differences in 2-m specific humidity and the positive differences in sensible heat flux (coincident with increased 2-m temperature). Above the surface, these warmer and drier conditions related to the finer soil grains create an

environment with an elevated LCL in the WRF_G simulation (not shown) compared to the WRF_S simulation. The elevated LCL leads to a reduction in CAPE and, therefore, less conducive conditions for convection initiation and maintenance.

The JJA 2016–2018 mean pattern in CIN is slightly different from the CAPE pattern in the WRF_S simulation for this period (Fig. 6c). The eastern United States shows more elevated values than the western United States, similar to CAPE; however, CIN's maximum values occur in the Great Plains (about 200 J kg^{-1}). A gradient is formed from that location, decreasing in all directions. The differences (WRF_G–WRF_S; Fig. 6d) in CIN display a considerable reduction of CIN in an area similar and a little west of CAPE's negative differences. CIN's value can be sensitive to either temperature or moisture depending on the ratio of the environmental stratification to the moist potential temperature lapse rate [Crook, 1996]. That is, it depends on the lapse rate between the LCL and the LFC. The role of the surface is primarily to define the LCL level. The warmer and drier surface environment in the WRF_G simulation related to the soil grain size would increase the LCL height and reduce the distance between it and the LFC, in some cases, reducing CIN, thereby making it more likely that convection will initiate.

The differences in CAPE and CIN can be traced directly to the impact of reducing the soil grain size in the WRF_G simulation. Taken together, the differences indicate that the WRF_G environment has less energy available to sustain convection (CAPE: –150–200 J kg^{-1}), yet, in the Midwest, that energy is more easily accessible (CIN: –50 J kg^{-1}), resulting in a competing effect. While it is difficult to be certain, the differences in precipitation and the differences in CAPE share very similar spatial

distributions. The differences in CIN and, especially in CAPE, are directly related to the differences in surface fluxes; therefore, they are directly related to soil hydro-physical properties via soil texture.

3.4.2 Moisture Transports

The implications of changing the soil's hydro-physical properties extend beyond creating conducive or inhibited convective environments by thermodynamic means. By changing the structure and evolution of the PBL through adjusting the distribution of soil properties, low-level circulation and moisture transports are also affected. To evaluate these processes, integrated quantities are presented in Fig. 7: precipitable water, moisture transports, and moisture flux convergence (MFC). Mean values in the figure are consistent with previous analysis [e.g., Roads et al., 1994].

A characteristic increasing gradient in precipitable water, or column integrated water vapor, exists from the western deserts to the southeastern coastal regions in the WRF_S simulation (Fig. 7a), with the highest values occurring along the Gulf of Mexico coast in Florida in the Yucatan Peninsula. The precipitable water differences (WRF_G – WRF_S; Fig. 7b) describe a similar pattern to the differences in latent heat flux (Fig. 7b) with negative values occurring throughout the Midwest, again consistent with the area of smaller soil grain sizes. The differences in the Midwest are mostly restricted to the lower troposphere and reflect the differences in the boundary layer and near-surface moisture variables (DB21; their Fig. 8c). The finer soil grains in this region restrict evaporation and lead to drier conditions above the surface.

Additionally, there are positive differences in precipitable water throughout Central Mexico and extending northward along the Rocky Mountains towards northeastern Colorado and western Nebraska. These differences are consistent with the differences in moisture transports and their convergence.

The moisture transports are shown in Fig. 7c (vectors) along with moisture flux convergence (MFC, shaded), given by:

$$MFC = \frac{1}{g} \int_{p_{top}}^{p_{sfc}} \nabla \cdot (q\mathbf{V}) dp \tag{3.1}$$

where q is water vapor, $\mathbf{V}$ vector wind field, and g is gravity, the integral is computed on pressure coordinates. MFC has been smoothed using a two-dimensional Gaussian smoother based on the standard deviation of the raw field. The moisture transport vectors (1 shown every 20 grid points) indicate strong southerly flow from the Gulf of Mexico into the Central United States, a feature consistent with the Great Plains Low-level Jet location. The underlying contours denote negative MFC (or moisture flux divergence) in southern Texas and Northern Mexico in the low-level jet's entry region. At the terminus of the low-level jet, the vectors veer eastward into the Midwest, leading to an area of positive moisture flux convergence throughout the southern Appalachian Mountains and the US Southeast. Also, note the strong convergence (dark blue hues) along the western edge of Mexico, signifying the North American Monsoon location.

Figure 7d shows that changes in the soil properties induce differences in moisture transports (vector) and differences in moisture flux convergence (contours).

The WRF_G simulations show an increased southerly flow of moisture towards positive MFC differences in the Rocky Mountains, an area consistent with the positive differences in precipitable water (Fig. 7b). These differences emanate from Central Mexico, a place of increased soil grain size assignments in the WRF_G simulation. The differences in moisture transports in the Midwest indicate a northward extension of the Great Plains low-level jet moisture transport and concurrent veering throughout Nebraska and extending northeastward towards Wisconsin and Indiana. The vectors along the eastern coastal region show enhanced northerly transport of moisture. Along southern coastal US, it shows enhanced easterly transport of moisture culminating in a net cyclonic circulation of moisture transports in the eastern US encircling the area of finer soil grains in the WRF_G simulation. The underlying moisture flux convergence differences are predominantly positive in the Midwest, suggesting that the WRF_G simulation has increased moisture flux convergence in the same region.

In general, the larger sensible heat flux due to soil properties instigates enhanced turbulent kinetic energy in the boundary layer leading to higher planetary boundary layer heights. The interaction of this PBL kinetic structure with the low-level winds can lead to either enhanced or diminished horizontal flows at a given height, as seen here. This agrees with previous findings where warm anomalies can lead to enhanced meridional moisture transports [Yang and Dominguez, 2019]. Furthermore, moisture transports are predominantly low-level phenomena because most atmospheric moisture is in the lower troposphere. In some cases, the height of the strongest winds in the boundary layer is altered, resulting in an alignment of strong

winds and high moisture content and, therefore, enhanced moisture transports (such as in Iowa and Illinois in WRF_G). In other cases, the height of the strongest winds is separated from the concentrated moisture, leading to reduced moisture transports (such as along the Gulf Coast in WRF_G). In both cases, the corridors of intense winds and the areas of enhanced moisture in the PBL are directly influenced by surface moisture and energy fluxes, which have been altered by changing the soil texture assignments.

3.4.3 Atmospheric Water Budget

The primary components of the atmospheric moisture budget are precipitation (P), evapotranspiration (ET), and the vertically integrated moisture flux convergence (MFC). Commonly, the change in water content in an atmospheric column over time is included ($\frac{\delta W}{\delta t}$), but this term is much smaller than the other three, so it is left out of this first-order analysis. The atmospheric water budget can be equated through the following relationship:

$$MFC = P - ET + R \tag{3.2}$$

where, R, is a residual term, which accounts for any imbalances. This simple budget equation states that the moisture entering a given area (by moisture flux convergence and evapotranspiration) is equal to the water precipitating from that area. It is a relationship that has been fundamental to water budget studies for decades [Berbery and Rasmusson, 1999; Li et al., 2013; Rasmusson, 1968; Roads et al., 1994; Trenberth

et al., 2007]. The individual terms of Eq. 2 are shown in Figure 8, and the values over the Midwest region are expressed in Table 2.

Figure 8a shows the (JJA 2016–2018) mean precipitation from the WRF_S simulation. Enhanced P values are shown in areas of topography (the Rocky Mountains and throughout the Appalachian Region), and there is an increasing gradient of precipitation from the Rocky Mountains eastward to the Atlantic and Gulf Coasts similar to the NLDAS Forcing (Fig. 3a) but with smaller values. The differences due to soil texture changes in the simulations (WRF_G – WRF_S; Fig. 8b) depict positive P values throughout the Rocky Mountains, consistent with the increased precipitable water and the positive differences in MFC. However, in the eastern United States, particularly in the Midwest, the differences are primarily negative despite enhanced moisture convergence. Instead, the differences in the Midwest are similar to the differences in precipitable water (Fig. 8b).

Where WRF_S experienced more rainfall compared to the NLDAS forcing (Fig. 3b), WRF_G experiences even more rainfall than WRF_S (i.e., through the mountainous western United States). Similarly, where WRF_S experienced less rainfall than the NLDAS Forcing, WRF_G experienced less rainfall than WRF_S (i.e., through the Midwest). Furthermore, the negative differences in P are located in (and just east of) the region of reduced mean CAPE (Fig. 6b). In the Midwest, there appears to be a higher correspondence between the differences in CAPE (Fig. 6b) and precipitation (Fig. 8a), than there is between MFC (Fig. 8f) and precipitation suggesting that precipitation in this region is more sensitive to thermodynamic instability than it is to dynamic moisture transports. Regardless, there are significant differences in

the precipitation environments caused by both dynamic and thermodynamic means. Each of the differences is related directly to surface fluxes, which have been modified by using the differing soil category datasets.

Three-year JJA-averaged ET from the WRF_S simulation is represented in Fig. 8c, with the differences (WRF_G–WRF_S) of the same quantity in Fig. 8d. The highest values of ET in WRF_S are located along the Appalachian Mountains, with maximum values nearing 4.5 mm day^{-1}. The differences show that the largest continuous area of negative differences is collocated with the area of decreasing soil grain size in the Midwestern United States (Fig. 1c). The soil hydro-physical properties associated with soil grain size directly affect ET because smaller soil grains retain water more strongly at a given value of soil moisture than larger soil grains. This retention both restricts and reduces bare soil evaporation and restricts uptake from root systems, thus reducing transpiration, as shown in DB21.

The largest continuous area of negative ET differences (Fig 8d) is also collocated, with the largest negative differences in P (Fig. 8b). Enhanced ET modifies the thermodynamic instability (i.e., CAPE/CIN; Fig 6) to create an environment more or less conducive for precipitation. In WRF_G, the ET is reduced due to the soil's hydro-physical properties, creating drier conditions above the surface (see DB21; their Figure 8c). This leads to negative differences in CAPE (Fig. 6b) in the same region. The differences in ET (about 1 mm day^{-1}) represent about 20% of the simulation-average value of ET. The differences in precipitation in this area (about 0.75–1.0 mm day^{-1}) consequently also represent about 20% of the three-year JJA-averaged value.

According to Table 2, ET has large values for each month and in the seasonal mean in both simulations. The land surface is a source of moisture in the summer months, with ET at its most active compared to any point throughout the annual cycle [Berbery, 2003]. Previous studies have suggested the ET is particularly difficult to simulate and is often over- or under-estimated in modeling frameworks. A large part of this difficulty is related to the lack of directly observed ET, therefore relying on an attempt to represent meter-scale land surface heterogeneity, including the effects of vegetation and soil hydro-physical properties in a much larger model grid.

Moisture flux convergence for WRF_S is shown in Fig. 8e, and differences between the model simulations are shown in Fig. 8f. MFC differences tend to agree with the differences in P: in central Mexico, positive differences in MFC are collocated with positive P differences. Similarly, there are modest positive differences in MFC throughout the Rocky Mountains in an area where there are also positive differences in P. However, there are mostly positive differences in MFC in the Midwest, but there are primarily negative differences in P. According to Table 2, in the Midwest, MFC has the smallest values compared to both P and ET. This is perhaps unsurprising: one of the main contributors to MFC is the Great Plains low-level jet which is maximized in the spring, not the summer months.

Additionally, the summer months are primarily void of synoptic-scale mid-latitude cyclones that contribute significantly to moisture advection and convergence/divergence. This result suggests that MFC is not necessarily the primary driver of precipitation, and other effects (e.g., land surface forcing) may be taking place. Nonetheless, this study shows that through the changes in soil hydro-physical

properties, the boundary layer is altered, affecting the low-level winds and the general circulation as it applies to the atmospheric water budget.

3.5 Conclusions

This study explored the effects of soil hydro-physical properties on atmospheric stability and the atmospheric water budget. To this end, three-year JJA regional WRF simulations employing different external soil texture databases were conducted. First, the well-known soil databases, STATSGO and GSDE, are used to assign soil texture categories to model grid spaces. Then those assignments are used with an accompanying look-up table to insert the appropriate soil hydro-physical property when necessary. Look-up tables are convenient from a computing efficiency standpoint. Still, they assume that soil properties associated with a soil texture category in one location are the same as that category's properties everywhere, which may not be the case. By changing the external soil database, the spatial patterns of the soil's hydro-physical properties are changed. Therefore, they affect the interactions between surface and sub-surface moisture and the interactions between the soil and the atmosphere.

The STATSGO dataset provides 1-km resolution over the contiguous United States and is developed using statistical techniques to combine multiple surveying campaigns and complementary satellite remote sensing techniques. The GSDE dataset is a modern advanced soil texture dataset developed using a more sophisticated approach based on machine learning techniques. It provides global 1-km

horizontal resolution soil data to be used primarily for Earth System modeling purposes. These two datasets represent premier estimates of soil texture, and each is widely used. However, as is evident in Fig. 1, they exhibit substantial differences. Namely, the GSDE dataset represents a reduction in soil grain size throughout the Midwest United States.

It has been shown that reducing the soil grain size leads to a reduction in latent heat flux and an increase in sensible heat flux for a given value of soil moisture (DB21). The changes in fluxes via soil texture altered low-level humidity and temperature leading to differences in three-year JJA-averaged thermodynamic instability characteristics. In the Midwest, the WRF_G environment experienced a drop in mean CAPE. Reduction in CAPE signifies a reduction in energy available to sustain convection. However, that area and areas just west of the Midwest also experienced a reduction in CIN. The net effect of reducing both CIN and CAPE is an environment with less energy to sustain convection (smaller CAPE). Still, that energy is more easily accessed (smaller CIN), resulting in a competing effect for precipitation processes. The timing and location of the precipitation differences suggests a closer relationship to the differences in CAPE rather than the differences in CIN.

Changes in surface fluxes due to the soil's hydro-physical properties also have dynamical implications, affecting atmospheric moisture transports and vertically integrated moisture flux convergence. Differences in sensible heat flux lead to changes in turbulent kinetic energy (not shown) and PBL growth. In this case, those interactions led to enhanced horizontal flows, such that a main general circulation feature, the Great Plains Low-level Jet, was elongated, and in the exit region, the

WRF_G simulation indicated stronger veering into the upper Midwest. Similarly, along the southern coastal states, there was a net easterly return flow, connecting a net cyclonic rotation of moisture transports encircling the area of reduced soil grain size in the WRF_G simulation.

Additionally, it has been shown that changing the soil hydro-physical properties can affect each term in the atmospheric water budget: P, ET, and MFC. The largest differences were shown in seasonal mean ET, a direct relationship in which smaller soil grains lead to reduced ET via the mechanisms described in DB21. Lesser but still apparent differences were found in MFC that are related to two mechanisms: 1) soil-related differences in low-level atmospheric moisture and 2) differences in low-level horizontal winds related to soil-modulated surface heat fluxes. Furthermore, the changes in continental precipitation depend on the type of precipitation regime: ones that resemble and appear to be dependent on MFC (i.e., arid regions throughout Mexico and the Rocky Mountains), and ones that are more dependent on the thermodynamic environment (i.e., the Midwest). Both regimes seem to be affected by soil properties through various mechanisms. The results of this study suggest that uncertainties in the definition of soil hydro-physical properties can lead to differences of the order of 15–20% of the mean values in the atmospheric water budget in summer.

Finally, this work is novel because it connects surface characteristics (i.e., soil properties) to both atmospheric thermodynamic instability and large-scale atmospheric circulations fundamental to the hydrologic cycle. Using L-A interactions, we have shown that soil properties affect surface fluxes, which alter the lower atmo-

sphere to ultimately influence regional precipitation characteristics. These findings are important to the consideration of soil representation in LSMs and will be helpful in diagnosing the land surface's role in sub-seasonal-to-seasonal prediction.

3.6 Final Summary of Physical Relationships

This study endeavored to connect prescribed land surface properties to atmospheric stability and the general circulation by means of the atmospheric moisture budget. The soil properties were altered by providing the model pre-processing system with different global soil texture databases. As discussed in Chapter 2, these datasets represent very different estimates of soil states with a notable negative differences in soil grain size in the Midwestern United States in the GSDE dataset compared to STATSGO. According to DB21, a reduction in soil grain size reduces mean latent heat flux and a corresponding increase in sensible heat flux because the soil retains moisture more strongly due to its adsorptive and capillary properties quantified through various soil characteristics like matric potential. In this study, reduced latent heat flux and increased sensible heat flux due to soil properties is shown to affect the coupled land-atmosphere system through both thermodynamic and dynamic means, eventually influencing precipitation. The essential aspects of these relationships are illustrated schematically in Fig. 3.9.

The thermodynamic environment is assessed using both convective available potential energy (CAPE) and convective inhibition (CIN) as proxies for atmospheric thermodynamic instability. CAPE quantifies the energy per mass of air available to

support and maintain convection. In areas with restricted latent heat flux and increased sensible heat flux due to smaller soil grain sizes (i.e., the Midwest), there was a corresponding reduction in mean surface-based CAPE in the GSDE simulation, denoted by negative differences in the ensemble mean fields (red font in schematic Fig. 3.9). The decrease in surface-based CAPE is because of the warmer and drier conditions near the surface resultant from differences in surface sensible and latent heat fluxes. The surface fluxes responded to the changes in soil texture; therefore, the differences in CAPE can also be related to differences in soil texture. The negative differences in CAPE in the Midwest signify an area with less energy to sustain convection in the ensemble mean (red text in schematic Fig. 3.9).

Following a similar mechanism, convection inhibition (CIN) is calculated based on low-level temperature and moisture, as well as atmospheric stability near the top of the PBL. Because the calculation of CIN is dependent on surface temperature and moisture values, it also responds directly to the decreased moisture and increased temperature associated with the soil-related reduction in latent heat flux and the increase in sensible heat flux. The warmer and drier atmospheric conditions near the surface led to negative differences in CIN in the Midwest in the GSDE simulation (green text in Fig. 3.9); therefore, the simulation with smaller soil grains had less energy available for convection (–CAPE), but that energy was easier to access (–CIN).

The low-level temperature and moisture quantities in CAPE and CIN are fundamental to determining the final atmospheric stability characteristics. In this way, both can be linked directly to latent and sensible heat fluxes. The surface heat

fluxes have been shown to respond to soil characteristics and soil moisture; therefore, changing the soil characteristics can lead to important differences in atmospheric stability.

The dynamic environment is linked to the land surface primarily through sensible heat flux. Increased sensible heat flux enhances surface-based turbulent kinetic energy in the boundary layer. The turbulent layer causes the boundary layer height to grow and decay diurnally. Horizontal winds in the boundary layer can either constructively or destructively interfere with the turbulent eddies. This can cause locally enhanced or diminished horizontal flows at low levels, which affects both horizontal transport of moisture via advection and the horizontal convergence/divergence of that moisture. In the Midwestern United States, the reduction of soil grain sizes led to an increase in sensible heat flux and a reduction in surface latent heat flux. This caused an increase in low-level moisture transports throughout the Central United States into the Midwest (light blue arrows in Figure 3.9b), and a corresponding increase in the convergence of that moisture in the exit region of the enhanced flow (black text in Fig. 3.9).

Large areas of differences in surface sensible and latent heat fluxes can also lead to more regional and continental-scale differences in circulation. In the Eastern United States, there is a net anti-cyclonic circulation apparent in the vertically-integrated moisture flux difference field, which indicates a weakening of the continental cyclonic circulation of moisture transports. Due to the differences in soil grain sizes, it is co-located with a large area of reduced latent heat fluxes and increased sensible heat fluxes. This circulation is less apparent in the wind field (not

shown), and is likely due to differences in the gradient of atmospheric moisture.

Through both thermodynamic and dynamic means, soil characteristics have been shown to alter each term of the atmospheric water budget, given by:

$$P - E = \frac{1}{g} \int_{p_{top}}^{p_{sfc}} \nabla \cdot (q\mathbf{V}) dp \tag{3.3}$$

where the RHS represents vertically-integrated MFC. In this framework, soil characteristics have altered ET directly due to soil properties interacting with soil moisture. Differences in precipitation in the Midwest and throughout the western mountain corridor were related to changes in surface fluxes through differences in atmospheric stability (CAPE/CIN) and moisture transport. Differences in vertically-integrated MFC suggested a relationship between surface fluxes and the horizontal wind field, such that moisture transports were enhanced and diminished to increase convergence in an area of reduced soil grain sizes and the corresponding differences in fluxes (i.e., the Midwest). Precipitation was discussed via thermodynamic and dynamic mechanisms. It has been shown that differences in surface fluxes caused by soil characteristics have influenced atmospheric stability, the horizontal transport of moisture, and the resulting regional precipitation characteristics.

Location Lat, Lon	Source	Soil Type	Veg. Type
US–ARM 36.605, -97.485	Flux Tower	silt loam (nearby)	CRO; winter wheat, soy, alfalfa
	STATSGO	silt loam	grasslands
	GSDE	clay loam	grasslands
US–MMS 39.323, -86.413	Flux Tower	*unspecified*	Decid. Broadleaf Forest; $> 60\%$ coverage
	STATSGO	silt loam	Decid. Broadleaf Forest
	GSDE	loam	Decid. Broadleaf Forest
US–IB1 41.859, -88.222	Flux Tower	silty clay loam	CRO; corn, soybean
	STATSGO	silt loam	urban, cropland
	GSDE	silty clay loam	urban, cropland

Table 3.1: Describes the characteristics of each Ameriflux Tower site according to the Site Metadata compared to the characteristics of the associated grid spaces in both model environments.

	WRF_S				WRF_G			
3-year mean	**P**	**MFC**	**ET**	**Res**	**P**	**MFC**	**ET**	**Res**
June	2.95	0.55	4.72	1.22	2.83	0.67	4.56	1.06
July	2.55	0.92	4.12	0.64	1.98	1.11	3.64	0.55
August	1.81	1.17	2.87	-0.11	1.57	1.84	2.52	-0.89
Total	2.44	0.88	3.90	0.58	2.13	1.21	3.57	0.24

Table 3.2: The main components of the atmospheric water budget are shown from the Midwest: precipitation (P), moisture flux convergence (MFC), evapotranspiration (ET) and the residual (RES). Single-month averages are included as well as the full-period means. All units are mm day^{-1}.

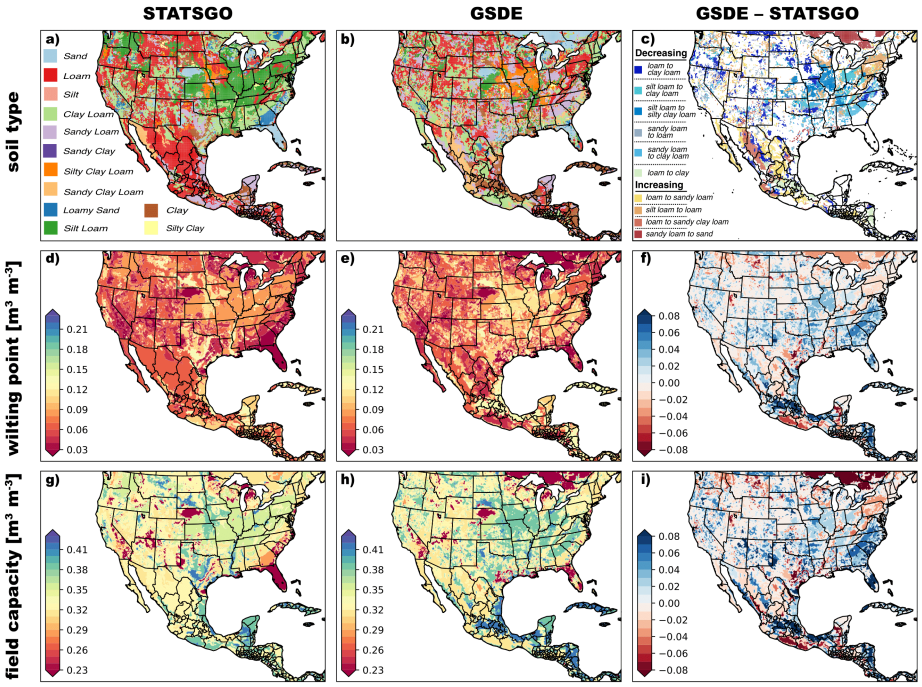

Figure 3.1: Soil category assignments are shown for (a) STATSGO, (b) GSDE, and (c) for the ten most common soil category transitions. The soil categories (a and b; adapted from DB21, their Fig 1a, 1b, respectively) are defined by the key in (a). The transitions (c) are organized by change in grain size with larger-to-smaller (i.e., decreasing grain size) transitions in cool colors, and smaller-to-larger transitions (i.e., increasing grain size) in warm colors. The assigned wilting point is shown for (d) STATSGO, and (e) GSDE, as well as (f) the differences (GSDE–STATSGO; e–d). The field capacity for (g) STATSGO and (h) GSDE is shown, as well as (i) the differences (GSDE–STATSGO; h–g) in field capacity.

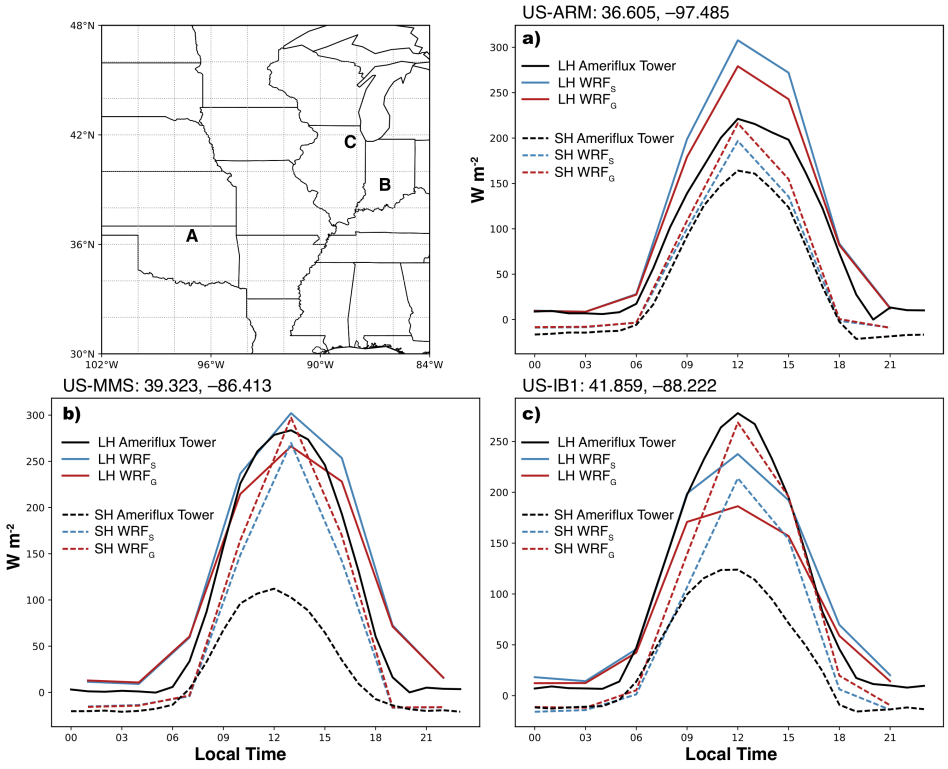

Figure 3.2: The diurnal cycle of latent (W m^{-2}) and sensible heat flux (W m^{-2}) the model simulations are compared to Ameriflux tower in-situ flux measurements. The location of each tower is given as lat/lon coordinates, and it is shown in the inset map. Solid lines represent latent heat flux, while dotted lines show sensible heat flux. The Ameriflux towers (black) are compared to WRF_S (blue) and WRF_G (red) at each flux tower location.

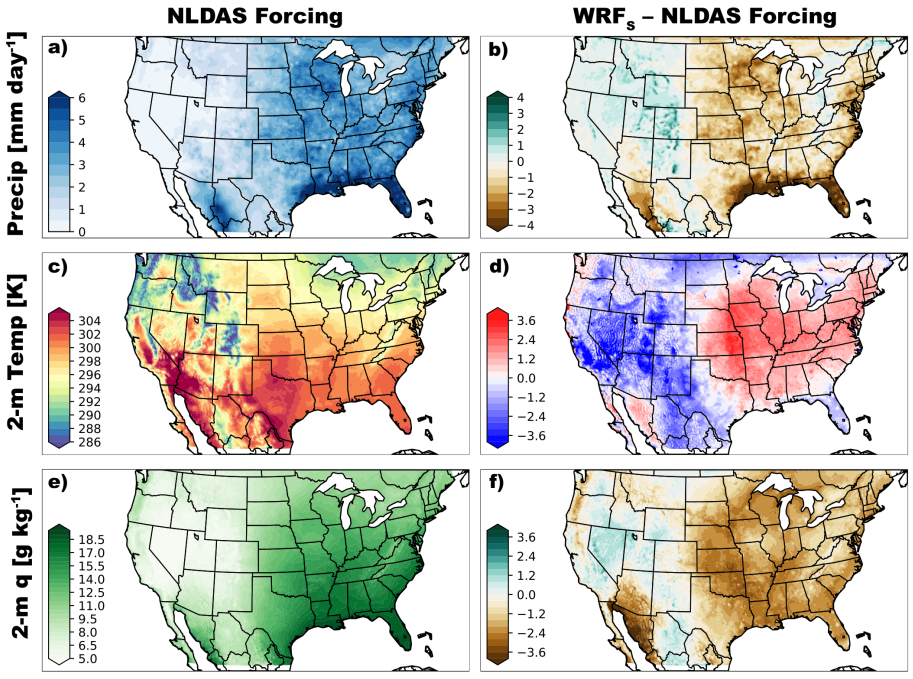

Figure 3.3: Meteorological fields from the NLDAS Forcing are shown in the left column: (a) precipitation (mm day^{-1}), (c) 2-m temperature (K), and (e) 2-m specific humidity (g kg^{-1}). Differences (WRF$_S$ – NLDAS Forcing) are shown in the right column bilinearly interpolated to the NLDAS grid: (b) precipitation (mm day^{-1}), (d) 2-m temperature (K), and (f) 2-m specific humidity (g kg^{-1}).

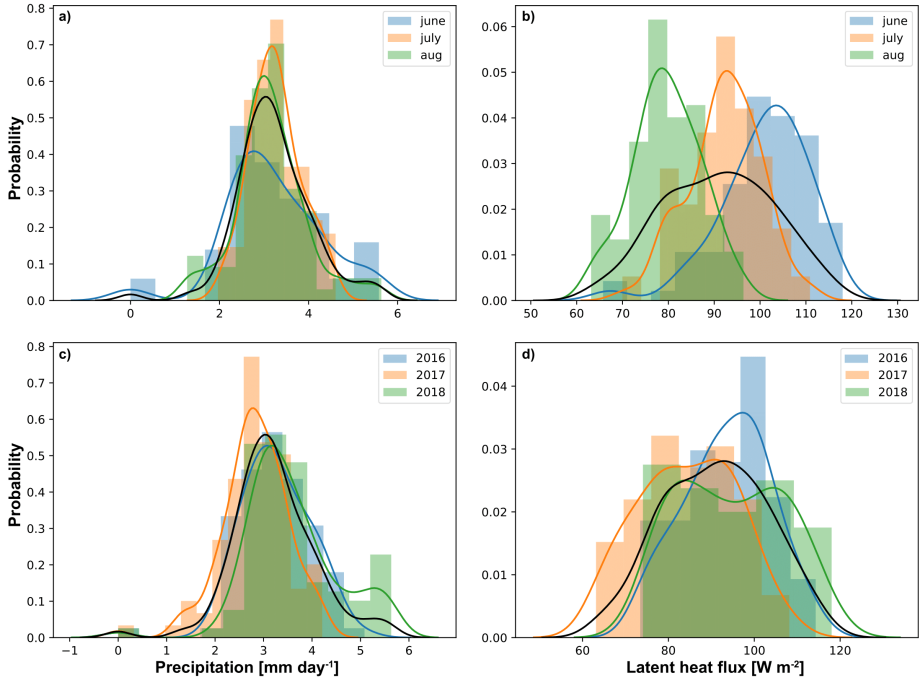

Figure 3.4: Domain-average daily mean values of (a and c) precipitation and (b and d) latent heat flux are shown as estimated probability distribution functions. Monthly analysis (a and b) of June (blue), July (orange), and August (green) are shown, as well as yearly analysis (c and d) of 2016 (blue), 2017 (orange), and 2018 (green). The full ensemble mean distribution is shown in black for each variable.

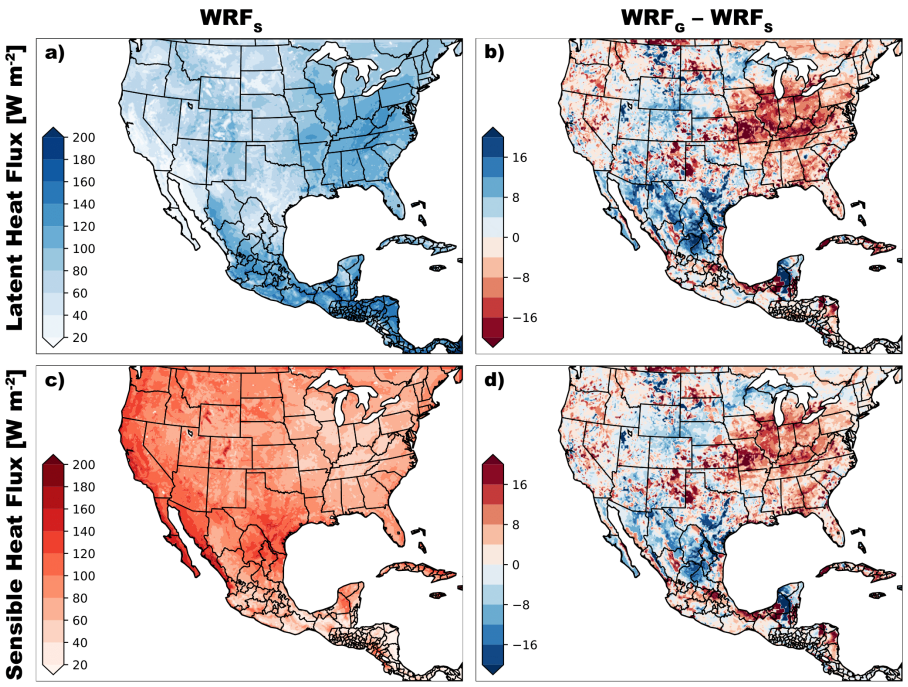

Figure 3.5: Three-year JJA-averaged surface (a) latent heat flux (W m^{-2}) and (c) sensible heat flux (W m^{-2}) maps are shown for the WRF$_S$ simulation as well as the differences (WRF$_G$ – WRF$_S$) in (b) latent heat flux and (d) sensible heat flux, which were adapted from DB21 Fig. 7c and 7d, respectively.

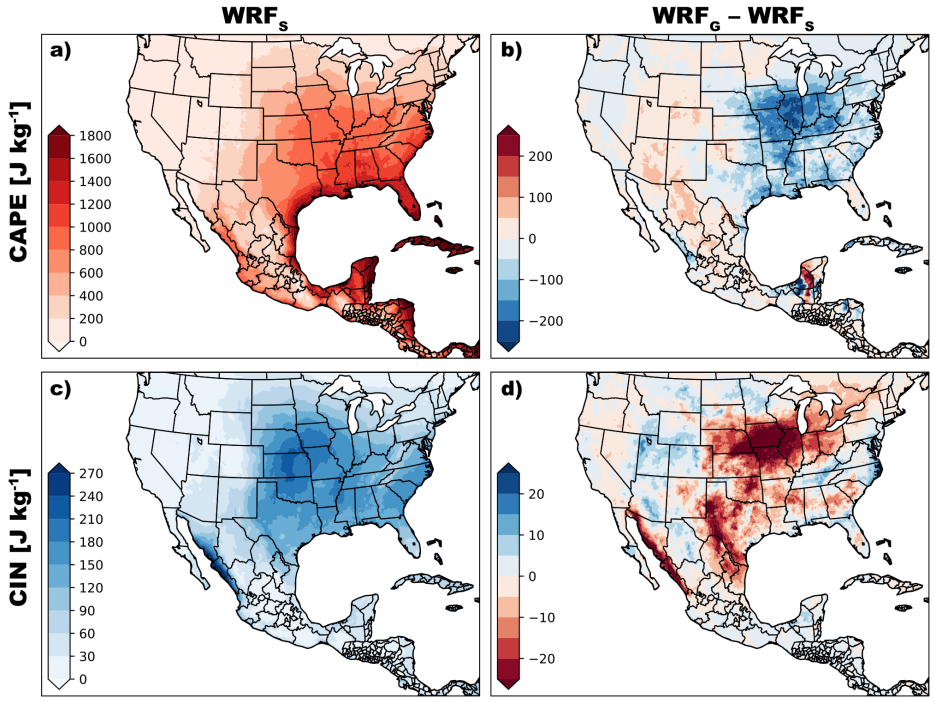

Figure 3.6: Three-year JJA-averaged (a) CAPE (J kg^{-1}) and (c) CIN (J kg^{-1}) maps are shown for the WRF$_S$ simulation as well as the differences (WRF$_G$ – WRF$_S$) in (b) CAPE and (d) CIN.

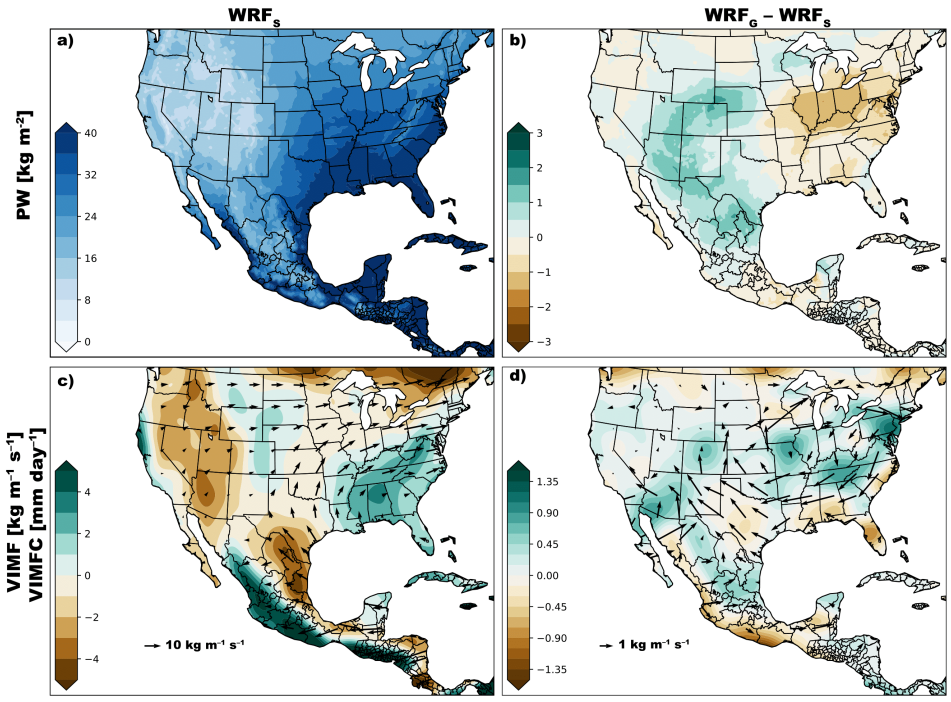

Figure 3.7: Three-year JJA-averaged quantities are shown for the WRF$_S$ simulation in the left column (a,c,e), and the differences (WRF$_G$–WRF$_S$) in those quantities are shown in the right column (b,d,f). The first row is precipitable water (kg m^{-2}). The second row displays vertically-integrated moisture flux convergence (mm day^{-1}; shaded), and overlaid moisture flux vectors (kg m s^{-1}; see keys for standard vector sizes).

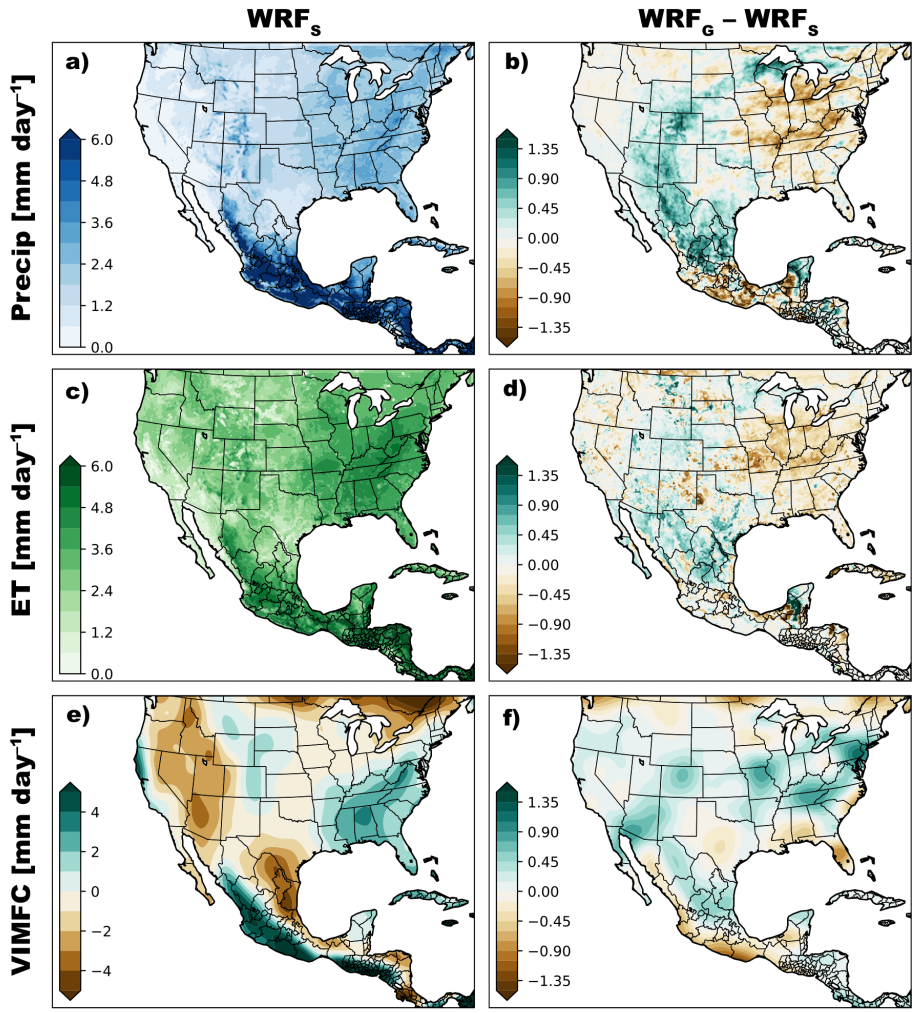

Figure 3.8: The main components of the three-year JJA-averaged atmospheric water budget are displayed for the WRF$_S$ simulation in the left column: (a) P, (c) ET, and (e) MFC; while, the differences (WRF$_G$ – WRF$_S$) in simulation-averaged quantities are shown in the right column: (b) P, (d) ET, and (f) MFC. All units are mm day^{-1}).

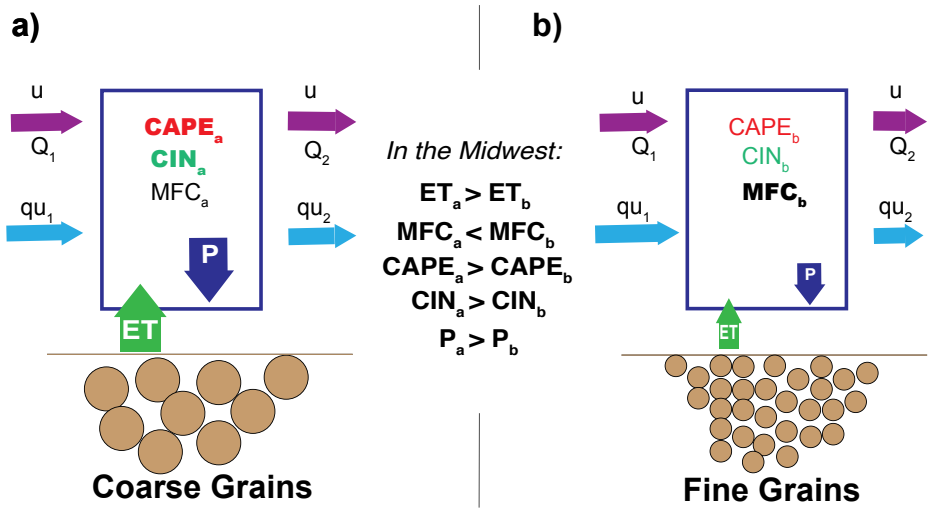

Figure 3.9: A schematic depicting the physical relationships established in Chapter 3. In the Midwest, in the simulation with larger soil grains (a) there was an increase in ET (green arrow) compared to the same area with smaller soil grain sizes (b). The simulation with larger soil grains (a) had an increase CAPE (bold red text), and CIN (bold green text), and Precipitation (P; large dark blue arrow). The simulation with smaller grain (b) had an increase in MFC (bold black text), resulting from differences in horizontal winds (u; purple arrows), low-level moisture (Q), and the convergence of moisture flux vectors (light blue arrows).

Chapter 4: Soil Hydro-physical Parameter Uncertainty Leads to Differences in Simulated Land–Atmosphere Coupling

The work presented in this Chapter is undergoing preparation for submission to the Journal of Hydrometeorology in the near future.

4.1 Introduction

Land surface models (LSMs) are common tools used to estimate current and future land surface states through physical relationships that exist within surface and subsurface systems. They can be used in standalone mode, forced with meteorological inputs, or they can be configured to function coupled to an atmospheric model. LSM development has occurred rapidly in the last two decades concurrent with the evolution of computing systems and storage. In particular, the ability for LSMs to predict surface snow depth and characteristics [Ek, 2003; Niu et al., 2011], to describe the evolution of vegetation in the annual cycle [Cramer et al., 2001], to account for advanced canopy-radiation interactions [Niu and Yang, 2004], to include agricultural practices [Pugh et al., 2015], and to include the influence of urban centers on temperature and surface fluxes [Kusaka and Kimura, 2004; Salamanca et al., 2011] has evolved rapidly. Yet throughout this evolution, one aspect of LSMs

has remained fairly constant: the representation of water movement in a vertical column [i.e., Mahrt and Ek, 1984], and the role of soil hydro-physical properties in that relationship [Chen and Dudhia, 2001].

Due to large land surface heterogeneity (at meter and sub-meter scales), LSMs are reliant on empirically derived parameters, many of which are poorly observed. In Noah-MP, for instance, there are more than 130 standard and hard-coded parameters [Cuntz et al., 2016]. The representation of soil processes alone introduces dozens of highly uncertain, empirically-derived parameters, and these soil parameters have some of the largest impacts on surface water and energy fluxes [Arsenault et al., 2018].

Soil processes are dependent on external soil texture classification databases, and these soil texture classes need to be linked to soil hydro-physical properties via pedotransfer functions (PTFs), of which, there are many [See van Looy et al., 2017, for a review]. PTFs are both used to derive the parameters that are used in LSMs, and they are included in the LSM structure itself. For example, Cosby et al. [1984] fit a power function to laboratory measurements of soil suction for each USDA soil texture class. Now, commonly in LSMs (including Noah-MP and CLM), both the fitting parameters and the power function are used as a part of the modified Richards Equation, to simulate water movement vertically in the soil column [Chen and Dudhia, 2001].

These soil hydro-physical parameters are derived in laboratory experiments, based on regional surveying campaigns then applied widely in space—assuming, for instance, that sand in one location is the same as sand everywhere. Following this

framework, there is uncertainty in the external soil texture classification databases, there is uncertainty in the PTFs, and there is uncertainty in the parameter definitions that are inserted into the PTFs.

In this study, we analyze the impact of these soil hydro-physical parameter definitions on land–atmosphere exchanges of heat and water. We utilize a modernized soil parameter table with updated hydro-physical properties [Kishné et al., 2017, ; hereafter K17], and compare it to the default soil property table in the WRF modeling suite. Section 2 will address the model design, discuss the role of soil hydro-physical properties in this modeling configuration, as well as describe each table and their origins. Section 3 will discuss the impacts of these parameters on seasonal model simulations. Our final thoughts, and conclusions will be presented in Section 4.

4.2 Experimental Design

4.2.1 Model design

This study utilizes the Weather Research and Forecasting model (WRF) version 4.1.2 [Skamarock et al., 2008] coupled to the Noah-MP land surface model [Niu et al., 2011] version 3.1 to evaluate the role of soil hydro-physical parameter definitions in land surface and coupled land-atmosphere processes. Two sets of experiments are conducted. The first utilizes the default soil parameter descriptions provided with the coupled WRF/Noah-MP modeling suite, and the second exchanges those parameters for the updated K17 parameters. For each variation, simulations are

conducted from January 1, 2020 through August 30, 2020. The initial 6 months are chosen for model spin-up, and they are considered sufficient to bring deep layer soil moisture into equilibrium. At the end of the spin-up period, the summer months (JJA) are considered for evaluation. Ensemble members are initiated on consecutive days from the end of the spin-up period: May 28, May 29, and May 30. Multiple days are used to account for dependence on model initial conditions. The early days are excepted, and only June 1 through August 30 are considered for analysis.

The model grid is set to 12-km horizontal resolution and is configured roughly over the CONUS region. There are 50 vertical levels, with the additional levels added to the lower atmosphere to better represent the boundary layer. The horizontal resolution mandates a convective parameterization: the Betts-Miller-Janjíc convective scheme is chosen [Janjić et al., 2001]. Thompson single-moment microphysics are implemented [Thompson et al., 2008] as well as, the RRTM-G radiation scheme [Iacono et al., 2008]. A second-order closure, non-local planetary boundary layer (PBL) scheme (MYNN2) is chosen to represent turbulent processes in the boundary layer [Nakanishi and Niino, 2006].

4.2.2 Use of soil parameters in Noah-MP

The LSM chosen for these simulations is the Noah-Multi-Physics [Noah-MP; Niu et al., 2011]. The Noah-MP LSM has been used and tested extensively serving as the lower boundary condition of NOAA's operational Global Forecast System (GFS) and the Climate Forecast System (CFS). It is the main LSM in NASA's

comprehensive land modeling framework: Land Information System [Kumar et al., 2011]. It has served as the primary land surface model through the development of the North American Land Data Assimilation System [NLDAS; Cosgrove et al., 2003], and other multi-institutional community-wide initiatives, and it very commonly used for research applications such as this. For a more robust description, please refer to Appendix C.

Noah-MP represents many processes within the land surface system in very fine detail. Compared to its predecessor, Noah, Noah-MP separated the canopy from the ground surface, which allows for more complex physical processes such as precipitation throughfall, sub-canopy turbulence, and canopy shading to be represented in a far more realistic way improving the surface energy balance. Similarly, in Noah-MP there are improved snow and frozen soil processes, and an unconfined aquifer serves as the lower boundary condition, which improves soil storage, recharge, runoff estimation [Niu et al., 2011].

The transport of water within the surface is controlled by a version of the Richards Equation:

$$\frac{\delta\theta}{\delta t} = \frac{\delta}{\delta z}\left[K\left(\frac{\delta\Psi}{\delta\theta}\right)\frac{\delta\theta}{\delta z}\right] + \frac{\delta K}{\delta z} + F_\theta, \tag{4.1}$$

where, θ is volumetric soil moisture, Ψ represents matric potential, K describes unsaturated hydraulic conductivity, z is depth (m), t is time (s), and F is a general source sink term that includes the effects of infiltration, percolation, and evaporative processes. Matric potential can be described by:

$$\Psi = \Psi_s \left(\frac{\theta}{\theta_s} \right)^{-b} \tag{4.2}$$

(i.e., Cosby et al. 1984). While, K follows the Campbell (1974) formulation:

$$K = K_s \left(\frac{\theta}{\theta_s} \right)^{2b+3}. \tag{4.3}$$

Volumetric soil moisture at saturation, or the porosity, is represented by θ_s. K_s and Ψ_s are the saturated hydraulic conductivity, and the saturated matric potential, respectively. b, in the definitions of K and Ψ, represents a curve-fitting parameter that displays a significant control over the both terms, but is heavily dependent on the samples from which it was derived. Because the Richards Equation in this form controls the transport of soil moisture, and it is strongly dependent soil hydro-physical parameters, the performance of Noah-MP is also dependent on soil hydro-physical parameters.

4.2.3 Soil hydro-physical parameters

The default soil hydro-physical parameters in the SOILPARM.tbl in Noah-MP are collected from multiple sources and have evolved over the last two decades to include additional categories (e.g., playa, lava, etc.), and some additional parameters (e.g., QTZ etc.) (See Kishné et al. [2017] for a detailed review; their Table 2). For this discussion, we will focus on four of the original parameters: BB (b), MAXSMC (porosity), SATPSI (saturated matric potential), and SATDK (saturated hydraulic conductivity), which were each defined in Cosby et al. [1984] for 11 out of 12 of the

original USDA soil categories (excluding silt).

Cosby et al. [1984, ; hereafter C84] used soil data from Holtan et al (1968) Holtan et al. [1968]. It includes 1448 soil samples acquired from 35 sites spread across 23 states and multiple major watersheds. The primary analysis included measuring soil water retention across multiple pressure heads. These parameters were the result of both measurement and fitting of a power function (given in Eq. 2). The mean values of each parameter from that analysis are used today in the SOILPARM.tbl. See Fig. 1 for the original values of each of these four parameters, and their standard deviations.

The soil hydro-physical parameters presented in K17 represent a more robust surveying campaign, utilizing 6749 soil samples from 850 profiles. While, C84 analyzed soil samples from localities distributed across the CONUS region, K17 parameters constitute a more high-resolution sampling strategy, with all 850 profiles located in and around Texas (See K17, their Fig. 1). The goal being to investigate the default table's relevance to soil and hydrological studies in the Texas region. It was not the goal of the K17 experiment to provide a widely applicable soil parameter table, so while it uses more samples, it is limited by the same regional limitations as the previous table in all areas outside of Texas and its surrounding states.

K17 parameters are also included in Fig. 1. For instance, Fig. 1a shows the porosity (θ_s) values for both K17 and the default parameter table. The differences in Fig. 1a are modest and less than the reported standard deviation, indicating the original reported standard deviation in C84 was sufficiently variant to describe this parameter. The same is true in Fig. 1b, except notice that the standard deviation

in most categories is twice the parameter value, suggesting both significant variation in the laboratory measurements, and overlapping parameter values in adjacent categories. The b parameter (Fig. 1c) is also highly variable (large standard deviations relative to value). In the case of the b parameter in sandy loam and clay loam, the differences between K17 and the default parameters are larger than the standard deviations, suggesting that the parameters in C84, were likely not representative of all conditions. Further, the differences in saturated matric potential (Ψ_s) (Fig 1d) for most soil categories are larger than the original reported standard deviation value, suggesting again an inadequate representation of the parameter variance.

Figure 2 shows matric potential (a) and unsaturated hydraulic conductivity (b) for select soil categories across a range of typical soil moisture values, following Eq 2, and Eq 3, respectively. If matric potential for sand is considered, the values are very similar at high soil moisture values, however as soil moisture decreases, the differences between K17 parameters and default increases. This behavior is the opposite in clay, with very similar values at low moisture, however with increasing differences with increasing soil moisture. This contrasting behavior indicates that soil moisture and the coupled system response will vary depending on both soil texture category and climatic regime (i.e., moisture-limited vs. energy-limited environments).

The differences in soil parameters are mapped on the model grid in Fig. 3, along with the soil texture classification map (Fig. 3a). Differences in saturated hydraulic conductivity (Fig. 3b) are fairly wide-spread along the U.S. East Coast, and throughout the Mountain West, with the largest negative differences seen in

Florida and western Nebraska, associated with the sand category. Large positive differences are also seen in the U.S. Southeast in Georgia, and Alabama, primarily associated with sandy loam, and minor negative differences are found throughout the Midwest associated with silt loam. Differences in saturated matric potential (Fig. 3c) are moderately positive throughout the Midwest (silt loam), and moderately negative in the west and throughout Mexico (loam). Differences in porosity (Fig. 3d) are mostly positive, with large positive values for the sand category in Florida and Nebraska, and moderately positive throughout the Midwest (i.e., silt loam). There are also minor negative values in porosity (Fig 3d), throughout the Texas region (clay loam), and along the Eastern Coast of the Gulf of California (sandy clay loam). The b parameter is shown in Fig. 3e. Strongly negative quantities occur throughout the U.S. Southeast, and throughout the Western States (mostly sandy loam), and weakly positive values elsewhere.

A change in parameters leading to an increase in matric potential would cause the soil to retain water more strongly, and the opposite is true for a change leading to a decrease in matric potential. A change in parameters leading to an increase in hydraulic conductivity would increase the amount of moisture transmitting through a volume of soil in a given time (i.e., increase sub-surface flow rate), and the opposite is also true for a change leading to a decrease in hydraulic conductivity. In general, these parameters are hydrologically consistent, meaning that for these parameters to change with opposite impacts would be rare. For instance, negative differences in b in the western states would lead to both a decrease in matric potential, and an increase in hydraulic conductivity leading to a scenario where the soil retains water

with less force and the flow rate has increased. As such, negative differences in b in the west would be expected to lead to a decrease in available moisture in the soil, and a reduction in latent heat flux. However, in arid regions like the west, extremely dry soil conditions often limit the impact of soil hydro-physical parameters because in both cases the soils are dry enough to continue to retain moisture very strongly, both still limiting ET in a similar way, despite differences in matric potential. While a change in b would affect both matric potential and hydraulic conductivity, a change in saturated hydraulic conductivity (K_s) or saturated matric potential (Ψ_s) would affect only hydraulic conductivity or matric potential, respectively.

Regional parameter differences such as those associated with the larger continuous area of silt loam will allow the differences in parameter values to project themselves onto regional scales. Features like those associated with silt loam in Midwest will emphasize parameter differences, as opposed to other cases with a more discontinuous representation. We expect that while there still may be differences associated with local areas of relatively large parameter differences, the regional climate and general circulation will respond more strongly to larger coherent areas of reduced or increased parameter values.

4.3 Parameter Impacts and Validation

We will examine next the response of the model simulations to changes in soil hydro-physical parameters by calculating differences in the ensemble mean for certain variables relevant to land surface processes and land–atmosphere coupling,

and comparing those fields to observations. This approach will generally follow the land–atmosphere coupling processes chain, excluding the impact of entrainment from the free-troposphere and cloud cover [Santanello et al., 2009]. It will consider soil moisture, surface fluxes, and the response of 2-m temperature and precipitation. To estimate model performance, a general performance metric is used for land-only points. Mean absolute error (MAE) is used, given by:

$$MAE = \frac{1}{n}\sum_{n=1}^{n} |y_i - x_i| \tag{4.4}$$

Where n is the number of land-only points, x represents the observed value, and y represents the predicted value. This quantity is averaged in time across the 3-month period (JJA 2020), and it will give us an indication whether improved performance was achieved by updating the soil hydro-physical parameters or not.

4.3.1 Soil moisture

First, it is necessary to analyze differences in volumetric soil moisture. The soil hydro-physical parameters dictate the movement of water at the surface and below, so it is expected that changing the hydro-physical parameters will lead to differences in volumetric soil moisture. For model validation, Soil Moisture Active-Passive (SMAP) Level 4 Rootzone soil moisture is used [Reichle et al., 2019]. The SMAP Level 4 dataset at 9-km horizontal resolution is derived from the raw SMAP satellite data which is surface based (5 cm in depth), and is propagated downwards using the Catchment Model. This constitutes a reliable estimate and land surface states,

and is used in this procedure as the "truth" despite its own possible minor biases. It is bi-linearly interpolated to the model grid so spatial biases can be calculated, and rootzone soil moisture is considered (0–100 cm depth).

Figure 4 shows (a) SMAP soil moisture and compares it with ensemble mean soil moisture from both (b) the set of WRF simulations utilizing K17 (hereafter, WRF_{K17}) and (d) the set of WRF simulations using the default settings (hereafter, $\mathrm{WRF}_{default}$). The mean fields show a decrease in average soil moisture from west-to-east, with the largest values in the Midwest United States, and within the eastern Mississippi River Watershed. Values in the SMAP L4 data are more extreme than the simulated soil moisture: drier in the dry areas, and wetter in the wet areas. Some similar features are apparent, such as the relative dryness in Florida, and the relative dry region in western Nebraska. In general, the patterns of rootzone soil moisture are very similar. Calculating the model biases, reveals the patterns discussed. Relative dry areas in the east, denoted by negative differences, and relative wet areas in the west denoted by positive differences. The MAE for each simulation is similar with only a slight, but perhaps negligible improvement for the K17 simulation. Total soil moisture and differences between simulated soil moisture and the observed soil moisture are related to many processes connected to the land surface and the coupled land-atmosphere system, making it difficult to infer which parameters lead to these differences; however, evaluating the differences between the model simulations is more useful for this purpose.

Figure 5 shows the differences in the ensemble mean soil moisture with each soil layer. Layer 1 (a) (0–10 cm depth) shows positive differences in the west (i.e., area

where K17 is retaining more moisture), negative values in the Midwest. Notice how the second (Fig. 5b) and third (Fig. 5c) layer are almost the opposite sign. The top and bottom soil layers are more difficult to interpret because, not only are soil hydrophysical properties working to alter soil moisture, but also there is input/removal of moisture from the top layer directly from atmospheric processes, and there is input/removal to the deepest layer from aquifer/groundwater interactions.

The middle two layers show very similar patterns to each other, which mainly follow the patterns in b. Negative differences in b (i.e., the Western U.S. in Fig. 3e), will cause the soil to retain moisture less strongly following matric potential (Eq. 2), and unsaturated conductivity is impacted: the rate of drainage will increase leading to negative differences in soil moisture in the west. This mechanism is enhanced by the mostly positive differences in saturated hydraulic conductivity (Fig. 3b), and the mostly negative differences in saturated matric potential (Fig. 3c), both supporting the increased conductivity, and reduced retention, respectively.

There are positive differences in soil moisture in the upper Midwest in the middle two soil layers, the opposite of what was seen in the West. Reversing the mechanism from above, this area has positive differences in b (i.e., leads to increased retention and reduced conductivity) and saturated matric potential (i.e., increased retention), while the differences in saturated hydraulic conductivity are negative (i.e., reduced flow), (Figs 3e, c, b, respectively). Also note the there is a positive difference in porosity. Increasing porosity reduces drainage, and increases moisture retention, though lesser so than the other more impactful parameters. Each of these together leads to positive soil moisture differences at mid-levels in the Midwest.

4.3.2 Surface fluxes

The differences in soil moisture are expected to lead to differences in the partitioning of water and energy fluxes at the surface. Ensemble mean latent heat flux in the $\mathrm{WRF}_{default}$ simulation (Fig. 6a) shows near-zero values occupying much of the Western states, and increasing towards the East, with values reaching their maximum (about 150 W m^{-2}) along the Appalachian Mountains. Differences in mean latent heat flux (Fig. 6b) show an area of largely negative values in the Midwest region, in the same area as the negative differences in the top-layer soil moisture. It appears that the latent heat flux is responding to the top-layer soil moisture instead of responding to the deeper rootzone layers. The ensembles utilize the same vegetation assignment, so even though soil properties influence vegetation at the soil-root interface, the differences in transpiration could be low. In fact, given the magnitude of the differences, these could be primarily related to the bare soil evaporation, which can occur in the non-vegetated fraction of each grid space. These differences in latent heat flux from the top soil layer are due to the negative differences in soil moisture shown in Fig. 4a.

Notice the area of strongly positive differences in Nebraska, in a region that we earlier noted as sand (See discussion of Fig 3). Compare that sand region to the region classified as sand in Central Florida. Despite the same changes in soil hydro-physical properties for this texture category, and similar values in soil moisture, there are strong differences in latent heat flux in Nebraska, which do not occur in Florida. This is because the impact of soil hydro-physical properties on

surface fluxes is sensitive the climate regime. Soil properties are less important in water-limited environments, because regardless of soil texture category, the matric potential retains moisture so strongly for all categories that it is unlikely to be removed through ET. Similarly, in energy-limited environments soil moisture moves rather free of constraint from matric potential, and drainage is only limited by K. It is in the middle-range of possible soil moisture values that the soil properties have a larger impact on surface fluxes, and soil moisture movement.

The response in sensible heat flux to the differing soil hydro-physical properties (Fig. 6d) is similar but opposite sign to the response of latent heat flux. There is a strongly positive area in the Midwest, with near zero values in most other regions. Energy that impinged on the land surface was distributed, and the energy that did not evaporate moisture went into sensible heat flux; therefore, we expect negative differences in latent heat flux and positive differences in sensible heat flux to be collocated following the surface energy balance.

4.3.3 2-m Temperature

In the next stage of the land surface-atmosphere coupling process chain, it is expected that increased matric potential will affect surface fluxes (i.e., reduced ET, increased sensible heat flux) leading to differences in low-level thermodynamic variables (i.e., increased 2-m temperature and reduced 2-m specific humidity), while regions with decreased matric potential would do the opposite. The same thinking can be applied to hydraulic conductivity.

The ensemble mean 2-m specific humidity shows a gradient of increasing values across the CONUS region, from west-to-east, with the highest values along the eastern and southern coast of the U.S. and the eastern coast of Mexico (Fig. 7a). Differences in ensemble mean specific humidity closely match differences in ensemble mean latent heat flux (Fig. 6b) with negative moisture values in the Midwest collocated with negative latent heat fluxes driven by soil hydro-physical properties, and slightly positive values along the southern east coast of the U.S. and over the region in western Nebraska, both collocated with positive differences in latent heat flux and classified as sand. A similar picture can be illustrated for 2-m temperature. Positive differences in 2-m temperature exist in the Midwest region collocated with positive differences in sensible heat flux, along with the corresponding negative differences along the southern east coast of U.S. and in Nebraska. These differences in 2-m thermodynamic variables closely match the differences in surface latent and sensible heat fluxes, which were induced by soil hydro-physical parameters.

To see if the differences in Fig. 7 translate to differences in model performance, simulated 2-m air temperature is compared to the Global historical Climate Network–Climate Anomaly Monitoring System [GHCN-CAMS Fan and van den Dool, 2008]. The GHCN-CAMS data are interpolated from their original 0.5° resolution grid to the 12-km grid using a bi-linear approach. These data have not undergone any correction for topography, nor for bias resulting from the interpolation. While it is understood that topography will influence the temperature by simple thermodynamic relationships, our discussion will focus on areas away from extreme topographical features (e.g., the Rocky Mountains) and will instead focus on the

U.S. Great Plains region.

The GHCN-CAMS 2-m temperature shows a general increase in temperature from north to south, with maximum values in the desert Southwest, and along the coast of western Mexico (Fig 8a). Both ensemble mean temperatures reveal a slightly different pattern with an extension of the southern coast U.S. temperatures into the high plains of the Central U.S. (Fig. 8b and d). If the bias is considered for each ensemble there is a prominent warm anomaly in the northern U.S. Great Plains (Fig. 8c and 8e). This is not an uncommon feature in both seasonal and longer-term simulations during summer in the Great Plains (i.e., Dennis and Berbery, 2021; Klein et al 2006). In general, both ensemble mean 2-m temperatures are similar in their representation of the observed seasonal mean. The MAE for each ensemble supports this assertion with a difference of only 0.04.

Temperature at 2-m can also be compared to station observations (Fig. 9). Each station in Fig. 9, represents an Automated Surface Observing Station (ASOS) site at a regional airport in Texas. Texas was chosen because it is the location of soil samples used to derive the K17 soil hydro-physical parameter dataset. It is expected that in this location, there should be an improvement in land surface representation, which should theoretically translate to improved temperature representation. These data were collected from the Integrated Surface Database [ISD; Smith et al., 2011]. This remarkable database represents a vast collection (more than 35,000 stations) of global hourly and synoptic observations from numerous sources including the ASOS program, with some stations having over 100 years of activity.

The simulated ensemble mean diurnal temperature evolution closely follows

the observed diurnal evolution of 2-m temperature at each ISD station (Fig. 9). In Abilene (Fig. 9a), both ensemble mean temperatures are slightly warmer throughout the diurnal cycle than observations however, this bias is less than 2° C, with a very modest improvement from $\mathrm{WRF}_{default}$. This is a similar situation in the other locations, with the exception of San Antonio, which has a notable cool bias for both ensemble mean diurnal cycles overnight and into the early afternoon. Furthermore, this is another instance of differences in the ensemble means, but neither resulting in a substantial improvement in the general model performance.

4.3.4 Precipitation

Differences in surface fluxes caused by soil hydro-physical properties led to differences in low-level thermodynamic variables. The land surface-atmosphere coupling process chain culminates with the precipitation responding to the thermodynamic evolution of the PBL. Following this approach, precipitation is analyzed to see if changing soil hydro-physical properties, which altered soil moisture and surface fluxes, will lead to differences/improvements in precipitation representation.

Simulated ensemble mean precipitation is compared CPC Global Unified gauge-based precipitation dataset [Chen et al., 2008; Xie et al., 2007]. The CPC Global Unified Precipitation data was provided by the NOAA/OAR/ESRL PSL, Boulder Colorado, USA, from their web site https://psl.noaa.gov/data/gridded/data.cpc.globalprecip.html. Similar to GHCN-CAMS, the CPC data is originally 0.5° resolution, and is bi-linearly interpolated to the model grid without correction.

CPC Unified Precipitation shows a dearth of precipitation in the arid western states, with precipitation increasing towards the eastern U.S. coasts (Fig. 10a). The highest values of observed precipitation are greater than 4.5 [mm day^{-1}], which occur along the eastern and southern U.S. coasts, and in Mexico along the west coast in the North American Monsoon region. The ensemble mean precipitation is lesser than observations in most areas in the eastern U.S. with most rain in the U.S. falling along areas of topography, instead of through the Midwest and along the coasts (Figs. 10b and 10d). The ensemble mean bias tells a similar story (Figs. 10c and 10e) , with large negative differences in the eastern U.S. Both of the ensemble mean precipitation representations are very similar, supported quantitatively by the small differences in MAE. Differences between the ensemble mean precipitation are apparent (not shown) but are less than shown in previous studies (i.e., Dennis and Berbery, 2021) with maximum differences of about 0.4 [mm day^{-1}]. The differences are collocated with the more substantial surface flux differences (i.e., mostly east of the Rocky Mountains).

4.4 Final Thoughts

This study utilized the coupled WRF-Noah-MP modeling suite to conduct two seasonal simulations using an ensemble approach to compare the use of two soil hydrophysical parameter datasets. The default soil parameter dataset is associated with many LSMs that use a look-up table, including Noah-MP and CLM. The other soil parameter dataset, that of K17, was derived as an alternative to the default, but

mainly for use in Texas and the surrounding region. Even though K17 is not meant for continental simulations such as these, it offered a set of hydrologically-consistent, plausible soil parameters, which enabled this more general study looking at the implications of changing soil hydro-physical parameter values on land surface states, and land-atmosphere coupling. Changing soil hydro-physical parameters does not improve the shortcomings associated with a look-up table. Both of these parameter sets are still not regionally transferable, and soil texture categories are not fine enough to be representative of soil texture heterogeneity and behavior.

This study focused on four variables in particular: porosity (θ_s), saturated matric potential (Ψ_s), saturated hydraulic conductivity (K_s), and b. From these parameters and volumetric soil moisture, one can calculate both matric potential following C84 (Eq. 2), and unsaturated hydraulic conductivity following Campbell (1974) (Eq. 3); two values which are critical to representing soil moisture movement below the surface. In some cases, differences in both the b parameter and saturated matric potential were greater than the original reported standard deviation of those parameters, suggesting larger variability in soil samples.

Differences in these hydro-physical parameters translated to differences in soil moisture. In some areas (like the western states), conductivity was increased, and matric potential was mostly decreased, creating a situation where the soil would transmit water quicker, and retain moisture less strongly; however due to the general aridity of the landscape, few differences were seen associated with soil hydro-physical properties. In other cases, like in the Midwest, matric potential was increased, so the soil retained moisture more strongly leading to positive differences in soil moisture

at level two and three, but negative differences in the top soil, which responds more quickly to coupled land-atmosphere effects. In either case, the response of the soil moisture to the differences in hydro-physical properties varied by region and climate regime. Soil parameter-related differences in soil moisture led to differences in surface sensible and latent heat fluxes, which were again sensitive to both region and climate regime. The primary flux differences were located in the Eastern U.S., in a less arid climate, with strong negative differences in the Midwest associated with decreased top-layer soil moisture. Strong negative differences in latent heat flux were collocated with strong positive differences in sensible heat flux obeying the surface energy balance.

Following the land surface atmosphere coupling process chain, differences in soil moisture and surface fluxes led to physically consistent differences in low-level thermodynamic variables. While these thermodynamic variables differed, when compared to observations those differences meant little when it came to quantifiable improvement in model performance. The same story is true connecting ensemble mean precipitation to the boundary thermodynamic structure—while differences are apparent in the ensemble mean values, those differences did not yield substantial improvements in performance.

In conclusion, this study analyzed the impact of changing soil hydro-physical properties on land surface states, and land-atmosphere coupling. It was found that land surface states and land-atmosphere coupling are sensitive to soil hydro-physical parameters, but that sensitivity is dependent on climate regime and region. The variations in soil hydro-physical parameter values are highlighted in this work. Lab-

oratory measurements of soil samples from differences regions often vary over orders of magnitude. Yet, those measurements are applied widely when using LSMs. This work is novel because it illustrates that differences in soil hydro-physical parameter values can have significant effects on land-atmosphere coupling and regional climate. These results improve our understanding of soil processes and the role of soil processes in coupled modeling. The understanding gained through these experiments will inform the next generation of land surface model development.

4.5 Final Summary of Physical Relationships

In this chapter, we investigated model uncertainties related to the definitions of soil hydro-physical parameters. While the previous two chapters explored the role of soil texture, this chapter examined the suitability of the soil parameters in the look-up table. Like the locations of soil texture classes, soil hydro-physical parameters are highly variable across small spatial scales making them difficult to define, yet in LSMs, a single parameter is often applied to an entire grid space resulting in misrepresentations of soil hydrologic processes. To this end we employed an alternative set of hydrologically-consistent soil parameters to replace the commonly-used default soil parameter table in Noah-MP. Coupled seasonal WRF-Noah-MP simulations using either dataset revealed important differences in ensemble mean soil moisture, surface latent and sensible heat fluxes, and the near surface atmospheric temperature and moisture related to the definitions of soil hydro-physical properties. For this discussion of physical relationships, I will focus on the soil property differences

associated with silt loam, the dominant soil category in the Midwest.

The key soil hydro-physical parameter differences associated with silt loam are the following: an increase in saturated matric potential and b. Collectively, these differences suggest that in the simulation with the new parameters, grid spaces with silt loam will retain moisture more strongly (increased matric potential; + saturated matric potential and +b).

The analysis of soil moisture reveals that there are near zero and slightly negative ensemble mean differences in top layer soil moisture in the area defined as silt loam, with near zero and slightly positive differences in the middle two soil layers down to 1 m depth beneath the surface (See Fig. 4a–c). Soil moisture differences of this magnitude are quite small, offering a unique opportunity to analyze the impact of soil parameters like matric potential without trying to account for its exponential relationship with soil moisture. Because both soil moisture and soil properties control surface fluxes, having small differences in soil moisture allows for more emphasis to be placed on soil properties. Matric potential will be larger (i.e., more negative) for the simulation with the new parameters at a given value of soil moisture (i.e., due to the positive differences in saturated matric potential and positive differences in b), meaning that the soil will retain moisture more strongly. This is true for the top layer, which is susceptible to bare soil evaporation, as well as the middle two layers down to 1m depth, which constitute the active rootzone.

Increasing the magnitude of matric potential causes an increase in the energy needed to overcome the adsorptive properties of the soil grains, therefore, it is expected that for a given value of soil moisture, there will be a decrease in evaporation

and transpiration. Calculating the ensemble mean latent heat flux differences supports this assertion, showing negative differences in the region defined as silt loam, consistent with the increase in matric potential (as shown in Fig. 5b). Energy gained at the surface will cause moisture to evaporate either through direct surface evaporation from the soil or by initiating transpiration processes in vegetation. In either case, (at either the air-soil interface, or the root-soil interface), there is an exchange of moisture based on retentive properties. For example, as air dries, evaporative demand increases, encouraging evaporation from the soil; however, as soil dries, matric potential becomes more negative, causing soil to retain the remaining moisture more strongly. This balance of forces determines whether or not evaporation occurs. Likewise, at the root-soil interface there are physiological properties of the plants that allow the root system to absorb water, however there is a similar balance between the soil suction and the root suction. As moisture in the soil is taken up by root systems, eventually the soil matric potential becomes more negative to a point that the roots will fail to absorb water. At that point, the plant will start to wilt, hence this value of soil moisture is called the "wilting point". These are the processes occurring at and beneath the surface leading to the differences in latent heat flux in the ensemble mean. As matric potential increases (i.e., becomes more negative) as it does for silt loam with the new parameters, both evaporation and transpiration will decrease leading to the patterns seen in latent heat flux.

Incoming energy that can no longer remove moisture from the surface (i.e., due to the effects of matric potential) is partitioned into sensible heat flux. Therefore, in the region with silt loam there are negative differences in ensemble mean latent

heat flux, and positive differences in ensemble mean sensible heat flux in accordance with the surface energy balance (see Fig 4d).

In a similar manner to the discussion of soil texture effects on the previous chapters, those differences in surface fluxes then influence the low-level thermodynamic variables. In the same region as the decrease in latent heat flux, there is a decrease in mean two-meter mixing ratio. Likewise, the increase in sensible heat flux led to an associated increase in two-meter temperature in the ensemble mean differences. Once low-level thermodynamic quantities are altered, boundary layer processes are initiated leading to differences in surface-based atmospheric stability, boundary clouds, and even precipitation.

Soil hydro-physical properties and soil moisture are what dictate surface evaporation and transpiration. In cases like that of silt loam, when the values of soil moisture are similar between simulations, but the soil parameters are different, the analysis of different behavior can focus solely on the soil parameters. However, this is not always the case. Often times matric potential needs to be considered with both the soil properties and the soil moisture in mind, leading to complex relationships in soil moisture movement, distribution and the resulting fluxes. Furthermore, the responses of this coupled system to changing soil hydro-physical properties from one dataset to another is specific to both region and climate. These results have shown that uncertainty in the definitions of soil hydro-physical properties can affect the distribution of latent and sensible heat fluxes through surface processes, and that those fluxes will influence low-level atmospheric thermodynamics; therefore, leading to differences in land-atmosphere coupling.

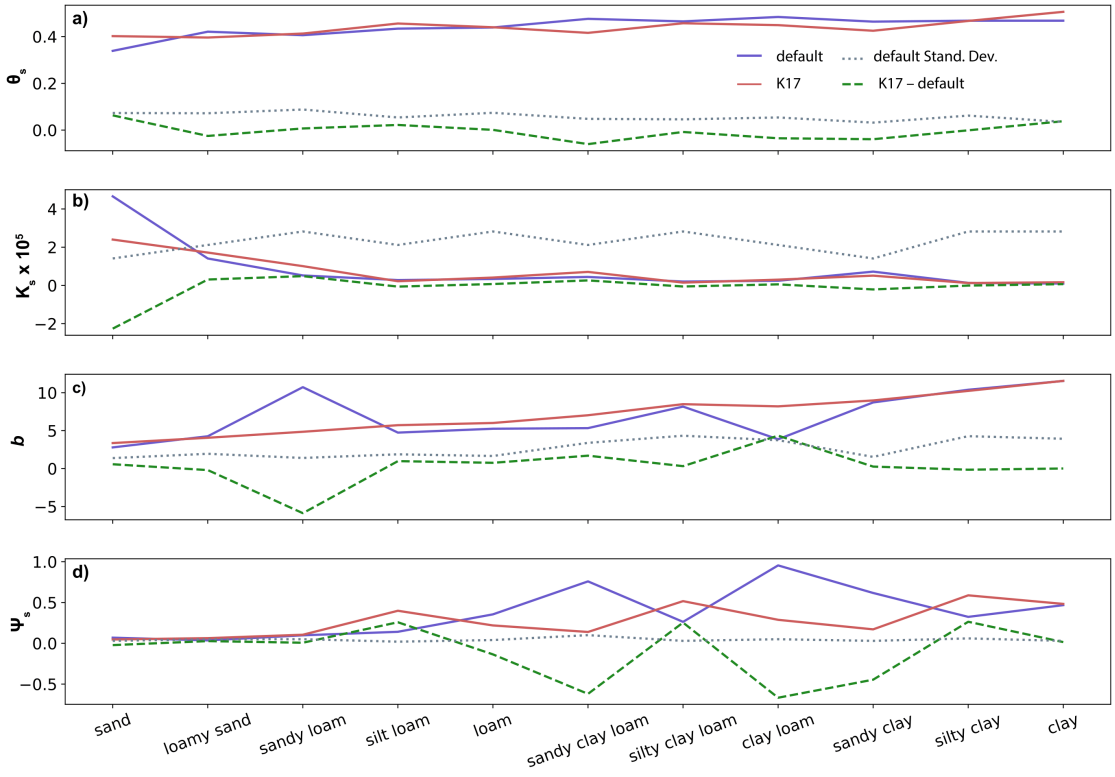

Figure 4.1: Select soil hydro-physical properties are shown for 11 of the 12 USDA soil categories (excluded silt). The default table values are shown (blue lines), as well as the K17 values (red line) for comparison. The differences between the two tables' values is shown using green dashed lines, and the standard deviation for each category as reported in Cosby et al. [1984], is shown as grey dotted lines. The hydro-physical properties are as follows: (a) θ_s,(b) $K_s \times 10^5$, (c) b, and (d) Ψ_s.

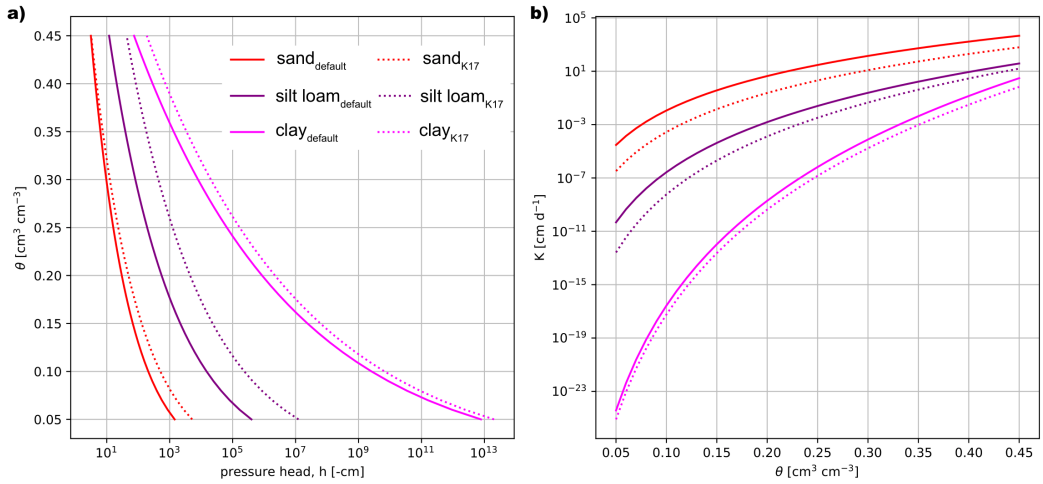

Figure 4.2: Following Eqs. 2 and 3, soil matric potential (-cm) (a; Eq. 2), and hydraulic conductivity (cm d^{-1}) (b; Eq. 3) are shown as a function of volumetric soil moisture (cm^3 cm^{-3}) for three soil categories: sand (red), silt loam (purple) and clay (pink). The default parameters are used in the solid lines, and the K17 parameters are used for the dotted lines.

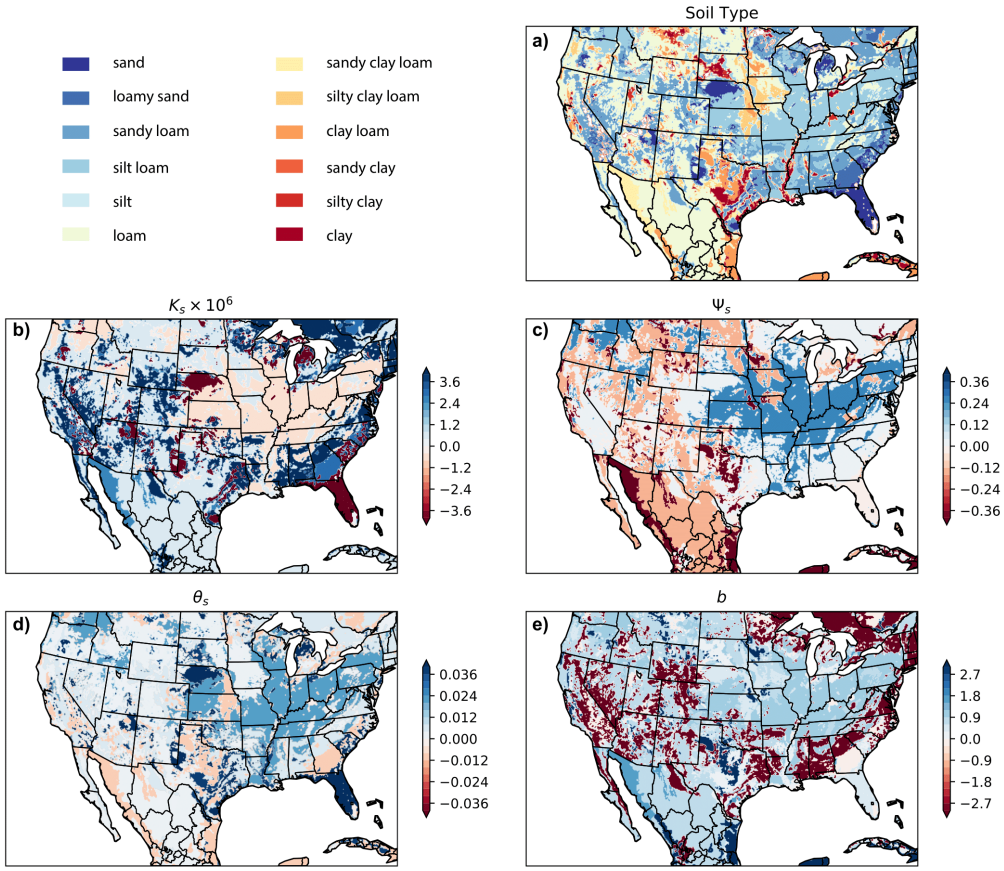

Figure 4.3: Soil texture categories are shown (a) on the model grid following the legend (top left panel), along with differences (K17–Default) in selected soil hydrophysical properties (b–e) following the soil texture categories (a): (b) $K_s \times 10^6$, (c) Ψ_s, (d) θ_s, and (e) b.

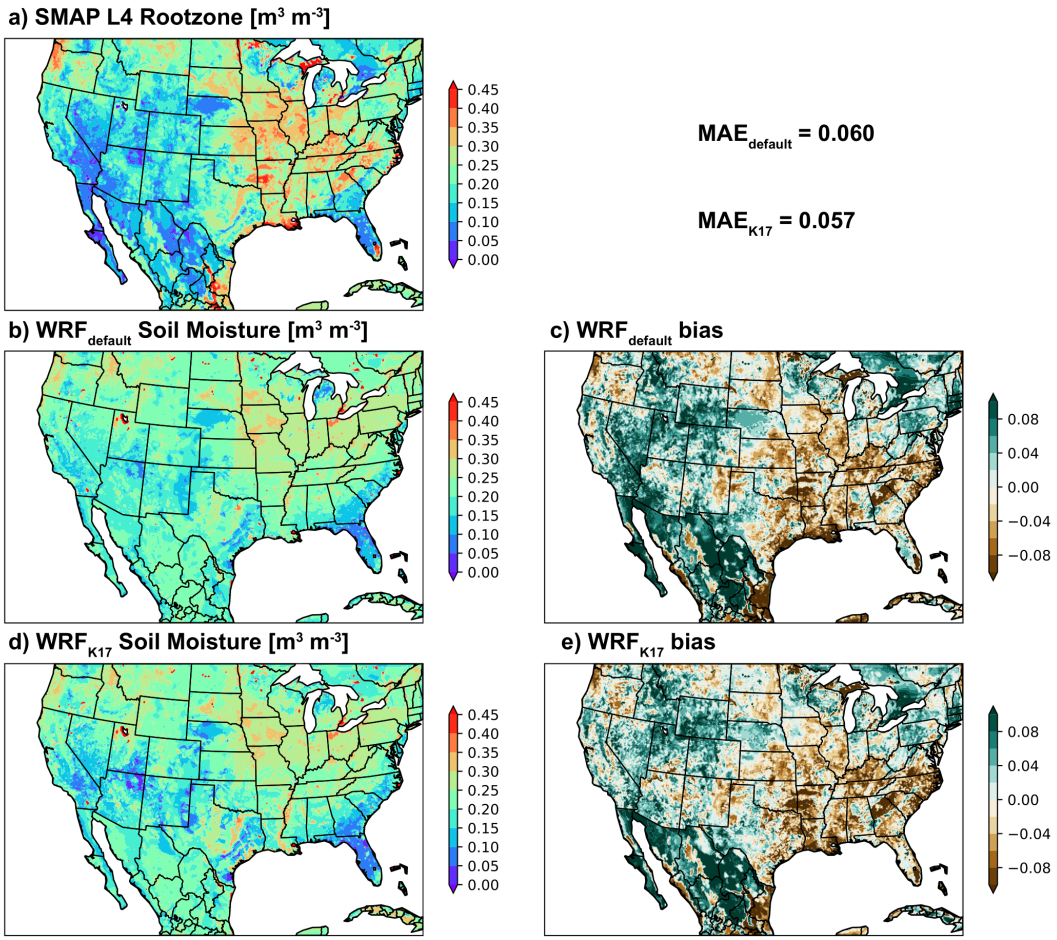

Figure 4.4: Volumetric soil moisture is shown from (a) the SMAP L4 Rootzone product [0-100cm depth; m^3 m^{-3}], along with (b) the $WRF_{default}$ ensemble mean volumetric soil moisture [0-100cm depth; m^3 m^{-3}], and (d) the WRF_{K17} ensemble mean volumetric soil moisture [0-100cm depth; m^3 m^{-3}]. The bias is shown ($WRF_{default}$ – SMAP) for (c) the $WRF_{default}$ simulation, and for (e) the WRF_{K17} simulation. The MAE for each simulation is shown in the top right panel.

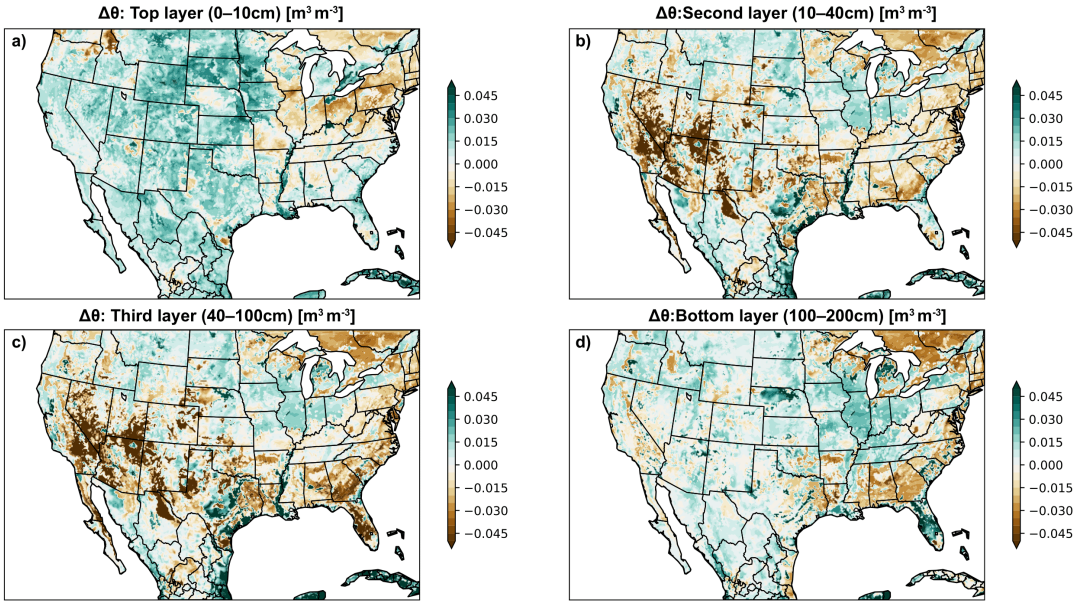

Figure 4.5: Differences (WRF_{K17} – $\mathrm{WRF}_{default}$) in mean volumetric soil moisture are shown at each soil level: (a) Level 1 (0–10 cm), (b) Level 2 (10–40 cm), (c) Level 3 (40–100cm), and (d) Level 4 (100–200 cm). All units are $\mathrm{m}^3\ \mathrm{m}^{-3}$.

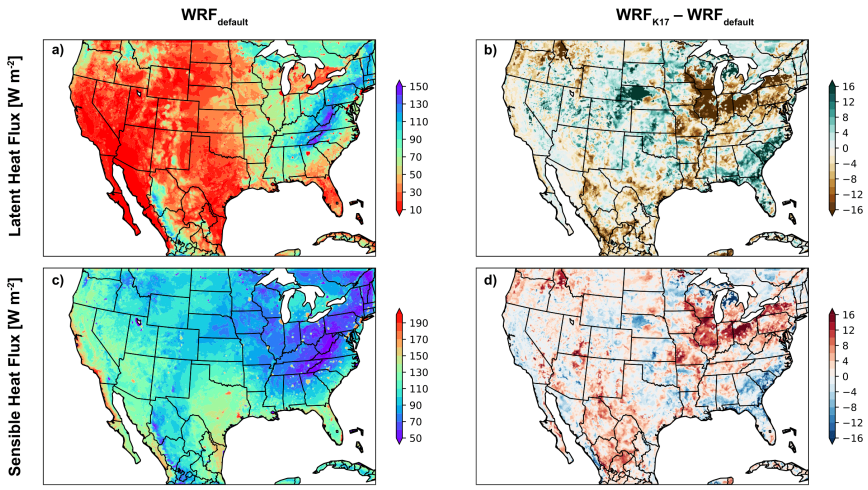

Figure 4.6: Ensemble mean (JJA, 2020) surface fluxes (W m^{-2}) are shown: (a) mean latent heat flux (W m^{-2}) for the WRF$_{default}$ simulations, (c) mean sensible heat flux (W m^{-2}) for the WRF$_{default}$ simulation. Differences (WRF$_K$–WRF$_{default}$) in (b) mean latent heat flux (W m^{-2}), and in (d) mean sensible heat flux (W m^{-2}) are also shown.

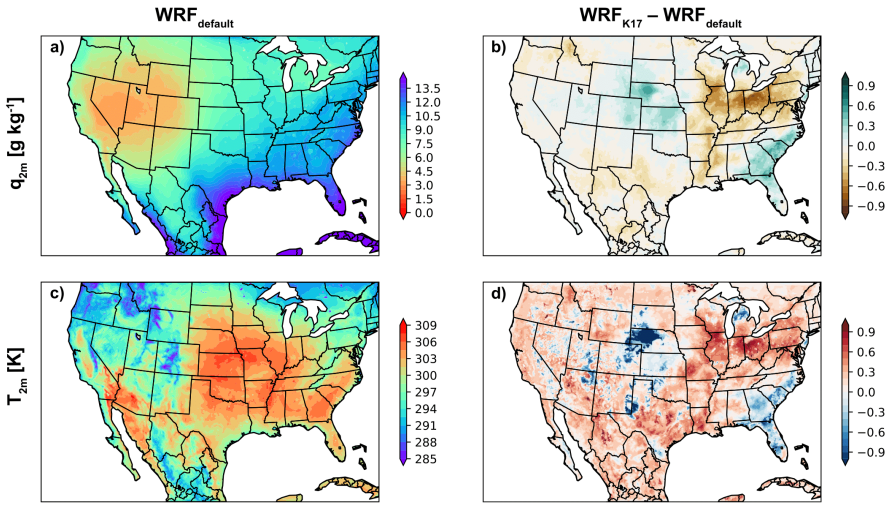

Figure 4.7: Ensemble mean (JJA, 2020) low-level thermodynamic variables are shown: (a) mean 2-m specific humidity (g kg^{-1}) for the WRF$_{default}$ simulations, (c) 2-m temperature (K) for the WRF$_{default}$ simulation. Differences ($WRF_K - WRF_{default}$) in (b) mean 2-m specific humidity (g kg^{-1}), and in (d) mean 2-m temperature (K) are also shown.

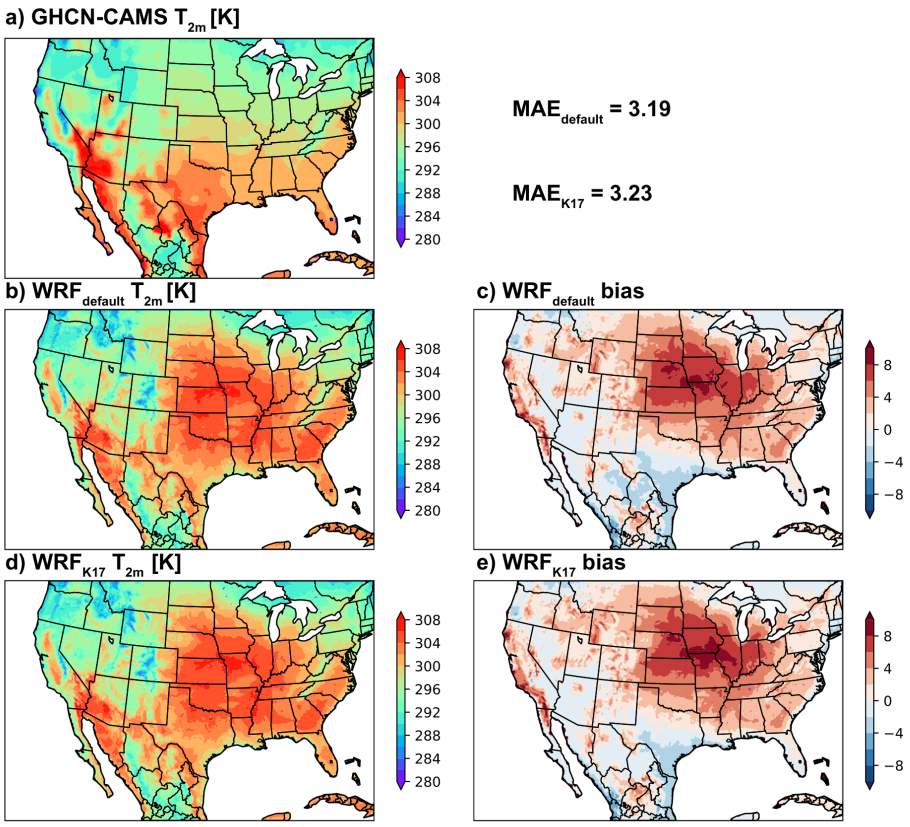

Figure 4.8: Temperature at 2-m is shown from (a) the GHCN-CAMS product [K], along with (b) the WRF$_{default}$ ensemble mean 2-m temperature [K], and (d) the WRF$_{K17}$ ensemble mean 2-m temperature [K]. The bias is shown (WRF$_{default}$ – GHCN-CAMS) for (c) the WRF$_{default}$ simulation, and for (e) the WRF$_{K17}$ simulation. The MAE for each simulation is shown in the top right panel.

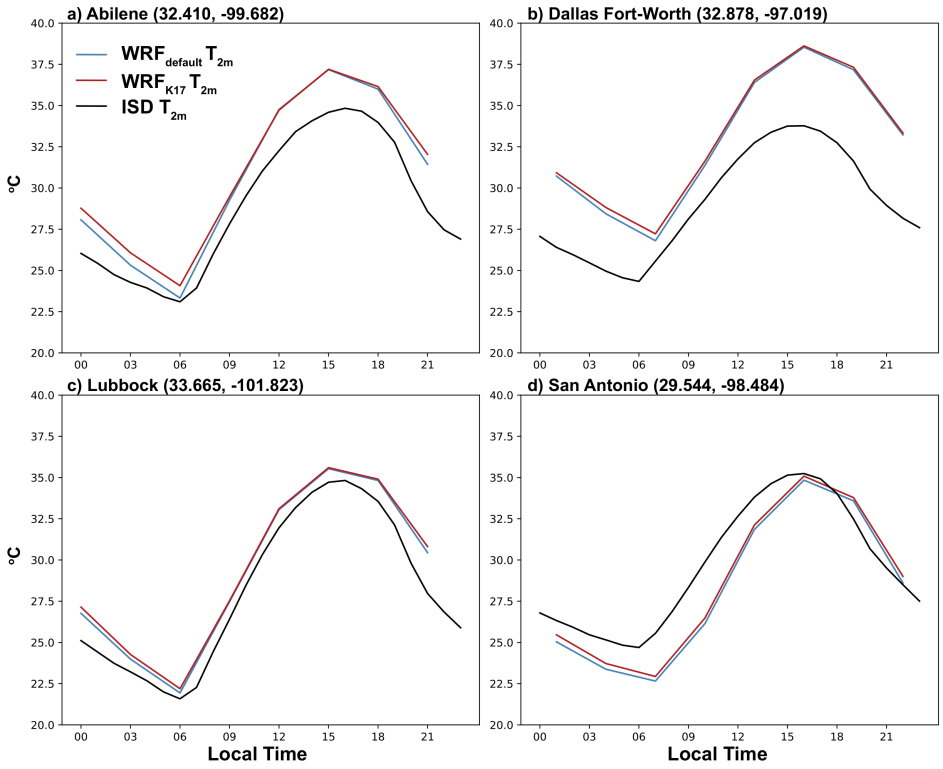

Figure 4.9: The diurnal cycle of temperature at 2-m [^{o}C] from station observations in Texas from the Integrated Surface Database are shown in black lines: (a) Abilene Regional Airport (32.410, -99.682), (b) Dallas Fort-Worth International Airport (32.878, -97.019), (c) Lubbock International Airport (33.665, -101.823), and (d) San Antonio International Airport (29.544, -98.484). The WRF$_{default}$ ensemble mean 2-m temperature is shown (blue lines), and the WRF$_{K17}$ ensemble mean 2-m temperature is shown (red lines). The X-axes in each panel shown local time.

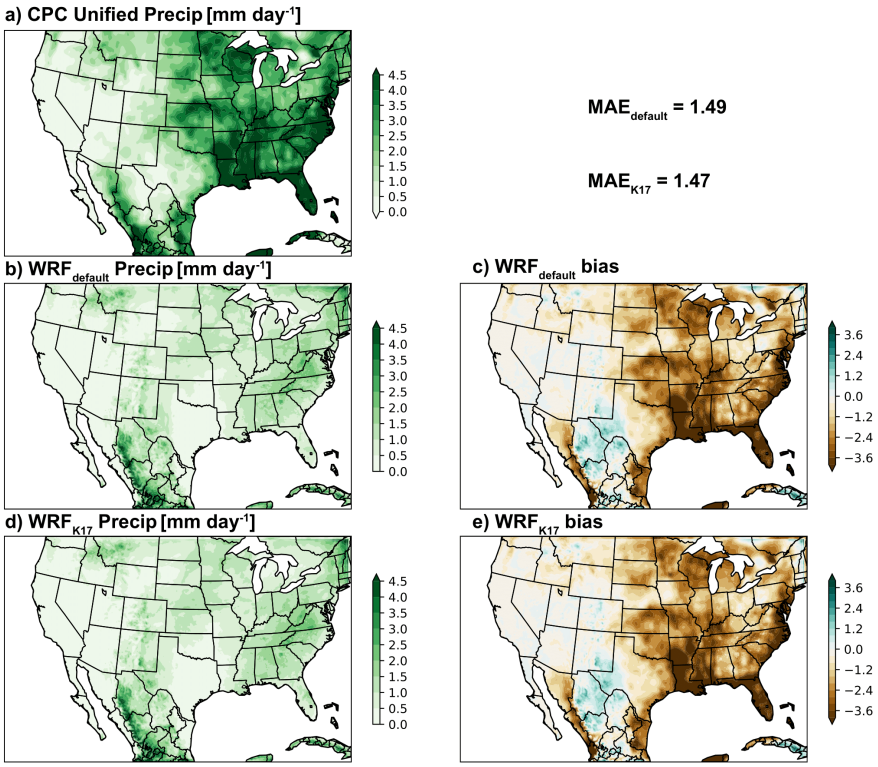

Figure 4.10: Precipitation is shown from (a) the CPC Global Unified gauge-based precipitation product [mm day^{-1}], along with (b) the WRF$_{default}$ ensemble mean precipitation [mm day^{-1}], and (d) the WRF$_{K17}$ ensemble mean precipitation [mm day^{-1}]. The bias is shown (WRF$_{default}$ – CPC Precip) for (c) the WRF$_{default}$ simulation, and for (e) the WRF$_{K17}$ simulation. The MAE for each simulation is shown in the top right panel.

Chapter 5: Final Thoughts

5.1 Summary and Challenges

This series of investigations has described the impacts of soil hydro-physical properties, represented in common LSMs, on coupled, seasonal WRF simulations over the North American region. The individual experiments have tested both the model sensitivity to rearranging the location of soil texture categories and the model response to changing the soil hydro-physical parameter values themselves. However, in both cases, neither configuration outperformed the other. While this collection of projects represents an early step towards quantifying and improving our understanding of the role of soil hydro-physical properties in couple land-atmosphere relationships, there are some obvious limitations in our ability to isolate the forcings of interest, including the role of vegetation, the limited-area modeling framework, and the coupled system response.

Throughout these experiments, a common consideration is the role of vegetation in these soil–land-atmosphere relationships. In reality, if the soil characteristics are changed, then the vegetation would physiologically respond. For example, if sand was transformed into clay, root systems with stronger absorptive properties would thrive instead of roots systems with weaker absorptive properties. Over long

time periods, the plants with root systems that could not readily absorb moisture from clay would not be able to transpire, leading to decay and replacement by plants that were better suited. This process does not occur in land surface models. Instead, the vegetation systems and the soil systems are unaware of each other. Parameters from each system are used in the equations to define evapotranspiration processes, but the systems themselves do not respond to each other. Vegetation is characterized much like the soil processes are defined. An external database often based on satellite remote sensing (i.e., MODIS) defines the general vegetation type for each grid space in the pre-processing system. Then those grid space indices are attached to a look-up table of vegetation parameters (e.g., rooting depth, LAI, stomatal resistance, etc.). When parameterizations in each grid space are activated, the model uses the vegetation index to find the correct parameter for each vegetation category and applies it accordingly. In this way, vegetation parameters and soil parameters are often used in unison, however, the two sets of parameters cannot evolve to synchronize with one another. This is the case with all current land surface models. The situation created by this structure is one where possible physical responses do not constrain soil-vegetation interactions but rather can occur in unrealistic scenarios (i.e., plants existing in soil conditions that are not likely or even possible). It would be a great improvement if the vegetation and soil systems would interact more realistically, but that type of LSM is still being developed.

Additionally, each of these experiments utilizes a limited-area model to perform simulations. In limited-area modeling, simulation quality can be limited by a lack of uncertainty quantification in the boundary conditions. The scales of at-

mospheric motions are restricted to those that fit within the boundary. In some cases, it has been found that precipitation processes in summer have been better represented in smaller regional domains, but that SM-P sensitivity is better represented in a larger domains [Seth and Giorgi, 1998]. In preparing these simulations, the goal was to separate the model boundaries from the areas of interest as much as possible to minimize the effects of the model structure on the modeled physical systems. This is a valid approach that has been used in countless climate studies using regional models. However, as is the case with all limited-area modeling, this is never perfect. For example, in the southeastern corners of the domains, where atmospheric flow is primarily easterly, we do not expect to see many model differences because the atmosphere hasn't interacted with the land surface (just the ocean) in those locations, and similarly, in the northwestern corners of the domains, the flow is primarily westerly, so we do not expect to see many differences. Also, the timescales of atmospheric motion relative to the domain suggest that it may take up to one month for the domain in certain fields to saturate, leaving little change after one month.

Further, in reviewing the simulations for Chapters 2 and 3, the responses are primarily local with very little change in continental-scale static stability, or in quasi-geostrophic relative vorticity, indicating that there are very few differences in the synoptic-scale regimes. This could be appropriately related to the surface forcing, or the lack of synoptic response could be associated with the limited-area modeling framework, but it is challenging to know which. The overlying issue in this regard, unfortunately, lies in computational cost. Land-atmosphere interactions are known

to occur on sub-seasonal to seasonal timescales, however, the characteristics of the land surface are represented more realistically at finer model resolutions. Therefore, these studies present a balance between high-resolution and long duration, making global models computationally expensive. The choice of using a limited-area model was a pragmatic one, despite the limitations.

Furthermore, coupled modeling such as is done in these simulations presents its general challenges. There are likely non-linear repercussions of changing single parameters (such as soil properties) without adjusting the whole system accordingly (i.e., adjusting vegetation, for instance). This is precisely why we endeavored to perform these studies. Soil parameters, which are thought to be mostly innocuous for the coupled climate system, can introduce substantial model uncertainty, as small changes in parameter values can lead to significant differences in longer term simulations—a common result in coupled system modeling. It is difficult to recognize a longer-timescale signal of the coupled system response vs. an artifact of coupled model error growth. While our goal was to analyze the coupled system responses specifically, this work would benefit from an understanding of the uncoupled land surface model responses to these changes as well. In this way, considering the discontinuity in spatial scales between atmospheric processes and land surface processes, coupled modeling presents certain challenges that are difficult to overcome. Nevertheless, a holistic view of how these parameters affect the coupled system response is an important finding for improved understanding, and it will motivate additional experiments utilizing both coupled and uncoupled models with various strategies.

5.2 Future Work

Despite the challenges reported here, we can improve the current land surface model structure that will allow for a simpler, more accurate representation of soil properties.

Commonly as has been shown, LSMs use look-up tables to connect soil hydro-physical properties to grid-assigned soil texture categories. The look-up table was implemented as an efficient way to provide horizontally varying soil parameters to an LSM. However, look-up tables provide a strong constraint on soil parameter heterogeneity. They restrict soils from varying within a soil texture category regionally, which is not uncommon given the broad category definitions.

A promising solution will be to remove the look-up table and soil texture assignments entirely from the model's structure. Instead, it is suggested to utilize soil hydro-physical parameter databases, which are now becoming available globally at high-resolution. Instead of rearranging soil texture during pre-processing, the new system could directly rearrange soil hydro-physical parameters, removing the soil texture/look-up table category confinement and allowing parameters to represent their regional characteristics more directly. I believe that this proposed solution is computationally plausible because the most intensive component is pre-processing, which only occurs before initiation. Because Noah-MP uses the same framework as the operational version of the Noah model, this improvement can be useful in operational NWP. Following implementation and sensitivity testing, this work could move into the NOAA R2O arena.

The proposed approach will follow a series of stages given below:

1. Pre-processing: Alter the Noah-MP Pre-processing System to accept and use soil hydro-physical parameter databases, rather than soil texture databases.

2. Noah-MP Code: Change Noah-MP model code to call soil parameters directly in subroutines, rather than calling the parameter table.

3. Testing: Conduct a series of sensitivity studies comparing the model physical structures across spatiotemporal scales, and in both coupled and uncoupled mode

4. Initiate R2O process.

5. Follow through to implementation.

It has been shown that soil texture and soil properties can affect surface fluxes, land-atmosphere interactions, and the atmospheric component of the water balance; therefore, I believe implementing an updated representation of soil properties can lead to improvements in model performance.

Appendix A:

A.1 Description of Community Land Model version 4 (CLMv4)

The following is a brief description of the Community Land Model Version 4 (hereafter, CLM), and its use of soil hydro-physical properties in equations that dictate the movement of moisture in the soil. For a full description please refer to the NCAR Technical Note: Oleson et al. [2013].

Figure A1 depicts the multitude of processes represented in the CLM modeling framework. This description will focus on soil processes, and specifically, the soil column's interaction with sub-surface moisture at above freezing temperatures. The following section is an adaptation of Section 7.4 in the above technical note.

A.2 Soil Water Physics

One-dimensional vertical flow of water in soils uses conservation of mass as

$$\frac{\delta\theta}{\delta t} = -\frac{\delta q}{\delta z} - Q \tag{A.1}$$

where θ is the volumetric soil water content (mm^3 mm^{-3}), t is time (s), z is height above a soil layer node in the soil column (mm) (positive upwards), q is soil water

flux (kg m^{-2} or mm s^{-1}) (positive upwards) and Q is a soil moisture sink term (mm mm^{-1} s^{-1}) (ET loss). This equation is solved by dividing the soil column into layers, and integrating downward in space and forward in time, with an upper boundary condition provided by infiltration flux into the top soil layer, and a lower boundary condition that depends on the depth of the water table.

The soil water flux q in Eq. A.1 can be described by Darcy's Law

$$q = -k\frac{\delta \Psi_h}{\delta z} \tag{A.2}$$

where k is the hydraulic conductivity (mm s^{-1}) and Ψ_h is the hydraulic potential (mm). The hydraulic potential is

$$\Psi_h = \Psi_m + \Psi_z \tag{A.3}$$

where Ψ_m is the soil matric potential (mm) (which is related to the adsorptive and capillary forces within the soil matrix), and Ψ_z is the gravitation potential (mm) (the vertical distance from an arbitrary reference elevation to a point in the soil). If the reference elevation is the soil surface, then $\Psi_z = z$. Letting $\Psi = \Psi_m$, Darcy's Law becomes

$$q = -k\left[\frac{\delta(\Psi + z)}{\delta z}\right]. \tag{A.4}$$

Darcy's equation can be further manipulated to yield

$$q = -k\left[\frac{\delta(\Psi + z)}{\delta z}\right] = -k\left(\frac{\delta \Psi}{\delta z} + 1\right) = -k\left(\frac{\delta \theta}{\delta z}\frac{\delta \Psi}{\delta \theta} + 1\right). \tag{A.5}$$

A substitution of Eq. A.5 into A.1, with Q=0 yields the Richards Equation

$$\frac{\delta\theta}{\delta t} = \frac{\delta}{\delta z}\left[k\left(\frac{\delta\theta}{\delta z}\frac{\delta\Psi}{\delta\theta}\right) + 1\right] \tag{A.6}$$

.

Zeng and Decker [2009] note that this θ-based version of the Richards Equation cannot maintain hydrostatic equilibrium due to truncation errors in the finite-difference numerical scheme. They show that this deficiency can be overcome by subtracting the equilibrium state from A.4 as

$$q = -k\left[\frac{\delta(\Psi + z - C)}{\delta z}\right] \tag{A.7}$$

where C is a constant hydraulic potential above the water table z_∇.

$$C = \Psi_E + z = \Psi_{sat}\left[\frac{\theta_E(z)}{\theta_{sat}}\right]^{-B} + z = \Psi_{sat} + z_\nabla \tag{A.8}$$

so that

$$q = -k\left[\frac{\delta(\Psi - \Psi_E)}{\delta z}\right] \tag{A.9}$$

where Ψ_E is the equilibrium soil matric potential (mm). Substituting A.9 into A.6 yield the modified Richards equation:

$$\frac{\delta\theta}{\delta t} = \frac{\delta}{\delta z}\left[k\frac{\delta(\Psi - \Psi_E)}{\delta z}\right] - Q \tag{A.10}$$

where the soil moisture sink term Q is included.

A.3 Implementation of Soil Hydro-physical Properties

In the WRF model, soil texture is assigned to each model gridspace during pre-processing (i.e., during execution of the WRF Pre-processing System, WPS). This system uses external soil texture databases to inform which soil texture categories occupy which grid spaces (a process described in Chapter 1). In this regard, the WRF version of CLM differs slightly from the CESM version of CLM. But, the general process is the same.

The hydraulic conductivity k_i (mm s^{-1}) and the soil matric potential Ψ_i (mm) for soil layer i vary with volumetric soil moisture θ_i and soil texture. According to the work of Clapp and Hornberger [1978], Cosby et al. [1984], and Campbell [1974] among others. Soil organic material is also accounted for in these equations, but it is beyond the scope of this description.

The hydraulic conductivity is defined at the depth of the interface of two adjacent layers $z_{h,i}$ and is a function of the saturated hydraulic conductivity $k_{sat}[z_{h,i}]$, and the liquid volumetric soil moisture of the two layers, θ_i and θ_{i+1}, given by:

$$k[z_{h,i}] = \begin{cases} k_{sat}[z_{h,i}] \left[\frac{0.5(\theta_i + \theta_{i+1})}{0.5(\theta_{sat,i} + \theta_{sat,i+1})} \right]^{2B_i+3} & 1 \leq i \leq N_{levsoi} - 1 \\ k_{sat}[z_{h,i}] \left(\frac{\theta_i}{\theta_{sat,i}} \right)^{2B_i+3} & i = N_{levsoi} \end{cases} \tag{A.11}$$

Soil Matric potential is defined at the node depth z_i of each layer i

$$\Psi_{m,i} = \Psi_{sat,i}\left(\frac{\theta_i}{\theta_{sat,i}}\right)^{-B_i} \geq -1 \times 10^8 \tag{A.12}$$

where $0.01 \leq \frac{\theta_i}{\theta_{sat,i}} \leq 1$.

In this case, Ψ_m in each soil layer follows the Cosby et al. [1984] formulation:

$$\Psi_m = \Psi_{sat}\left(\frac{\theta}{\theta_{sat}}\right)^{-b} \tag{A.13}$$

while, hydraulic conductivity, k, is from Campbell [1974], given by:

$$k = k_{sat}\left(\frac{\theta}{\theta_{sat}}\right)^{2b+3}. \tag{A.14}$$

See the diagram in Fig. A.2 for the locations of the definitions of matric potential and soil hydraulic conductivity.

A.4 Numerical Solution

Sub-surface water balance is given by:

$$\int_{-z_{h,i}}^{-z_{h,i-1}} \frac{\delta\theta}{\delta t} dz = \int_{-z_{h,i}}^{-z_{h,i-1}} \frac{\delta\theta}{\delta z} dz - \int_{-z_{h,i}}^{-z_{h,i-1}} Q dz \tag{A.15}$$

rearranging and taking the finite difference with time and evaluating implicitly at $t = n + 1$ yields,

$$\frac{\Delta z_i \Delta\theta_{liq,i}}{\Delta t} = -q_{i-1}^{n+1} + q_i^{n+1} - e_i \tag{A.16}$$

where $\Delta\theta_{liq,i} = \theta_{liq,i}^{n+1} - \theta_{liq,i}^{n}$ is the change in volumetric soil liquid water of layer i in time Δt and Δz_i is the thickness of layer i (mm).

The soil water fluxes in Eq. A.16, because of their dependence on hydraulic conductivity and soil matric potential, can be linearized about θ using a Taylor series expansion as

$$q_i^{n+1} = q_i^n + \frac{\delta q_i}{\delta \theta_{liq,i}} \Delta\theta_{liq,i} + \frac{\delta q_i}{\delta \theta_{liq,i+1}} \Delta\theta_{liq,i+1} \tag{A.17}$$

$$q_{i-1}^{n+1} = q_{i-1}^n + \frac{\delta q_{i-1}}{\delta \theta_{liq,i-1}} \Delta\theta_{liq,i-1} + \frac{\delta q_{i-1}}{\delta \theta_{liq,i}} \Delta\theta_{liq,i}. \tag{A.18}$$

Substituting Eq. A.17 and A.18, back in to A.16, yields a set of general tridiagonal equations of the form:

$$r_i = a_1 \Delta\theta_{liq,i-1} + b_i \Delta\theta_{liq,i} + c_i \Delta\theta liq, i+1 \tag{A.19}$$

where,

$$a_i = -\frac{\delta q_{i-1}}{\delta \theta_{liq,i-1}} \tag{A.20}$$

$$b_i = \frac{\delta q_i}{\delta \theta_{liq,i}} - \frac{\delta q_{i-1}}{\delta \theta_{liq,i}} - \frac{\Delta z_1}{\Delta t} \tag{A.21}$$

$$c_i = \frac{\delta q_i}{\delta \theta_{liq,i+1}} \tag{A.22}$$

$$r_i = q_{i-1}^n - q_i^n + e_i. \tag{A.23}$$

This set of equations is solved over layers $i = 1, ..., N_{levsoi} + 1$ where the layer $i = N_{levsoi} + 1$ is an aquifer representation.

From here, one can solve for the finite difference form of Eqs. A.20–A.23 using Eq. A.9, account for the boundaries of the general set of tridiagonal equations (i.e., the top soil layer, and the deepest layer before the aquifer), and incorporate the equilibrium matric potential, [See Oleson et al., 2013, , Sections 7.4.2.0–7.4.2.4]. After doing so, solving the set of appropriate tridiagonal equations following Pres et al. [1992] will update the liquid soil water as follows

$$w_{liq,i}^{n+1} = w_{liq,i}^n + \Delta\theta_{liq,i}\Delta z_i \tag{A.24}$$

where, $i = 1, ..., N_{levsoi}$. Volumetric soil water is

$$\theta_i = \frac{w_{liq,i}}{\Delta z_i \rho_{liq}}. \tag{A.25}$$

A.5 Surface Fluxes

Parts of the following are abbreviated from Section 5.1–5.4 of Oleson et al. [2013]. Surface sensible and latent heat fluxes in CLM are derived from a resistance formulation utilizing the Monin-Obukhov similarity theory. This section focuses only on the latent heat flux from bare soil surfaces. For a full description, the reader is

referred to the entire Technical Description Oleson et al. [2013].

In general, the surface latent heat fluxes from the bare soil can be written as

$$E = -\rho_{atm} \frac{(q_{atm} - q_s)}{r_{aw}} \tag{A.26}$$

where ρ_{atm} is the density of the atmosphere, q_{atm} is the atmospheric moisture content, q_s is the surface moisture content, and r_{aw} is the aerodynamic resistance with respect to water [see Oleson et al. [2013], their Eq. 5.57]. q_s in Eq. A26 can be written as

$$q_{soil} = \alpha_{soil} q_{sat}^{T_1} \tag{A.27}$$

with $q_{sat}^{T_1}$ representing the saturated specific humidity at the soil surface temperature T_1. α_{soil} can be given by:

$$\alpha_{soil} = exp\left(\frac{\Psi_1 g}{1 \times 10^3 R_{wv} T_1} \right) \tag{A.28}$$

an exponential term, dictated by Ψ_1, the soil water matric potential in the topmost soil layer, g the gravitation constant, and R_{wv} the gas constant for water vapor. Therefore, the soil matric potential and, by definition, the soil hydro-physical parameters play a direct role in calculating surface evaporation.

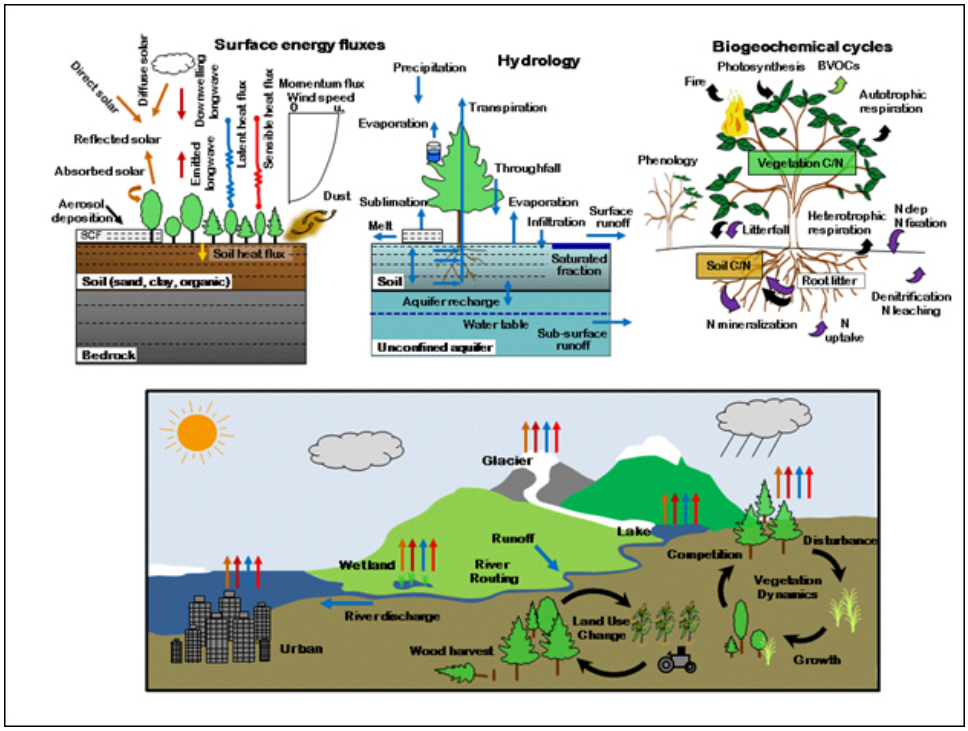

Figure A.1: A schematic depicting the complexity of processes that are represented in the CLM modeling framework. This schematic was borrowed from the NCAR's Online Description of CLM: (https://www.cesm.ucar.edu/models/clm/).

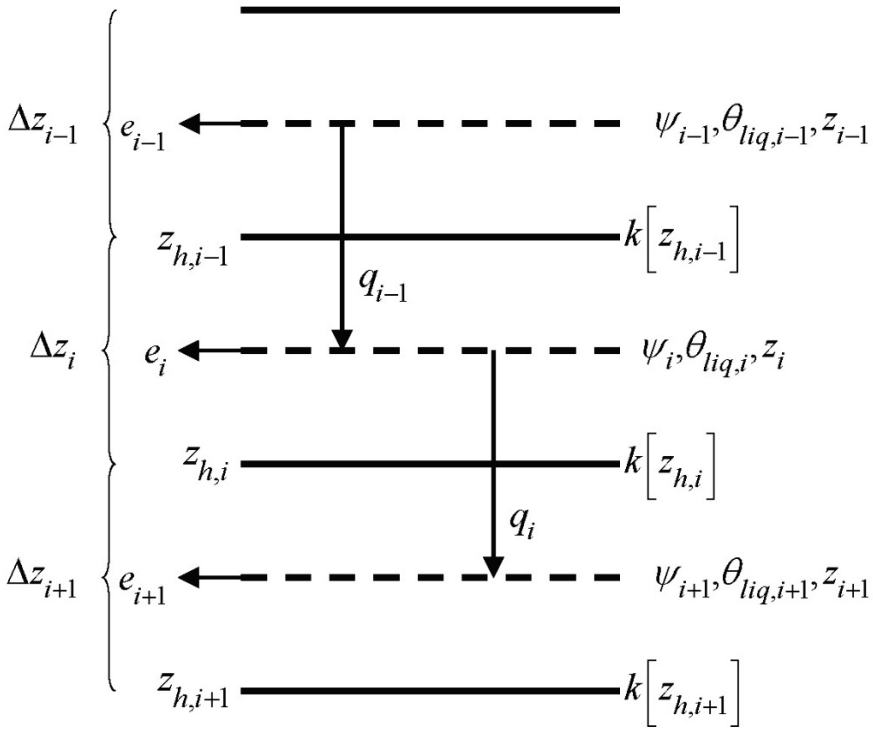

Figure A.2: Schematic diagram of the numerical scheme used to solve for soil water fluxes. Three soil layers, $i-1$, i, and $i+1$ are shown. The soil matric potential Ψ and volumetric soil moisture θ_{liq} are defined at the layer node depth z. The hydraulic conductivity $k[z_h]$ is defined at the interface of two layers z_h. The layer thickness is Δz. The soil water fluxes are q_{i-1} and q_i are defined as positive upwards. The soil moisture sink term e (ET loss) is defined as positive for flow out of the layer. This figure is adapted from Oleson et al. [2010], their Figure 7.3.

Appendix B:

This appendix was included in Dennis and Berbery [2021] as supplementary material supporting Chapter 1, Section 3.1: WRF Verification.

B.1 Comparison of WRF/CLM simulations with Livneh et al (2015)

Land surface models are particularly challenging to validate. In situ measurements often fall short in scale or duration. Quantities such as evapotranspiration (ET) are not directly measurable and are strongly dependent on parameterization schemes. On the other hand, soil moisture (SM) is considered a model-specific index [Koster et al., 2009]. Nevertheless, it is relevant for a study that does not employ any model calibration to be validated in its quality and realism. To do so, we will provide a comparison of the free-running WRF/CLM simulations used in this study to the long-term mean of a calibrated simulation reported by Livneh et al. [2015].

The Livneh et al. [2013] dataset is publicly available. It is a long-term, gridded dataset of surface meteorological observations and hydrologically-consistent land surface estimates. Livneh et al. [2015], hereafter L15, expanded this dataset to include Mexico, the conterminous US (CONUS), and southern Canada at 1/16° spatial resolution (about 6 km) from 1950–2013. L15 used the Variable Infiltration

Capacity (VIC) land surface model Liang et al. [1994] forced with the gridded surface meteorological data from Livneh et al. [2013]. VIC parameters were obtained from Livneh et al. [2013], who validated major river discharges over the CONUS region. The resulting calibrated and hydrologically-consistent dataset represents a reliable estimate of land surface states over the region of interest. It is thus suitable for WRF/CLM validation.

The WRF/CLM simulations are compared to the 2003–2013 averaged L15 dataset in terms of ET and normalized SM. Fig. B.1 shows the spatial patterns in ET (Figs. B.1a, c, e) and the normalized SM (Figs. B.1b, d, f) over the Mississippi River Basin. The ET maps reveal very similar patterns, with a gradient in values increasing from west to east, with maximums in all three maps approaching, and in few cases exceeding, 4.5 mm day^{-1}. There is a slight westward shift in higher values in L15 than the model simulations, but overall these products are very similar.

Directly comparing soil moisture is not possible because the VIC and CLM models' structures, equations, and parameters are not the same. Therefore, the comparison is focused on normalized total column soil moisture. Simple linear normalization is used, given by:

$$x_{norm} = (x - x_1)/(x_{99} - x_1), \tag{B.1}$$

Each model is normalized to its own range of values, reducing the dependence on parameters and structure. x_{99}, in this case, is the 99th percentile value of x, and x_1, is the first percentile. The use of percentiles reduces the impact of statistical

outliers in determining the normalization range.

It is evident that throughout the Midwest, the two CLM simulations (Figs. B.1b, and B.1d) are relatively moister compared to L15. The differences in soil moisture could be due to many reasons not to be discussed here. For instance, they could be the result of summer irrigation throughout the mid-western agriculture belt, or they could be an artifact of the years chosen for climatology. Regardless, the WRF/CLM simulations are similar to L15 in the overall pattern—increased wetness throughout the Midwest, a similar gradient as in the ET maps, leading to reduced relative wetness in the high plains along the Front Range of the Rocky Mountains.

The temporal evolution of both ET and normalized SM is assessed using monthly-averaged values over the Mississippi River Basin (Fig. B.2). The values of ET (Fig B.2a) indicate that the WRF/CLM simulations are quite similar to each other and also similar to the L15 ET values. In more than half of the sub-basins and in the full Mississippi River Basin, the difference between a WRF/CLM simulated ET and L15 ET is smaller than the difference between the two WRF/CLM simulations themselves (See Table S1). These results suggest that the range of values portrayed by the WRF/CLM simulations is reasonable, as defined by the L15 climatology.

The time series of normalized total column SM yields a somewhat different story. The model simulations are very similar to each other, suggesting that the soil texture categorization plays only a small role in normalized full column soil moisture. In all instances in Fig. B.2b, the model simulations are more relatively

moist than the L15 SM. The normalized scale, according to Eq B.1, is limited to values between about 0 and 1. Therefore, the differences between the models and L15 are about 15–20% of the normalized moisture range. These percentagewise differences between WRF/CLM SM and L15 SM are larger than what is shown in the ET analysis.

In conclusion, the unconstrained WRF/CLM model simulations, contrasted to a constrained and validated dataset, produce reasonable ET values in terms of spatial structure, multi-year basin-averages, and monthly time series. Evaluation of normalized SM is more challenging because values are model-specific. Nevertheless, comparing multi-year averages and monthly time series reveals that the differences in relative moisture are on the order of 10–15% of the wetness range.

Basin-averaged Evapotranspiration [mm day^{-1}]

Basin Name	WRF-STATSGO	WRF-GSDE	Livneh (2003–2013)
Arkansas	3.01	2.86	2.79
Ohio	4.36	3.91	3.71
Missouri	2.61	2.58	2.39
Upper Mississippi	3.25	3.11	3.41
Lower Mississippi	4.04	3.80	3.57
Full Mississippi	3.23	3.07	3.00

Normalized Full Column Soil Moisture [%]

Basin Name	WRF-STATSGO	WRF-GSDE	Livneh (2003–2013)
Arkansas	0.500	0.520	0.337
Ohio	0.670	0.645	0.524
Missouri	0.551	0.545	0.227
Upper Mississippi	0.541	0.561	0.334
Lower Mississippi	0.598	0.661	0.389
Full Mississippi	0.538	0.549	0.356

Table B.1: Shows the basin-averaged ET [mm day^{-1}] over the JJA 2016–2018 period for WRF-STATSGO, and WRF-GSDE, and for the JJA 2003–2013 for Livneh. It also shows the basin-averaged normalized full column soil moisture [%] over the JJA 2016–2018 period for WRF-STATSGO, and WRF-GSDE, and for the JJA 2003–2013 for Livneh. Arkansas, Ohio, Missouri, Upper Mississippi, and Lower Mississippi are sub-basins that constitue the Full Mississippi River Basin.

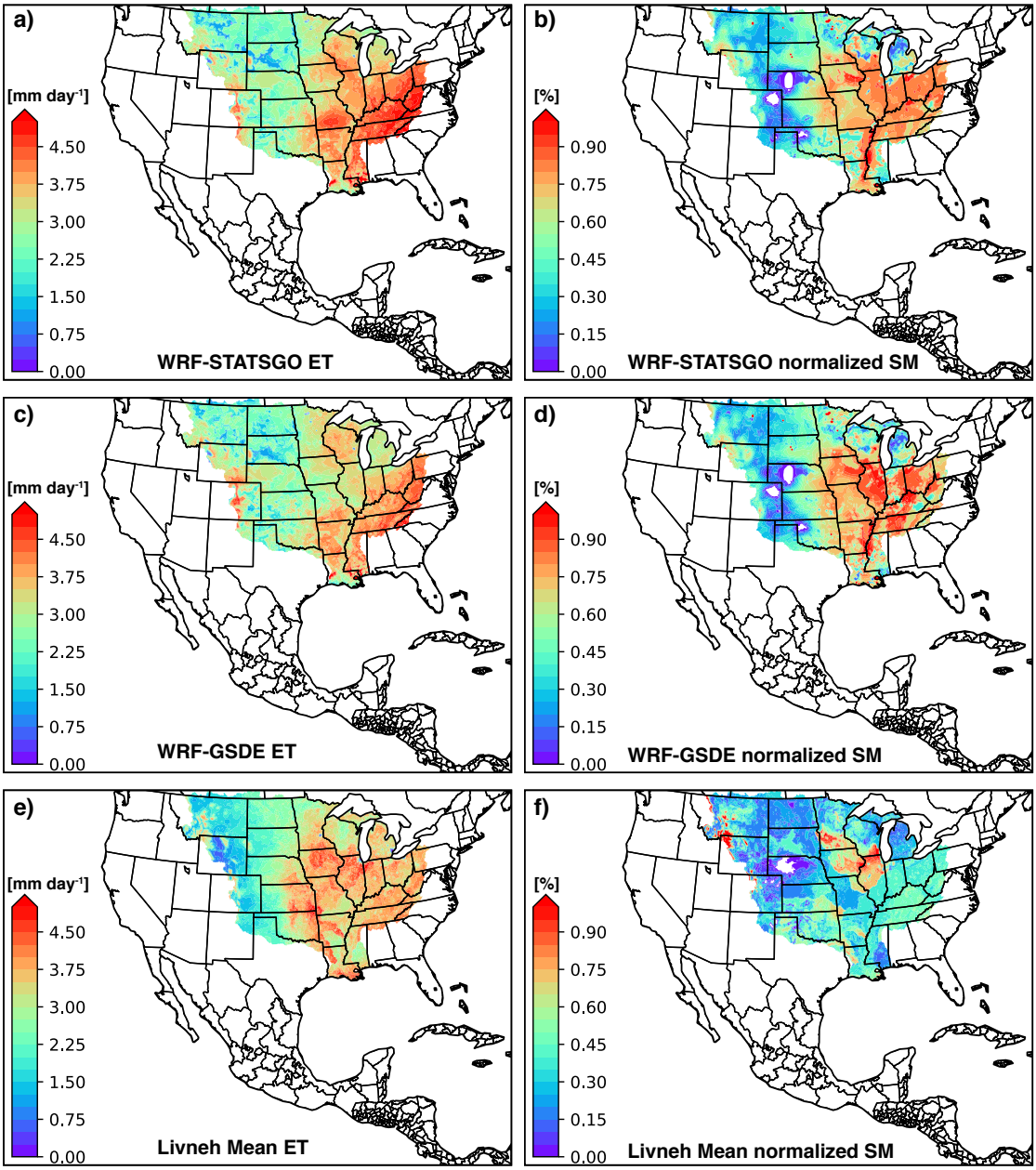

Figure B.1: Assigned top-layer soil categories for (a) WRF-USGS, (b) WRF-GSDE and (c) the seven most common transitions, as well as associated soil hydro-physical properties: Extractable water (d) for WRF-USGS, (e) WRF-GSDE, and (f) the differences (e - d); and the b-parameter (g) for WRF-USGS, (h) WRF-GSDE, and (i) the differences (h – g).

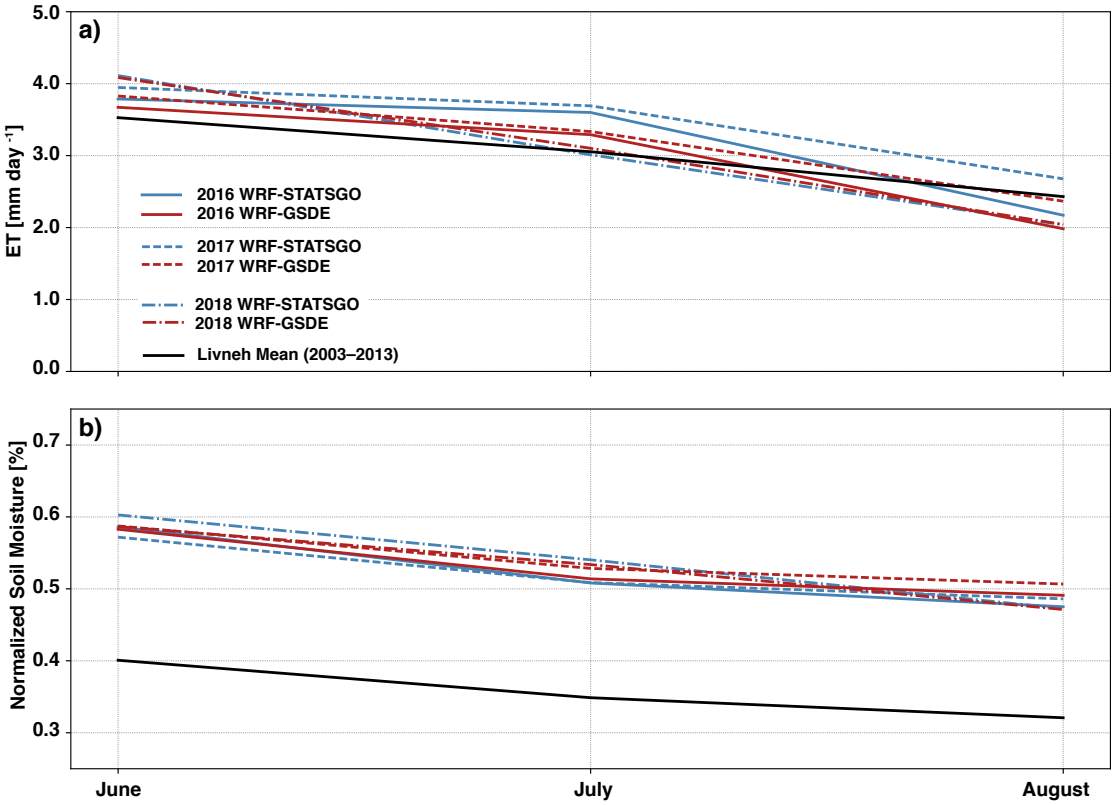

Figure B.2: Timeseries of (a) basin-averaged, monthly ET [mm day-1], and (b) basin-averaged normalized full column soil moisture [%] for (blue) WRF-STATSGO, (red), WRF-GSDE, and (black) L15 mean over the Mississippi River Basin. Solid colored lines are for the 2016 period, dashed lines represent 2017 and dash-dotted line indicate 2018. The solid black line represents L15 average for each variable (2003–2013).

Appendix C:

C.1 Description of Noah-MP

Noah-Multiple Physics (or Noah-MP) has evolved from the Noah land surface model improving on the existing physics, and providing numerous alternative physics packages to test in the original Noah LSM framework [Niu et al., 2011].

The Noah LSM came to life in the early 2000s [Ek, 2003] as a combination of existing land surface model components. Currently, the Noah LSM is used operationally for as the lower boundary condition in the Global Forecast System (GFS) and in other NCEP products. Its main functionality is depicted in schematic form in Fig. C.1. This section will describe the how the Noah-MP framework handles soil moisture transport within the soil column, how soil hydro-physical properties are implemented, and how surface fluxes are calculated in non-frozen non-vegetated conditions. The description is collected from numerous sources, including Chen and Dudhia [2001]; Chen et al. [1996, 1997]; Ek [2003]; Mahrt and Ek [1984]; Niu et al. [2011]; Pan and Mahrt [1987]; Shellito et al. [2016], among others.

C.2 Soil Hydraulics Functions and Soil Hydro-physical Properties

Noah-MP has 4 soil layers that increase in thickness with depth, and represents soil hydraulics, soil thermodynamics, root density, transpiration processes, snow physics, and canopy shading in very fine detail. The soil hydraulics are governed by a form of the Richards Equation [Richards, 1931], presented here as in Chen et al. [1996], and Shellito et al. [2016]:

$$\frac{\delta\theta}{\delta t} = \frac{\delta}{\delta z}\left[K\left(\frac{\delta\Psi}{\delta\theta}\right)\frac{\delta\theta}{\delta z}\right] + \frac{\delta K}{\delta z} + F_\theta \tag{C.1}$$

where θ is the volumetric soil moisture (m^3 m^{-3}), t is time (s), z is depth (m) F_θ represents the a net source/sink term (cm^3 cm^{-3} s^{-1}), including processes such as infiltration into and evaporation from the top soil layer, and transpiration from any root containing layers. K represents the Campbell [1974] variation of unsaturated hydraulic conductivity (m s^{-1}), and Ψ describes the matric potential (-cm) as is done in Cosby et al. [1984]. K and Ψ are given by,

$$K = K_{sat}\left(\frac{\theta}{\theta_s}\right)^{2b+3} \tag{C.2}$$

and

$$\Psi = \Psi_{sat}\left(\frac{\theta}{\theta_s}\right)^{-b}, \tag{C.3}$$

respectively. Eqs. C.2 and C.3 constitute the main pedotransfer functions that exist within the Noah-MP LSM. Those connect soil grain size, via certain parameters to

soil hydraulic functions. In Eqs. C.2 and C.3, K_{sat}, Ψ_{sat}, θ_s, and b, are empirically-derived, constant, soil hydro-physical properties, representing saturated hydraulic conductivity (m s^{-1}), saturated matric potential (-cm), porosity (m^3 m^{-3}), and a unitless curve fitting parameter, b, respectively.

Eq. C.1 is implemented in each of Noah-MP's four soil layers, following the general form,

$$d_{z_i}\frac{\delta\theta_i}{\delta t} = D\left(\frac{\delta\theta}{\delta z}\right)_{z_{i-1}} - D\left(\frac{\delta\theta}{\delta z}\right)_{z_i} + K_{z_{i-1}} - K_{z_i} - E_{t_i}, \tag{C.4}$$

with slightly different expressions for the top and bottom layers (See Fig C.2). i in Eq. C.4 refers to the soil layers, with $i = 1$ being the top most soil layer, increasing downwards. K is the conductivity, also accounting for the gravitational percolation downwards. D is diffusivity, given by $D = K(\delta\Psi/\delta\theta)$, a component of Eq. C.1.

C.3 Surface Fluxes

While, Noah-MP represents many versions of surface water fluxes (i.e., surface evaporation, canopy evaporation, canopy throughfall, and multiple representations of transpiration and stomatal resistance), this section will focus on only the soil's role in bare surface evaporation in the warm season.

Bare surface evaporation is given by:

$$E_{dir} = (1 - \sigma_f)\left(\frac{\theta_1 - \theta_{dry}}{\theta_{sat} - \theta_{dry}}\right)E_p \tag{C.5}$$

where, σ_f is the vegetation fraction, θ_1 is the top layer volumetric soil moisture, θ_{dry} is the wilting point, θ_s is the porosity, and E_p is potential evaporation calculated by a Penman-based energy balance approach, and a stability dependent aerodynamic resistance [Mahrt and Ek, 1984]. In this context, the soil hydro-physical properties are used to calculate top layer soil moisture content, and soil moisture content is used directly in calculating surface fluxes, therefore, soil hydro-physical properties can have a strong influence.

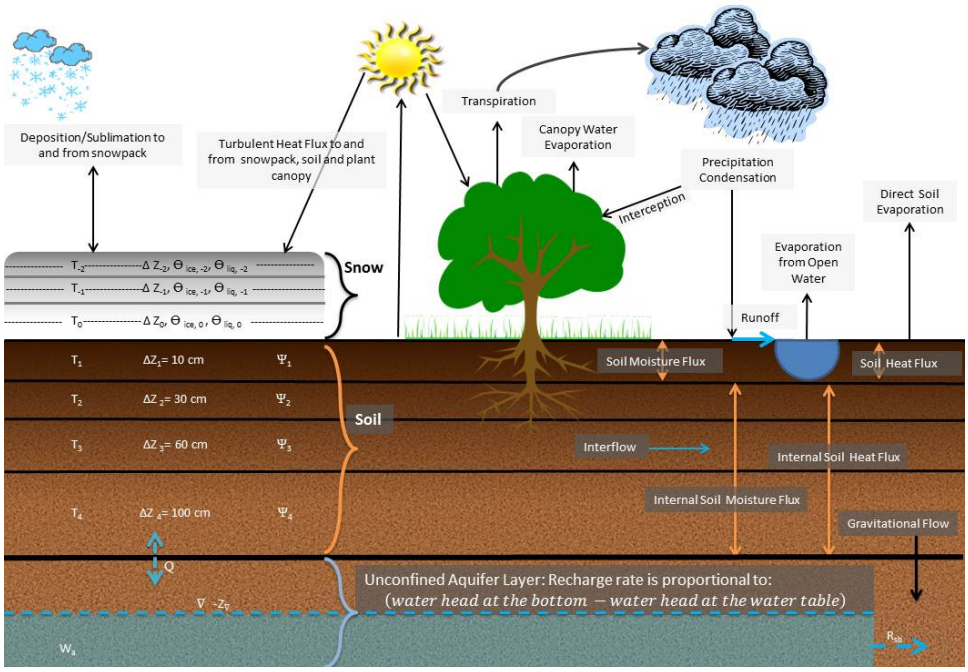

Figure C.1: A schematic depicting the major components of the Noah-MP land surface modeling suite. Borrowed from: https://www.jsg.utexas.edu/noah-mp/.

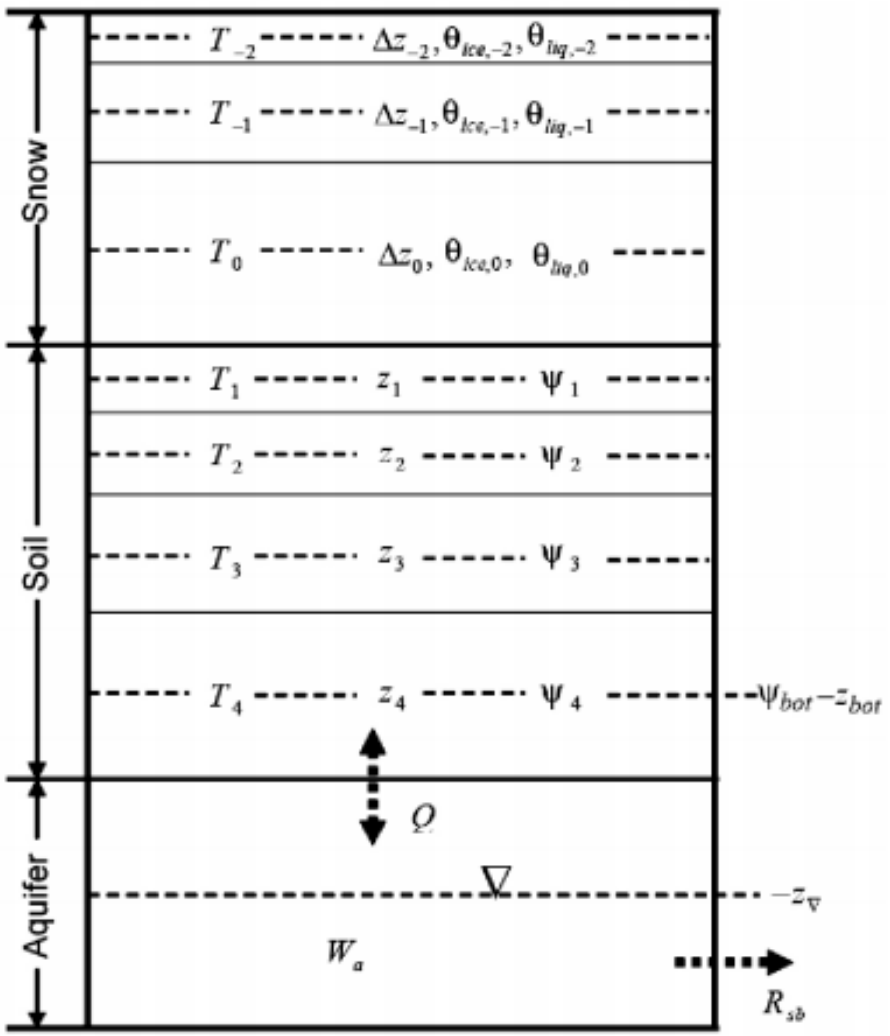

Figure C.2: A schematic diagram depicting the discretization of snow, soil, and aquifer layers in Noah-MP. Borrowed from Niu et al. [2011], their Fig. 2.

Bibliography

Aires, F., P. Gentine, K. L. Findell, B. R. Lintner, and C. Kerr, 2013: Neural Network-Based Sensitivity Analysis of Summertime Convection over the Continental United States. *J. Climate*, **27 (5)**, 1958–1979, doi:10.1175/JCLI-D-13-00161.1, URL http://journals.ametsoc.org/doi/10.1175/JCLI-D-13-00161.1.

Andersen, T. K., and J. M. Shepherd, 2014: A global spatiotemporal analysis of inland tropical cyclone maintenance or intensification. *International Journal of Climatology*, **34 (2)**, 391–402, doi:https://doi.org/10.1002/joc.3693, URL http://rmets.onlinelibrary.wiley.com/doi/abs/10.1002/joc.3693, _eprint: https://onlinelibrary.wiley.com/doi/pdf/10.1002/joc.3693.

Arsenault, K. R., G. S. Nearing, S. Wang, S. Yatheendradas, and C. D. Peters-Lidard, 2018: Parameter Sensitivity of the Noah-MP Land Surface Model with Dynamic Vegetation. *Journal of Hydrometeorology*, **19 (5)**, 815–830, doi:10.1175/jhm-d-17-0205.1, URL https://journals.ametsoc.org/view/journals/hydr/19/5/jhm-d-17-0205_1.xml, publisher: American Meteorological Society Section: Journal of Hydrometeorology.

Avissar, R., and Y. Liu, 1996: Three-dimensional numerical study of shallow convective clouds and precipitation induced by land surface forcing. *Journal of Geophysical Research: Atmospheres*, **101 (D3)**, 7499–7518, doi:https://doi.org/10.1029/95JD03031, URL https://agupubs.onlinelibrary.wiley.com/doi/abs/10.1029/95JD03031, _eprint: https://agupubs.onlinelibrary.wiley.com/doi/pdf/10.1029/95JD03031.

Bai, P., X. Liu, T. Yang, K. Liang, and C. Liu, 2016: Evaluation of streamflow simulation results of land surface models in GLDAS on the Tibetan plateau. *Journal of Geophysical Research: Atmospheres*, **121 (20)**, 12,180–12,197, doi:10.1002/2016JD025501, URL https://agupubs.onlinelibrary.wiley.com/doi/abs/10.1002/2016JD025501, _eprint: https://agupubs.onlinelibrary.wiley.com/doi/pdf/10.1002/2016JD025501.

Baur, F., C. Keil, and G. C. Craig, 2018: Soil moisture–precipitation coupling over Central Europe: Interactions between surface anomalies at different scales and

the dynamical implication. *Quarterly Journal of the Royal Meteorological Society*, **144 (717)**, 2863–2875, doi:10.1002/qj.3415, URL https://rmets.onlinelibrary.wiley.com/doi/abs/10.1002/qj.3415.

Berbery, E. H., 2003: Eta model estimated land surface processes and the hydrologic cycle of the Mississippi basin. *J Geophys Res*, **108**, 1–20, doi:10.1029/2002JD003192.

Berbery, E. H., and E. M. Rasmusson, 1999: Mississippi Moisture Budgets on Regional Scales. *Mon. Wea. Rev.*, **127 (11)**, 2654–2673, doi:10.1175/1520-0493(1999)127⟨2654:MMBORS⟩2.0.CO;2, URL http://journals.ametsoc.org/doi/full/10.1175/1520-0493(1999)127%3C2654%3AMMBORS%3E2.0.CO%3B2.

Betts, A. K., 2009: Land-Surface-Atmosphere Coupling in Observations and Models. *Journal of Advances in Modeling Earth Systems*, **1 (3)**, doi:10.3894/JAMES.2009.1.4, URL https://agupubs.onlinelibrary.wiley.com/doi/abs/10.3894/JAMES.2009.1.4, _eprint: https://agupubs.onlinelibrary.wiley.com/doi/pdf/10.3894/JAMES.2009.1.4.

Betts, A. K., and J. H. Ball, 1995: The FIFE surface diurnal cycle climate. *Journal of Geophysical Research: Atmospheres*, **100 (D12)**, 25 679–25 693, doi:10.1029/94JD03121, URL http://agupubs.pericles.prod.literatumonline.com/doi/abs/10.1029/94JD03121.

Biraud, S., M. Fischer, S. Chan, and M. Torn, 2020: AmeriFlux US-ARM ARM Southern Great Plains site- Lamont, Ver. 10-5. *AmeriFlux AMP*, doi:https://doi.org/10.17190/AMF/1246027.

Bonan, G. B., E. G. Patton, I. N. Harman, K. W. Oleson, J. J. Finnigan, Y. Lu, and E. A. Burakowski, 2018: Modeling canopy-induced turbulence in the Earth system: a unified parameterization of turbulent exchange within plant canopies and the roughness sublayer (CLM-ml v0). *Geoscientific Model Development*, **11 (4)**, 1467–1496, doi:10.5194/gmd-11-1467-2018, URL https://gmd.copernicus.org/articles/11/1467/2018/, publisher: Copernicus GmbH.

Bosilovich, M. G., and W.-y. Sun, 1998: Monthly Simulation of Surface Layer Fluxes and Soil Properties during FIFE. *Journal of the Atmospheric Sciences*, **55 (7)**, 1170–1184, doi:10.1175/1520-0469(1998)055⟨1170:MSOSLF⟩2.0.CO;2, URL https://journals.ametsoc.org/view/journals/atsc/55/7/1520-0469_1998_055_1170_msoslf_2.0.co_2.xml, publisher: American Meteorological Society Section: Journal of the Atmospheric Sciences.

Breuer, H., F. Ács, B. Laza, Á. Horváth, I. Matyasovszky, and K. Rajkai, 2012: Sensitivity of MM5-simulated planetary boundary layer height to soil dataset: comparison of soil and atmospheric effects. *Theor Appl Climatol*, **109 (3)**, 577–590, doi:10.1007/s00704-012-0597-y, URL https://doi.org/10.1007/s00704-012-0597-y.

Cai, X., Z.-L. Yang, Y. Xia, M. Huang, H. Wei, L. R. Leung, and M. B. Ek, 2014: Assessment of simulated water balance from Noah, Noah-MP, CLM, and VIC over CONUS using the NLDAS test bed. *Journal of Geophysical Research: Atmospheres*, **119 (24)**, 13,751–13,770, doi:10.1002/2014JD022113, URL http://agupubs.onlinelibrary.wiley.com/doi/abs/10.1002/2014JD022113, _eprint: https://onlinelibrary.wiley.com/doi/pdf/10.1002/2014JD022113.

Campbell, G. S., 1974: A Simple Method for Determinig Unsaturated Conductivity from Moisture Retention Data. *Soil Science*, **117 (6)**, 311, URL https://journals.lww.com/soilsci/Abstract/1974/06000/A_SIMPLE_METHOD_FOR_DETERMINING_UNSATURATED.1.aspx.

Chaney, N. W., and Coauthors, 2019: POLARIS Soil Properties: 30-m Probabilistic Maps of Soil Properties Over the Contiguous United States. *Water Resources Research*, **55 (4)**, 2916–2938, doi:10.1029/2018WR022797, URL https://agupubs.onlinelibrary.wiley.com/doi/abs/10.1029/2018WR022797, _eprint: https://agupubs.onlinelibrary.wiley.com/doi/pdf/10.1029/2018WR022797.

Chen, F., and J. Dudhia, 2001: Coupling an Advanced Land Surface–Hydrology Model with the Penn State–NCAR MM5 Modeling System. Part I: Model Implementation and Sensitivity. *Monthly Weather Review*, **129 (4)**, 569–585, doi:10.1175/1520-0493(2001)129⟨0569:CAALSH⟩2.0.CO;2, URL https://journals.ametsoc.org/view/journals/mwre/129/4/1520-0493_2001_129_0569_caalsh_2.0.co_2.xml, publisher: American Meteorological Society Section: Monthly Weather Review.

Chen, F., and Coauthors, 1996: Modeling of land surface evaporation by four schemes and comparison with FIFE observations. *Journal of Geophysical Research: Atmospheres*, **101 (D3)**, 7251–7268, doi:10.1029/95JD02165, URL http://doi.wiley.com/10.1029/95JD02165.

Chen, L., P. A. Dirmeyer, A. Tawfik, and D. M. Lawrence, 2017: Sensitivities of Land Cover–Precipitation Feedback to Convective Triggering. *Journal of Hydrometeorology*, **18 (8)**, 2265–2283, doi:10.1175/JHM-D-17-0011.1, URL https://journals.ametsoc.org/view/journals/hydr/18/8/jhm-d-17-0011_1.xml, publisher: American Meteorological Society Section: Journal of Hydrometeorology.

Chen, M., W. Shi, P. Xie, V. B. S. Silva, V. E. Kousky, R. W. Higgins, and J. E. Janowiak, 2008: Assessing objective techniques for gauge-based analyses of global daily precipitation. *Journal of Geophysical Research: Atmospheres*, **113 (D4)**, doi:https://doi.org/10.1029/2007JD009132, URL https://agupubs.onlinelibrary.wiley.com/doi/abs/10.1029/2007JD009132, _eprint: https://agupubs.onlinelibrary.wiley.com/doi/pdf/10.1029/2007JD009132.

Chen, T. H., and Coauthors, 1997: Cabauw experimental results from the Project for Intercomparison of Land-Surface Parameterization Schemes. *Journal of Climate*, **10 (6)**, 1194–1215, doi:10.1175/1520-0442(1997)010⟨1194:CERFTP⟩2.0.CO;2.

Clapp, R. B., and G. M. Hornberger, 1978: Empirical equations for some soil hydraulic properties. *Water Resources Research*, **14 (4)**, 601–604, doi:10.1029/WR014i004p00601.

Cosby, B. J., G. M. Hornberger, R. B. Clapp, and T. R. Ginn, 1984: A Statistical Exploration of the Relationships of Soil Moisture Characteristics to the Physical Properties of Soils. *Water Resources Research*, **20 (6)**, 682–690, doi:10.1029/WR020i006p00682, URL http://agupubs.onlinelibrary.wiley.com/doi/abs/10.1029/WR020i006p00682.

Cosgrove, B. A., and Coauthors, 2003: Real-time and retrospective forcing in the North American Land Data Assimilation System (NLDAS) project. *Journal of Geophysical Research: Atmospheres*, **108 (D22)**, doi:https://doi.org/10.1029/2002JD003118, URL https://agupubs.onlinelibrary.wiley.com/doi/abs/10.1029/2002JD003118, _eprint: https://agupubs.onlinelibrary.wiley.com/doi/pdf/10.1029/2002JD003118.

Cramer, W., and Coauthors, 2001: Global response of terrestrial ecosystem structure and function to CO2 and climate change: results from six dynamic global vegetation models. *Global Change Biology*, **7 (4)**, 357–373, doi:https://doi.org/10.1046/j.1365-2486.2001.00383.x, URL https://onlinelibrary.wiley.com/doi/abs/10.1046/j.1365-2486.2001.00383.x, _eprint: https://onlinelibrary.wiley.com/doi/pdf/10.1046/j.1365-2486.2001.00383.x.

Crook, N. A., 1996: Sensitivity of Moist Convection Forced by Boundary Layer Processes to Low-Level Thermodynamic Fields. *Mon. Wea. Rev.*, **124 (8)**, 1767–1785, doi:10.1175/1520-0493(1996)124⟨1767:SOMCFB⟩2.0.CO;2, URL http://journals.ametsoc.org/doi/10.1175/1520-0493%281996%29124%3C1767%3ASOMCFB%3E2.0.CO%3B2.

Cuntz, M., J. Mai, L. Samaniego, M. Clark, V. Wulfmeyer, O. Branch, S. Attinger, and S. Thober, 2016: The impact of standard and hard-coded parameters on the hydrologic fluxes in the Noah-MP land surface model. *Journal of Geophysical Research: Atmospheres*, **121 (18)**, 10,676–10,700, doi:10.1002/2016JD025097, URL http://agupubs.onlinelibrary.wiley.com/doi/abs/10.1002/2016JD025097, _eprint: https://onlinelibrary.wiley.com/doi/pdf/10.1002/2016JD025097.

Dai, Y., and Coauthors, 2019a: A Global High-Resolution Data Set of Soil Hydraulic and Thermal Properties for Land Surface Modeling. *Journal of Advances in Modeling Earth Systems*, **11 (9)**, 2996–3023, doi:https://doi.org/10.1029/2019MS001784, URL https://agupubs.onlinelibrary.wiley.com/doi/abs/10.1029/2019MS001784, _eprint: https://agupubs.onlinelibrary.wiley.com/doi/pdf/10.1029/2019MS001784.

Dai, Y., and Coauthors, 2019b: A review of the global soil property maps for Earth system models. *SOIL*, **5 (2)**, 137–158, doi:https://doi.org/10.5194/soil-5-137-2019, URL https://www.soil-journal.net/5/137/2019/.

Davis, R. O. E., and H. H. Bennett, 1927: Grouping of Soils on the Basis of Mechanical Analysis. *United States Department of Agriculture*, **419**, 1–15.

Dennis, E. J., and E. H. Berbery, 2021: The Role of Soil Texture in Local Land Surface–Atmosphere Coupling and Regional Climate. *Journal of Hydrometeorology*, **22 (2)**, 313–330, doi:10.1175/JHM-D-20-0047.1, URL https://journals.ametsoc.org/view/journals/hydr/22/2/jhm-d-20-0047.1.xml, publisher: American Meteorological Society Section: Journal of Hydrometeorology.

Dirmeyer, P. A., 2011: The terrestrial segment of soil moisture–climate coupling. *Geophysical Research Letters*, **38 (16)**, doi:10.1029/2011GL048268, URL http://agupubs.onlinelibrary.wiley.com/doi/abs/10.1029/2011GL048268.

Dirmeyer, P. A., G. Balsamo, E. M. Blyth, R. Morrison, and H. M. Cooper, 2021: Land-Atmosphere Interactions Exacerbated the Drought and Heatwave Over Northern Europe During Summer 2018. *AGU Advances*, **2 (2)**, e2020AV000 283, doi:https://doi.org/10.1029/2020AV000283, URL http://agupubs.onlinelibrary.wiley.com/doi/abs/10.1029/2020AV000283, _eprint: https://onlinelibrary.wiley.com/doi/pdf/10.1029/2020AV000283.

Dirmeyer, P. A., and S. Halder, 2017: Application of the Land–Atmosphere Coupling Paradigm to the Operational Coupled Forecast System, Version 2 (CFSv2). *J. Hydrometeor.*, **18 (1)**, 85–108, doi:10.1175/JHM-D-16-0064.1, URL https://journals.ametsoc.org/jhm/article/18/1/85/69829/Application-of-the-Land-Atmosphere-Coupling, publisher: American Meteorological Society.

Dirmeyer, P. A., R. D. Koster, and Z. Guo, 2006: Do Global Models Properly Represent the Feedback between Land and Atmosphere? *J. Hydrometeor.*, **7 (6)**, 1177–1198, doi:10.1175/JHM532.1, URL http://journals.ametsoc.org/jhm/article/7/6/1177/5462/Do-Global-Models-Properly-Represent-the-Feedback, publisher: American Meteorological Society.

Dirmeyer, P. A., C. A. Schlosser, and K. L. Brubaker, 2009: Precipitation, Recycling, and Land Memory: An Integrated Analysis. *Journal of Hydrometeorology*, **10 (1)**, 278–288, doi:10.1175/2008JHM1016.1, URL https://journals.ametsoc.org/view/journals/hydr/10/1/2008jhm1016_1.xml, publisher: American Meteorological Society Section: Journal of Hydrometeorology.

Dirmeyer, P. A., Z. Wang, M. J. Mbuh, and H. E. Norton, 2014: Intensified land surface control on boundary layer growth in a changing climate. *Geophysical Research Letters*, **41 (4)**, 1290–1294, doi:https://doi.org/10.1002/2013GL058826, URL https://agupubs.onlinelibrary.wiley.com/doi/abs/10.1002/2013GL058826, _eprint: https://agupubs.onlinelibrary.wiley.com/doi/pdf/10.1002/2013GL058826.

Duan, Q., and Coauthors, 2006: Model Parameter Estimation Experiment (MOPEX): An overview of science strategy and major results from the second and third workshops. *Journal of Hydrology*, **320 (1)**, 3–17, doi:10.1016/j.jhydrol.2005.07.031, URL http://www.sciencedirect.com/science/article/pii/S002216940500329X.

Duffková, R., 2013: *Influence of Soil Physical Properties and Terrain Relief on Actual Evapotranspiration in the Catchment with Prevailing Arable Land Determined by Energy Balance and Bowen Ratio*. IntechOpen, doi:10.5772/52810, URL https://www.intechopen.com/chapters/44339, publication Title: Evapotranspiration - An Overview.

Dy, C. Y., and J. C. H. Fung, 2016: Updated global soil map for the Weather Research and Forecasting model and soil moisture initialization for the Noah land surface model. *Journal of Geophysical Research: Atmospheres*, **121 (15)**, 8777–8800, doi:10.1002/2015JD024558, URL http://agupubs.onlinelibrary.wiley.com/doi/full/10.1002/2015JD024558.

Ek, M., and R. H. Cuenca, 1994: Variation in soil parameters: Implications for modeling surface fluxes and atmospheric boundary-layer development. *Boundary-Layer Meteorol*, **70 (4)**, 369–383, doi:10.1007/BF00713776, URL https://doi.org/10.1007/BF00713776.

Ek, M. B., 2003: Implementation of Noah land surface model advances in the National Centers for Environmental Prediction operational mesoscale Eta model. *Journal of Geophysical Research*, **108 (D22)**, 8851, doi:10.1029/2002JD003296, URL http://doi.wiley.com/10.1029/2002JD003296.

Eltahir, E. A. B., 1998: A Soil Moisture–Rainfall Feedback Mechanism: 1. Theory and observations. *Water Resources Research*, **34 (4)**, 765–776, doi:https://doi.org/10.1029/97WR03499, URL https://agupubs.onlinelibrary.wiley.com/doi/abs/10.1029/97WR03499, _eprint: https://agupubs.onlinelibrary.wiley.com/doi/pdf/10.1029/97WR03499.

Fan, Y., and H. van den Dool, 2008: A global monthly land surface air temperature analysis for 1948–present. *Journal of Geophysical Research: Atmospheres*, **113 (D1)**, doi:10.1029/2007JD008470, URL https://agupubs.onlinelibrary.wiley.com/doi/10.1029/2007JD008470.

FAO/UNSECO, 1971: The FAO-UNESCO soil map of the World. U. N. Educ.,Sci. Cultural Organ., Paris, France.

Ferguson, C. R., E. F. Wood, and R. K. Vinukollu, 2012: A Global Intercomparison of Modeled and Observed Land–Atmosphere Coupling. *J. Hydrometeor.*, **13 (3)**, 749–784, doi:10.1175/JHM-D-11-0119.1, URL https://journals.ametsoc.org/jhm/article/13/3/749/5579/A-Global-Intercomparison-of-Modeled-and-Observed, publisher: American Meteorological Society.

Findell, K. L., A. Berg, P. Gentine, J. P. Krasting, B. R. Lintner, S. Malyshev, J. A. Santanello, and E. Shevliakova, 2017: The impact of anthropogenic land use and land cover change on regional climate extremes. *Nat Commun*, **8 (1)**, 989, doi:10.1038/s41467-017-01038-w, URL http://www.nature.com/articles/s41467-017-01038-w, number: 1 Publisher: Nature Publishing Group.

Findell, K. L., and E. A. B. Eltahir, 1997: An analysis of the soil moisture-rainfall feedback, based on direct observations from Illinois. *Water Resources Research*, **33 (4)**, 725–735, doi:https://doi.org/10.1029/96WR03756, URL https://agupubs.onlinelibrary.wiley.com/doi/abs/10.1029/96WR03756, _eprint: https://agupubs.onlinelibrary.wiley.com/doi/pdf/10.1029/96WR03756.

Findell, K. L., and E. A. B. Eltahir, 2003: Atmospheric Controls on Soil Moisture–Boundary Layer Interactions. Part I: Framework Development. *J. Hydrometeor.*, **4 (3)**, 552–569, doi:10.1175/1525-7541(2003)004⟨0552:ACOSML⟩2.0.CO;2, URL http://journals.ametsoc.org/doi/full/10.1175/1525-7541%282003%29004%3C0552%3AACOSML%3E2.0.CO%3B2.

Fischer, E. M., S. I. Seneviratne, D. Lüthi, and C. Schär, 2007: Contribution of land-atmosphere coupling to recent European summer heat waves. *Geophysical Research Letters*, **34 (6)**, doi:https://doi.org/10.1029/2006GL029068, URL https://agupubs.onlinelibrary.wiley.com/doi/abs/10.1029/2006GL029068, _eprint: https://agupubs.onlinelibrary.wiley.com/doi/pdf/10.1029/2006GL029068.

Fisher, J. B., and Coauthors, 2017: The future of evapotranspiration: Global requirements for ecosystem functioning, carbon and climate feedbacks, agricultural management, and water resources. *Water Resources Research*, **53 (4)**, 2618–2626, doi:10.1002/2016WR020175, URL http://agupubs.onlinelibrary.wiley.com/doi/abs/10.1002/2016WR020175.

for Environmental Prediction/National Weather Service/NOAA/U.S. Department of Commerce, N. C., 2015: *NCEP GDAS/FNL 0.25 Degree Global Tropospheric Analyses and Forecast Grids*. Research Data Archive at the National Center for Atmospheric Research, Computational and Information Systems Laboratory, Boulder CO, URL https://doi.org/10.5065/D65Q4T4Z.

Gentine, P., D. Entekhabi, and J. Polcher, 2010: Spectral Behaviour of a Coupled Land-Surface and Boundary-Layer System. *Boundary-Layer Meteorol*, **134 (1)**, 157–180, doi:10.1007/s10546-009-9433-z, URL https://doi.org/10.1007/s10546-009-9433-z.

Gentine, P., D. Entekhabi, and J. Polcher, 2011: The Diurnal Behavior of Evaporative Fraction in the Soil–Vegetation–Atmospheric Boundary Layer Continuum. *Journal of Hydrometeorology*, **12 (6)**, 1530–1546, doi:10.1175/2011JHM1261.1, URL https://journals.ametsoc.org/view/journals/hydr/12/6/2011jhm1261_1.xml, publisher: American Meteorological Society Section: Journal of Hydrometeorology.

Gentine, P., A. A. M. Holtslag, F. D'Andrea, and M. Ek, 2013: Surface and Atmospheric Controls on the Onset of Moist Convection over Land. *J. Hydrometeor.*, **14 (5)**, 1443–1462, doi:10.1175/JHM-D-12-0137.1, URL http://journals.ametsoc.org/doi/10.1175/JHM-D-12-0137.1.

Godfrey, C. M., and D. J. Stensrud, 2008: Soil Temperature and Moisture Errors in Operational Eta Model Analyses. *J. Hydrometeor.*, **9 (3)**, 367–387, doi:10.1175/2007JHM942.1, URL https://journals.ametsoc.org/jhm/article/9/3/367/5802/Soil-Temperature-and-Moisture-Errors-in, publisher: American Meteorological Society.

He, J. J., Y. Yu, L. J. Yu, C. M. Yin, N. Liu, S. P. Zhao, and X. Chen, 2016: Effect of soil texture and hydraulic parameters on WRF simulations in summer in east China. *Atmospheric Science Letters*, **17 (10)**, 538–547, doi:10.1002/asl.690, URL https://rmets.onlinelibrary.wiley.com/doi/abs/10.1002/asl.690.

Hengl, T., and Coauthors, 2017: SoilGrids250m: Global gridded soil information based on machine learning. *PLOS ONE*, **12 (2)**, e0169 748, doi:10.1371/journal.pone.0169748, URL https://journals.plos.org/plosone/article?id=10.1371/journal.pone.0169748.

Hirsch, A. L., A. J. Pitman, J. Kala, R. Lorenz, and M. G. Donat, 2015: Modulation of Land-Use Change Impacts on Temperature Extremes via Land–Atmosphere Coupling over Australia. *Earth Interactions*, **19 (12)**, 1–24, doi:10.1175/EI-D-15-0011.1, URL https://journals.ametsoc.org/view/journals/eint/19/12/ei-d-15-0011.1.xml, publisher: American Meteorological Society Section: Earth Interactions.

Hobbs, J. A., 1941: Field Method for the Estimation of Soil Textures. *Journal of ASFMRA*, **5 (1)**, 24–31, URL https://www.jstor.org/stable/43757146.

Hohenegger, C., P. Brockhaus, C. S. Bretherton, and C. Schär, 2009: The Soil Moisture–Precipitation Feedback in Simulations with Explicit and Parameterized Convection. *Journal of Climate*, **22 (19)**, 5003–5020, doi:10.1175/2009JCLI2604.1, URL https://journals.ametsoc.org/view/journals/clim/22/19/2009jcli2604.1.xml, publisher: American Meteorological Society Section: Journal of Climate.

Holt, T. R., D. Niyogi, F. Chen, K. Manning, M. A. LeMone, and A. Qureshi, 2006a: Effect of Land–Atmosphere Interactions on the IHOP 24–25 May 2002 Convection Case. *Mon. Wea. Rev.*, **134 (1)**, 113–133, doi:10.1175/MWR3057.1, URL http://journals.ametsoc.org/doi/10.1175/MWR3057.1.

Holt, T. R., D. Niyogi, F. Chen, K. Manning, M. A. LeMone, and A. Qureshi, 2006b: Effect of Land–Atmosphere Interactions on the IHOP 24–25 May 2002 Convection Case. *Monthly Weather Review*, **134 (1)**, 113–133, doi:10.1175/MWR3057.1, URL https://journals.ametsoc.org/view/journals/mwre/134/1/mwr3057.1.xml, publisher: American Meteorological Society Section: Monthly Weather Review.

Holtan, H. N., C. B. England, G. P. Lawless, and G. A. Schumaker, 1968: Moisture-tension data for selected soils on experimental watersheds. URL https://agris.fao.org/agris-search/search.do?recordID=US201300317949, publisher: Agricultural Research Service, U.S. Dept. of Agriculture.

Iacono, M. J., J. S. Delamere, E. J. Mlawer, M. W. Shephard, S. A. Clough, and W. D. Collins, 2008: Radiative forcing by long-lived greenhouse gases: Calculations with the AER radia- tive transfer models. *Journal of Geophysical Research Atmospheres*, **113 (D13103)**, doi:10.1029/2008jd009944.

Janjić, Z. I., J. P. Gerrity Jr, and S. Nickovic, 2001: An alternative approach to nonhydrostatic modeling. *Monthly Weather Review*, **129 (5)**, 1164–1178.

Jia, G., and Coauthors, 2019: Land–climate interactions. In: Climate Change and Land: an IPCC special report on climate change, desertification, land degradation, sustainable land management, food security, and greenhouse gas fluxes in terrestrial ecosystems. *IPCC Special Report: Climate Change and Land*, IPCC, 133–247.

Kennedy, D., S. Swenson, K. W. Oleson, D. M. Lawrence, R. Fisher, A. C. L. d. Costa, and P. Gentine, 2019: Implementing Plant Hydraulics in the Community Land Model, Version 5. *Journal of Advances in Modeling Earth Systems*, **11 (2)**, 485–513, doi:10.1029/2018MS001500, URL https://agupubs.onlinelibrary.wiley.com/doi/abs/10.1029/2018MS001500.

Kim, C. P., and D. Entekhabi, 1998: Impact of soil heterogeneity in a mixed-layer model of the planetary boundary layer. *Hydrological Sciences Journal*, **43 (4)**, 633–658, doi:10.1080/02626669809492158, URL https://doi.org/10.1080/02626669809492158, publisher: Taylor & Francis _eprint: https://doi.org/10.1080/02626669809492158.

Kishné, A. S., Y. T. Yimam, C. L. S. Morgan, and B. C. Dornblaser, 2017: Evaluation and improvement of the default soil hydraulic parameters for the Noah Land Surface Model. *Geoderma*, **285**, 247–259, doi:10.1016/j.geoderma.2016.09.022, URL https://www.sciencedirect.com/science/article/pii/S0016706116304888.

Koster, R. D., Z. Guo, R. Yang, P. A. Dirmeyer, K. Mitchell, and M. J. Puma, 2009: On the Nature of Soil Moisture in Land Surface Models. *J. Climate*, **22 (16)**, 4322–4335, doi:10.1175/2009JCLI2832.1, URL http://journals.ametsoc.org/doi/10.1175/2009JCLI2832.1.

Koster, R. D., M. J. Suarez, and M. Heiser, 2000: Variance and Predictability of Precipitation at Seasonal-to-Interannual Timescales. *Journal of Hydrometeorology*, **1 (1)**, 26–46, doi:10.1175/1525-7541(2000)001⟨0026:VAPOPA⟩2.0.CO;2, URL http://journals.ametsoc.org/doi/abs/10.1175/1525-7541(2000)001%3C0026:VAPOPA%3E2.0.CO%3B2.

Koster, R. D., and Coauthors, 2004: Regions of Strong Coupling Between Soil Moisture and Precipitation. *Science*, **305 (5687)**, 1138–1140, doi:10.1126/science.1100217, URL http://science.sciencemag.org/content/305/5687/1138.

Koster, R. D., and Coauthors, 2006: GLACE: The Global Land–Atmosphere Coupling Experiment. Part I: Overview. *J. Hydrometeor.*, **7 (4)**, 590–610, doi:10.1175/JHM510.1, URL http://journals.ametsoc.org/doi/10.1175/JHM510.1.

Kumar, A., F. Chen, D. Niyogi, J. G. Alfieri, M. Ek, and K. Mitchell, 2011: Evaluation of a Photosynthesis-Based Canopy Resistance Formulation in the Noah Land-Surface Model. *Boundary-Layer Meteorol*, **138 (2)**, 263–284, doi:10.1007/s10546-010-9559-z, URL https://link.springer.com/article/10.1007/s10546-010-9559-z.

Kumar, S. V., and Coauthors, 2006: Land Information System: An interoperable framework for high resolution land surface modeling. *Environmental modelling & software*, **21 (10)**, 1402–1415.

Kusaka, H., and F. Kimura, 2004: Coupling a Single-Layer Urban Canopy Model with a Simple Atmospheric Model: Impact on Urban Heat Island Simulation for an Idealized Case. *undefined*, URL /paper/Coupling-a-Single-Layer-Urban-Canopy-Model-with-a-Kusaka-Kimura/f05217b95e12c3bdd640935f58ba3395f9f58c53.

Lannoy, G. J. M. D., R. D. Koster, R. H. Reichle, S. P. P. Mahanama, and Q. Liu, 2014: An updated treatment of soil texture and associated hydraulic properties in a global land modeling system. *Journal of Advances in Modeling Earth Systems*, **6 (4)**, 957–979, doi:10.1002/2014MS000330, URL https://agupubs.onlinelibrary.wiley.com/doi/abs/10.1002/2014MS000330.

Lawrence, D. M., P. E. Thornton, K. W. Oleson, and G. B. Bonan, 2007: The Partitioning of Evapotranspiration into Transpiration, Soil Evaporation, and Canopy Evaporation in a GCM: Impacts on Land–Atmosphere Interaction. *J. Hydrometeor.*, **8 (4)**, 862–880, doi:10.1175/JHM596.1, URL http://journals.ametsoc.org/jhm/article/8/4/862/69009/The-Partitioning-of-Evapotranspiration-into, publisher: American Meteorological Society.

Lawrence, D. M., and Coauthors, 2011: Parameterization improvements and functional and structural advances in Version 4 of the Community Land Model. *Journal of Advances in Modeling Earth Systems*, **3 (1)**, doi:10.1029/2011MS00045, URL https://agupubs.onlinelibrary.wiley.com/doi/abs/10.1029/2011MS00045.

Lawrence, D. M., and Coauthors, 2019: The Community Land Model Version 5: Description of New Features, Benchmarking, and Impact of Forcing Uncertainty. *Journal of Advances in Modeling Earth Systems*, **11 (12)**, 4245–4287, doi:10.1029/2018MS001583, URL http://agupubs.onlinelibrary.wiley.com/doi/abs/10.1029/2018MS001583.

Lee, J. M., Y. Zhang, and S. A. Klein, 2018: The Effect of Land Surface Heterogeneity and Background Wind on Shallow Cumulus Clouds and the Transition to Deeper Convection. *J. Atmos. Sci.*, **76 (2)**, 401–419, doi:10.1175/JAS-D-18-0196.1, URL https://journals.ametsoc.org/doi/full/10.1175/JAS-D-18-0196.1.

Lee, J. M., Y. Zhang, and S. A. Klein, 2019: The Effect of Land Surface Heterogeneity and Background Wind on Shallow Cumulus Clouds and the Transition to Deeper Convection. *Journal of the Atmospheric Sciences*, **76 (2)**, 401–419, doi:10.1175/JAS-D-18-0196.1, URL https://journals.ametsoc.org/view/journals/atsc/76/2/jas-d-18-0196.1.xml, publisher: American Meteorological Society Section: Journal of the Atmospheric Sciences.

Lee, S.-J., and E. H. Berbery, 2012: Land Cover Change Effects on the Climate of the La Plata Basin. *Journal of Hydrometeorology*, **13 (1)**, 84–102, doi:10.1175/JHM-D-11-021.1, URL https://journals.ametsoc.org/view/journals/hydr/13/1/jhm-d-11-021_1.xml, publisher: American Meteorological Society Section: Journal of Hydrometeorology.

Lee, S.-J., E. H. Berbery, and D. Alcaraz-Segura, 2013: The impact of ecosystem functional type changes on the La Plata Basin climate. *Adv. Atmos. Sci.*, **30 (5)**, 1387–1405, doi:10.1007/s00376-012-2149-x, URL https://doi.org/10.1007/s00376-012-2149-x.

Lehmann, P., O. Merlin, P. Gentine, and D. Or, 2018: Soil Texture Effects on Surface Resistance to Bare-Soil Evaporation. *Geophysical Research Letters*, **45 (19)**, 10,398–10,405, doi:https://doi.org/10.1029/2018GL078803, URL http://agupubs.onlinelibrary.wiley.com/doi/abs/10.1029/2018GL078803, _eprint: https://onlinelibrary.wiley.com/doi/pdf/10.1029/2018GL078803.

Li, L., W. Li, and A. P. Barros, 2013: Atmospheric moisture budget and its regulation of the summer precipitation variability over the Southeastern United States. *Clim Dyn*, **41 (3)**, 613–631, doi:10.1007/s00382-013-1697-9, URL https://doi.org/10.1007/s00382-013-1697-9.

Liang, X., D. P. Lettenmaier, E. F. Wood, and S. J. Burges, 1994: A simple hydrologically based model of land surface water and energy fluxes for general circulation models. *Journal of Geophysical Research: Atmospheres*, **99 (D7)**, 14 415–14 428, doi:https://doi.org/10.1029/94JD00483, URL https://agupubs.onlinelibrary.wiley.com/doi/abs/10.1029/94JD00483, _eprint: https://agupubs.onlinelibrary.wiley.com/doi/pdf/10.1029/94JD00483.

Liao, K.-H., L.-G. Lv, G.-S. Yang, and Q. Zhu, 2016: Sensitivity of simulated hillslope subsurface flow to rainfall patterns, soil texture and land use. *Soil Use and Management*, **32 (3)**, 422–432, doi:10.1111/sum.12282, URL http://onlinelibrary.wiley.com/doi/abs/10.1111/sum.12282, _eprint: https://onlinelibrary.wiley.com/doi/pdf/10.1111/sum.12282.

Livneh, B., T. J. Bohn, D. W. Pierce, F. Munoz-Arriola, B. Nijssen, R. Vose, D. R. Cayan, and L. Brekke, 2015: A spatially comprehensive, hydrometeorological data set for Mexico, the U.S., and Southern Canada 1950–2013. *Scientific Data*, **2 (1)**, 150 042, doi:10.1038/sdata.2015.42, URL https://www.nature.com/articles/sdata201542, number: 1 Publisher: Nature Publishing Group.

Livneh, B., E. A. Rosenberg, C. Lin, B. Nijssen, V. Mishra, K. M. Andreadis, E. P. Maurer, and D. P. Lettenmaier, 2013: A Long-Term Hydrologically Based Dataset of Land Surface Fluxes and States for the Conterminous United States: Update and Extensions. *Journal of Climate*, **26 (23)**, 9384–9392, doi:10.1175/JCLI-D-12-00508.1, URL https://journals.ametsoc.org/view/journals/clim/26/23/jcli-d-12-00508.1.xml, publisher: American Meteorological Society Section: Journal of Climate.

Lu, D., H. Wang, D. Huang, D. Li, and Y. Sun, 2020: Measurement and Estimation of Water Retention Curves Using Electrical Resistivity Data in Porous Media. *Journal of Hydrologic Engineering*, **25 (6)**, 04020 021, doi:10.1061/(ASCE)HE.1943-5584.0001925, URL https://ascelibrary.org/doi/abs/10.1061/%28ASCE%29HE.1943-5584.0001925, publisher: American Society of Civil Engineers.

Luo, Y., E. H. Berbery, K. E. Mitchell, and A. K. Betts, 2007: Relationships between Land Surface and Near-Surface Atmospheric Variables in the NCEP North American Regional Reanalysis. *J. Hydrometeor.*, **8 (6)**, 1184–1203, doi:10.1175/2007JHM844.1, URL https://journals.ametsoc.org/doi/full/10.1175/2007JHM844.1.

Mahmood, R., and Coauthors, 2010: Impacts of Land Use/Land Cover Change on Climate and Future Research Priorities. *Bulletin of the American Meteorological Society*, **91 (1)**, 37–46, doi:10.1175/2009BAMS2769.1, URL https://journals.ametsoc.org/view/journals/bams/91/1/2009bams2769_1.xml, publisher: American Meteorological Society Section: Bulletin of the American Meteorological Society.

Mahrt, L., and M. Ek, 1984: The Influence of Atmospheric Stability on Potential Evaporation. *J. Climate Appl. Meteor.*, **23 (2)**, 222–234, doi:10.1175/1520-0450(1984)023⟨0222:TIOASO⟩2.0.CO;2, URL http://journals.ametsoc.org.proxy-um.researchport.umd.edu/doi/abs/10.1175/1520-0450(1984)023%3C0222:TIOASO%3E2.0.CO%3B2.

Marshall, C. H., K. C. Crawford, K. E. Mitchell, and D. J. Stensrud, 2003: The Impact of the Land Surface Physics in the Operational NCEP Eta Model on Simulating the Diurnal Cycle: Evaluation and Testing Using Oklahoma Mesonet Data. *Wea. Forecasting*, **18 (5)**, 748–768, doi:10.1175/1520-0434(2003)018⟨0748:TIOTLS⟩2.0.CO;2, URL http://journals.ametsoc.org/waf/article/18/5/748/38626/The-Impact-of-the-Land-Surface-Physics-in-the, publisher: American Meteorological Society.

Martens, B., and Coauthors, 2017: GLEAM v3: satellite-based land evaporation and root-zone soil moisture. *Geoscientific Model Development*, **10**, 1903–1925, doi:10.5194/gmd-10-1903-2017, URL http://adsabs.harvard.edu/abs/2017GMD....10.1903M.

Matamala, R., 2019: AmeriFlux US-IB1 Fermi National Accelerator Laboratory-Batavia (Agricultural site), Ver. 8-5, AmeriFlux AMP, (Dataset). doi:https://doi.org/10.17190/AMF/1246065.

McDermid, S. S., C. Montes, B. I. Cook, M. J. Puma, N. Y. Kiang, and I. Aleinov, 2019: The Sensitivity of Land–Atmosphere Coupling to Modern Agriculture in the Northern Midlatitudes. *Journal of Climate*, **32 (2)**, 465–484, doi:10.1175/JCLI-D-17-0799.1, URL https://journals.ametsoc.org/view/journals/clim/32/2/jcli-d-17-0799.1.xml, publisher: American Meteorological Society Section: Journal of Climate.

Mesinger, F., and Coauthors, 2006: North American Regional Reanalysis. *Bulletin of the American Meteorological Society*, **87 (3)**, 343–360, doi:10.1175/BAMS-87-3-343, URL https://journals.ametsoc.org/view/journals/bams/87/3/bams-87-3-343.xml, publisher: American Meteorological Society Section: Bulletin of the American Meteorological Society.

Miralles, D. G., T. R. H. Holmes, R. A. M. D. Jeu, J. H. Gash, A. G. C. A. Meesters, and A. J. Dolman, 2011: Global land-surface evaporation estimated from satellite-based observations. *Hydrology and Earth System Sciences*, **15 (2)**, 453–469, doi:https://doi.org/10.5194/hess-15-453-2011, URL https://www.hydrol-earth-syst-sci.net/15/453/2011/hess-15-453-2011.html, publisher: Copernicus GmbH.

Montzka, C., M. Herbst, L. Weihermüller, A. Verhoef, and H. Vereecken, 2017: A global data set of soil hydraulic properties and sub-grid variability of soil water retention and hydraulic conductivity curves. *Earth System Science Data*, **9 (2)**, 529–543, doi:https://doi.org/10.5194/essd-9-529-2017, URL https://www.earth-syst-sci-data.net/9/529/2017/.

Mu, M., and Coauthors, 2021: Evaluating a land surface model at a water-limited site: implications for land surface contributions to droughts and heatwaves. *Hydrology and Earth System Sciences*, **25 (1)**, 447–471, doi:10.5194/hess-25-447-2021, URL https://hess.copernicus.org/articles/25/447/2021/, publisher: Copernicus GmbH.

Müller, O. V., P. L. Vidale, B. Vannière, R. Schiemann, R. Senan, R. J. Haarsma, and J. H. Jungclaus, 2021: Land–Atmosphere Coupling Sensitivity to GCMs Resolution: A Multimodel Assessment of Local and Remote Processes in the Sahel Hot Spot. *Journal of Climate*, **34 (3)**, 967–985, doi:10.1175/JCLI-D-20-0303.1, URL https://journals.ametsoc.org/view/journals/clim/34/3/JCLI-D-20-0303.1.xml, publisher: American Meteorological Society Section: Journal of Climate.

Nair, U. S., and Coauthors, 2019: Influence of Land Cover and Soil Moisture based Brown Ocean Effect on an Extreme Rainfall Event from a Louisiana Gulf Coast Tropical System. *Sci Rep*, **9 (1)**, 17 136, doi:10.1038/s41598-019-53031-6, URL http://www.nature.com/articles/s41598-019-53031-6, number: 1 Publisher: Nature Publishing Group.

Nakanishi, M., and H. Niino, 2006: An Improved Mellor–Yamada Level-3 Model: Its Numerical Stability and Application to a Regional Prediction of Advection Fog. *Boundary-Layer Meteorol*, **119 (2)**, 397–407, doi:10.1007/s10546-005-9030-8, URL https://doi.org/10.1007/s10546-005-9030-8.

Navale, A., C. Singh, S. Budakoti, and S. K. Singh, 2020: Evaluation of season long rainfall simulated by WRF over the NWH region: KF vs. MSKF. *Atmospheric Research*, **232**, 104 682, doi:10.1016/j.atmosres.2019.104682, URL http://www.sciencedirect.com/science/article/pii/S0169809519303904.

Nearing, G. S., D. M. Mocko, C. D. Peters-Lidard, S. V. Kumar, and Y. Xia, 2016: Benchmarking NLDAS-2 Soil Moisture and Evapotranspiration to Separate Uncertainty Contributions. *J. Hydrometeor.*, **17 (3)**, 745–759, doi:10.1175/JHM-D-15-0063.1, URL https://journals.ametsoc.org/jhm/article/17/3/745/6075/Benchmarking-NLDAS-2-Soil-Moisture-and, publisher: American Meteorological Society.

Niu, G.-Y., and Z.-L. Yang, 2004: Effects of vegetation canopy processes on snow surface energy and mass balances. *Journal of Geophysical Research: Atmospheres*, **109 (D23)**, doi:https://doi.org/10.1029/2004JD004884, URL https://agupubs.onlinelibrary.wiley.com/doi/abs/10.1029/2004JD004884, _eprint: https://agupubs.onlinelibrary.wiley.com/doi/pdf/10.1029/2004JD004884.

Niu, G. Y., and Coauthors, 2011: The community Noah land surface model with multiparameterization options (Noah-MP): 1. Model description and evaluation with local-scale measurements. *Journal of Geophysical Research Atmospheres*, **116 (12)**, 1–19, doi:10.1029/2010JD015139.

Novick, K., and R. Phillips, 2020: AmeriFlux US-MMS Morgan Monroe State Forest, Ver. 18-5, AmeriFlux AMP, (Dataset). doi:https://doi.org/10.17190/AMF/1246080.

NRCS Soil Survey Staff, USDA, 2012: General Soil Map (STATSGO2), Web Soil Survey. URL http://websoilsurvey.nrcs.usda.gov/.

Oleson, K., and Coauthors, 2013: Technical description of version 4.5 of the Community Land Model (CLM). Tech. rep., UCAR/NCAR, 5912 KB pp. doi:10.5065/D6RR1W7M, URL http://opensky.ucar.edu/islandora/object/technotes:515, artwork Size: 5912 KB Medium: application/pdf.

Oleson, K. W., and Coauthors, 2010: Technical Description of version 4.0 of the Community Land Model (CLM). *NCAR Technical Notes*, 266.

Or, D., and P. Lehmann, 2019: Surface Evaporative Capacitance: How Soil Type and Rainfall Characteristics Affect Global-Scale Surface Evaporation. *Water Resources Research*, **55 (1)**, 519–539, doi:10.1029/2018WR024050, URL http://agupubs.onlinelibrary.wiley.com/doi/abs/10.1029/2018WR024050, _eprint: https://onlinelibrary.wiley.com/doi/pdf/10.1029/2018WR024050.

Pan, H.-L., and L. Mahrt, 1987: Interaction between soil hydrology and boundary-layer development. *Boundary-Layer Meteorol*, **38 (1-2)**, 185–202, doi:10.1007/BF00121563, URL https://link.springer.com/article/10.1007/BF00121563.

Peters-Lidard, C. D., E. Blackburn, X. Liang, and E. F. Wood, 1998: The Effect of Soil Thermal Conductivity Parameterization on Surface Energy Fluxes and Temperatures. *Journal of the Atmospheric Sciences*, **55 (7)**, 1209–1224, doi:10.1175/1520-0469(1998)055⟨1209:TEOSTC⟩2.0.CO;2, URL https://journals.ametsoc.org/view/journals/atsc/55/7/1520-0469_1998_055_1209_teostc_2.0.co_2.xml, publisher: American Meteorological Society Section: Journal of the Atmospheric Sciences.

Prats, S. A., M. C. Malvar, and J. W. Wagenbrenner, 2021: Compaction and cover effects on runoff and erosion in post-fire salvage logged areas in the Valley Fire, California. *Hydrological Processes*, **35 (1)**, doi:10.1002/hyp.13997, URL https://onlinelibrary.wiley.com/doi/10.1002/hyp.13997.

Pres, W., S. Teukolsky, W. Vetterling, and B. Flannery, 1992: *Numerical Recipes in FORTRAN: The Art of Scientific Computing*. Cambridge University Press, New York.

Pugh, T. A. M., A. Arneth, S. Olin, A. Ahlström, A. D. Bayer, K. K. Goldewijk, M. Lindeskog, and G. Schurgers, 2015: Simulated carbon emissions from land-use change are substantially enhanced by accounting for agricultural management. *Environ. Res. Lett.*, **10 (12)**, 124 008, doi:10.1088/1748-9326/10/12/124008, URL https://doi.org/10.1088/1748-9326/10/12/124008, publisher: IOP Publishing.

Rasmusson, E. M., 1968: Atmospheric Water Vapor Transport and the Water Balance of North America: II. Large-Scale Water Balance Investigations. *Monthly Weather Review*, **96 (10)**, 720–734, doi:10.1175/1520-0493(1968)096⟨0720:AWVTAT⟩2.0.CO;2, URL https://journals.ametsoc.org/view/journals/mwre/96/10/1520-0493_1968_096_0720_awvtat_2_0_co_2.xml, publisher: American Meteorological Society Section: Monthly Weather Review.

Rawls, W. J., Y. A. Pachepsky, J. C. Ritchie, T. M. Sobecki, and H. Bloodworth, 2003: Effect of soil organic carbon on soil water retention. *Geoderma*, **116 (1)**, 61–76, doi:10.1016/S0016-7061(03)00094-6, URL http://www.sciencedirect.com/science/article/pii/S0016706103000946.

Reichle, R. H., and Coauthors, 2019: Version 4 of the SMAP Level-4 Soil Moisture Algorithm and Data Product. *Journal of Advances in Modeling*

Earth Systems, **11 (10)**, 3106–3130, doi:10.1029/2019MS001729, URL https://agupubs.onlinelibrary.wiley.com/doi/abs/10.1029/2019MS001729, _eprint: https://agupubs.onlinelibrary.wiley.com/doi/pdf/10.1029/2019MS001729.

Richards, L. A., 1931: Capillary conduction of liquids through porous mediums. *Physics*, **1 (5)**, 318–333, doi:10.1063/1.1745010.

Ritchie, J. T., 1981: Soil Water Availability. *Plant and Soil*, **58 (1/3)**, 327–338, URL https://www.jstor.org/stable/42933793.

Roads, J. O., S.-C. Chen, A. K. Guetter, and K. P. Georgakakos, 1994: Large-Scale Aspects of the United States Hydrologic Cycle. *Bulletin of the American Meteorological Society*, **75 (9)**, 1589–1610, doi:10.1175/1520-0477(1994)075⟨1589:LSAOTU⟩2.0.CO;2, URL https://journals.ametsoc.org/view/journals/bams/75/9/1520-0477_1994_075_1589_lsaotu_2_0_co_2.xml, publisher: American Meteorological Society Section: Bulletin of the American Meteorological Society.

Robock, A., and Coauthors, 2018: Evaluation of the North American Land Data Assimilation System over the southern Great Plains during the warm season. *Journal of Geophysical Research: Atmospheres*, doi:10.1029/2002JD003245@10.1002/(ISSN)2169-8996.GCIP3, URL http://agupubs.onlinelibrary.wiley.com/doi/full/10.1029/2002JD003245%4010.1002/%28ISSN%292169-8996.GCIP3, publisher: John Wiley & Sons, Ltd.

Roundy, J. K., C. R. Ferguson, and E. F. Wood, 2013: Temporal Variability of Land–Atmosphere Coupling and Its Implications for Drought over the Southeast United States. *Journal of Hydrometeorology*, **14 (2)**, 622–635, doi:10.1175/JHM-D-12-090.1, URL https://journals.ametsoc.org/view/journals/hydr/14/2/jhm-d-12-090_1.xml, publisher: American Meteorological Society Section: Journal of Hydrometeorology.

Roundy, J. K., and E. F. Wood, 2014: The Attribution of Land–Atmosphere Interactions on the Seasonal Predictability of Drought. *J. Hydrometeor.*, **16 (2)**, 793–810, doi:10.1175/JHM-D-14-0121.1, URL http://journals.ametsoc.org/doi/10.1175/JHM-D-14-0121.1.

Salamanca, F., A. Martilli, M. Tewari, and F. Chen, 2011: A Study of the Urban Boundary Layer Using Different Urban Parameterizations and High-Resolution Urban Canopy Parameters with WRF. *Journal of Applied Meteorology and Climatology*, **50 (5)**, 1107–1128, doi:10.1175/2010JAMC2538.1, URL https://journals.ametsoc.org/view/journals/apme/50/5/2010jamc2538.1.xml, publisher: American Meteorological Society Section: Journal of Applied Meteorology and Climatology.

Santanello, J. A., C. D. Peters-Lidard, A. Kennedy, and S. V. Kumar, 2012: Diagnosing the Nature of Land–Atmosphere Coupling: A Case Study of Dry/Wet Extremes in the U.S. Southern Great Plains. *Journal of Hydrometeorology*,

14 (1), 3–24, doi:10.1175/JHM-D-12-023.1, URL http://dx.doi.org/10.1175/JHM-D-12-023.1.

Santanello, J. A., C. D. Peters-Lidard, and S. V. Kumar, 2011: Diagnosing the Sensitivity of Local Land–Atmosphere Coupling via the Soil Moisture–Boundary Layer Interaction. *Journal of Hydrometeorology*, **12 (5)**, 766–786, doi:10.1175/JHM-D-10-05014.1, URL http://journals.ametsoc.org/doi/abs/10.1175/JHM-D-10-05014.1.

Santanello, J. A., C. D. Peters-Lidard, S. V. Kumar, C. Alonge, and W.-K. Tao, 2009: A Modeling and Observational Framework for Diagnosing Local Land-Atmosphere Coupling on Diurnal Time Scales. *Journal of Hydrometeorology*, **10 (3)**, 577–599, doi:10.1175/2009JHM1066.1, URL http://journals.ametsoc.org/doi/abs/10.1175/2009JHM1066.1.

Santanello, J. A., and Coauthors, 2018: Land–Atmosphere Interactions: The LoCo Perspective. *Bull. Amer. Meteor. Soc.*, **99 (6)**, 1253–1272, doi:10.1175/BAMS-D-17-0001.1, URL http://journals.ametsoc.org/doi/10.1175/BAMS-D-17-0001.1.

Sellers, P., and Coauthors, 1996: A Revised Land Surface Parameterization (SiB2) for Atmospheric GCMS. Part I: Model Formulation. *J. Climate*, **9 (4)**, 676–705, doi:10.1175/1520-0442(1996)009⟨0676:ARLSPF⟩2.0.CO;2, URL http://journals.ametsoc.org/doi/10.1175/1520-0442%281996%29009%3C0676%3AARLSPF%3E2.0.CO%3B2.

Seneviratne, S. I., T. Corti, E. L. Davin, M. Hirschi, E. B. Jaeger, I. Lehner, B. Orlowsky, and A. J. Teuling, 2010: Investigating soil moisture–climate interactions in a changing climate: A review. *Earth-Science Reviews*, **99 (3)**, 125–161, doi:10.1016/j.earscirev.2010.02.004, URL http://www.sciencedirect.com/science/article/pii/S0012825210000139.

Seth, A., and F. Giorgi, 1998: The Effects of Domain Choice on Summer Precipitation Simulation and Sensitivity in a Regional Climate Model. *Journal of Climate*, **11 (10)**, 2698–2712, doi:10.1175/1520-0442(1998)011⟨2698:TEODCO⟩2.0.CO;2, URL https://journals.ametsoc.org/view/journals/clim/11/10/1520-0442_1998_011_2698_teodco_2.0.co_2.xml, publisher: American Meteorological Society Section: Journal of Climate.

Shangguan, W., Y. Dai, Q. Duan, B. Liu, and H. Yuan, 2014: A global soil data set for earth system modeling. *Journal of Advances in Modeling Earth Systems*, **6 (1)**, 249–263, doi:10.1002/2013MS000293, URL http://agupubs.onlinelibrary.wiley.com/doi/abs/10.1002/2013MS000293.

Shellito, P. J., E. E. Small, and M. H. Cosh, 2016: Calibration of Noah Soil Hydraulic Property Parameters Using Surface Soil Moisture from SMOS and Basinwide In Situ Observations. *Journal of Hydrometeorology*, **17 (8)**, 2275–2292, doi:10.

1175/JHM-D-15-0153.1, URL https://journals.ametsoc.org/view/journals/hydr/17/8/jhm-d-15-0153_1.xml, publisher: American Meteorological Society Section: Journal of Hydrometeorology.

Shepherd, J. M., A. M. Thomas, J. A. Santanello, P. Lawston-Parker, and J. Basara, 2021: Evidence of warm core structure maintenance over land: a case study analysis of cyclone Kelvin. *Environ. Res. Commun.*, **3 (4)**, 045 004, doi:10.1088/2515-7620/abf39a, URL https://doi.org/10.1088/2515-7620/abf39a, publisher: IOP Publishing.

Singh, D., S. P. McDermid, B. I. Cook, M. J. Puma, L. Nazarenko, and M. Kelley, 2018: Distinct Influences of Land Cover and Land Management on Seasonal Climate. *Journal of Geophysical Research: Atmospheres*, **123 (21)**, 12,017–12,039, doi:https://doi.org/10.1029/2018JD028874, URL https://agupubs.onlinelibrary.wiley.com/doi/abs/10.1029/2018JD028874, _eprint: https://agupubs.onlinelibrary.wiley.com/doi/pdf/10.1029/2018JD028874.

Skamarock, W. C., and Coauthors, 2008: A Description of the Advanced Research WRF Version 3. *NCAR Technical Notes*, 125.

Smith, A., N. Lott, and R. Vose, 2011: The Integrated Surface Database: Recent Developments and Partnerships. *Bull. Amer. Meteor. Soc.*, **92 (6)**, 704–708, doi:10.1175/2011BAMS3015.1, URL https://journals.ametsoc.org/doi/abs/10.1175/2011BAMS3015.1.

Song, H.-J., C. R. Ferguson, and J. K. Roundy, 2015: Land–Atmosphere Coupling at the Southern Great Plains Atmospheric Radiation Measurement (ARM) Field Site and Its Role in Anomalous Afternoon Peak Precipitation. *J. Hydrometeor.*, **17 (2)**, 541–556, doi:10.1175/JHM-D-15-0045.1, URL http://journals.ametsoc.org/doi/10.1175/JHM-D-15-0045.1.

Song, Y. M., Z. F. Wang, L. L. Qi, and A. N. Huang, 2019: Soil Moisture Memory and Its Effect on the Surface Water and Heat Fluxes on Seasonal and Interannual Time Scales. *Journal of Geophysical Research: Atmospheres*, **124 (20)**, 10 730–10 741, doi:https://doi.org/10.1029/2019JD030893, URL https://agupubs.onlinelibrary.wiley.com/doi/abs/10.1029/2019JD030893, _eprint: https://agupubs.onlinelibrary.wiley.com/doi/pdf/10.1029/2019JD030893.

Sörensson, A. A., and E. H. Berbery, 2015: A Note on Soil Moisture Memory and Interactions with Surface Climate for Different Vegetation Types in the La Plata Basin. *Journal of Hydrometeorology*, **16 (2)**, 716–729, doi:10.1175/JHM-D-14-0102.1, URL https://journals.ametsoc.org/view/journals/hydr/16/2/jhm-d-14-0102_1.xml, publisher: American Meteorological Society Section: Journal of Hydrometeorology.

Sorooshian, S., R. Lawford, P. Try, W. Rossow, J. Roads, J. Polcher, S. Gilles, and R. Schiffer, 2005: Water and energy cycles: Investigating the links. *GEWEX Proceedings*, **54**, 58–64.

Stensrud, D. J., 2009: *Parameterization schemes keys understanding numerical weather prediction models*. Cambridge University Press.

Szabó, B., G. Szatmári, K. Takács, A. Laborczi, A. Makó, K. Rajkai, and L. Pásztor, 2019: Mapping soil hydraulic properties using random-forest-based pedotransfer functions and geostatistics. *Hydrology and Earth System Sciences*, **23 (6)**, 2615–2635, doi:10.5194/hess-23-2615-2019, URL https://hess.copernicus.org/articles/23/2615/2019/, publisher: Copernicus GmbH.

Tawfik, A. B., and P. A. Dirmeyer, 2014: A process-based framework for quantifying the atmospheric preconditioning of surface-triggered convection. *Geophysical Research Letters*, **41 (1)**, 173–178, doi:10.1002/2013GL057984, URL https://agupubs.onlinelibrary.wiley.com/doi/abs/10.1002/2013GL057984.

Thompson, G., P. R. Field, R. M. Rasmussen, and W. D. Hall, 2008: Explicit Forecasts of Winter Precipitation Using an Improved Bulk Microphysics Scheme. Part II: Implementation of a New Snow Parameterization. *Mon. Wea. Rev.*, **136 (12)**, 5095–5115, doi:10.1175/2008MWR2387.1, URL http://journals.ametsoc.org/doi/10.1175/2008MWR2387.1.

Trenberth, K. E., L. Smith, T. Qian, A. Dai, and J. Fasullo, 2007: Estimates of the Global Water Budget and Its Annual Cycle Using Observational and Model Data. *Journal of Hydrometeorology*, **8 (4)**, 758–769, URL https://www.jstor.org/stable/24911466, publisher: American Meteorological Society.

Tripathi, O. P., and F. Dominguez, 2013: Effects of spatial resolution in the simulation of daily and subdaily precipitation in the southwestern US. *Journal of Geophysical Research: Atmospheres*, **118 (14)**, 7591–7605, doi:https://doi.org/10.1002/jgrd.50590, URL https://agupubs.onlinelibrary.wiley.com/doi/abs/10.1002/jgrd.50590, _eprint: https://agupubs.onlinelibrary.wiley.com/doi/pdf/10.1002/jgrd.50590.

van Looy, K., and Coauthors, 2017: Pedotransfer Functions in Earth System Science: Challenges and Perspectives. *Reviews of Geophysics*, **55 (4)**, 1199–1256, doi:10.1002/2017RG000581, URL http://agupubs.onlinelibrary.wiley.com/doi/abs/10.1002/2017RG000581.

Vereecken, H., and Coauthors, 2016: Modeling Soil Processes: Review, Key Challenges, and New Perspectives. *Vadose Zone Journal*, **15 (5)**, vzj2015.09.0131, doi:https://doi.org/10.2136/vzj2015.09.0131, URL https://acsess.onlinelibrary.wiley.com/doi/abs/10.2136/vzj2015.09.0131, _eprint: https://acsess.onlinelibrary.wiley.com/doi/pdf/10.2136/vzj2015.09.0131.

Verhoef, A., and G. Egea, 2014: Modeling plant transpiration under limited soil water: Comparison of different plant and soil hydraulic parameterizations and preliminary implications for their use in land surface models. *Agricultural and Forest Meteorology*, **191**, 22–32, doi:10.1016/j.agrformet.2014.02.009, URL https://www.sciencedirect.com/science/article/pii/S0168192314000483.

Weaver, C. P., 2004: Coupling between Large-Scale Atmospheric Processes and Mesoscale Land–Atmosphere Interactions in the U.S. Southern Great Plains during Summer. Part II: Mean Impacts of the Mesoscale. *J. Hydrometeor.*, **5 (6)**, 1247–1258, doi:10.1175/JHM-397.1, URL http://journals.ametsoc.org/jhm/article/5/6/1247/5522/Coupling-between-Large-Scale-Atmospheric-Processes, publisher: American Meteorological Society.

Weckwerth, T. M., and D. B. Parsons, 2006: A Review of Convection Initiation and Motivation for IHOP_2002. *Mon. Wea. Rev.*, **134 (1)**, 5–22, doi:10.1175/MWR3067.1, URL http://journals.ametsoc.org/doi/full/10.1175/MWR3067.1.

Weihermüller, L., P. Lehmann, M. Herbst, M. Rahmati, A. Verhoef, D. Or, D. Jacques, and H. Vereecken, 2021: Choice of Pedotransfer Functions Matters when Simulating Soil Water Balance Fluxes. *Journal of Advances in Modeling Earth Systems*, **13 (3)**, e2020MS002 404, doi:https://doi.org/10.1029/2020MS002404, URL https://agupubs.onlinelibrary.wiley.com/doi/abs/10.1029/2020MS002404, _eprint: https://agupubs.onlinelibrary.wiley.com/doi/pdf/10.1029/2020MS002404.

Weil, R., and N. Brady, 2017: *Nature and Properties of Soils*. 15th ed., Pearson.

Welty, J., and X. Zeng, 2018: Does Soil Moisture Affect Warm Season Precipitation Over the Southern Great Plains? *Geophysical Research Letters*, **45 (15)**, 7866–7873, doi:10.1029/2018GL078598, URL http://agupubs.onlinelibrary.wiley.com/doi/abs/10.1029/2018GL078598.

Xia, Y., B. A. Cosgrove, M. B. Ek, J. Sheffield, L. Luo, E. F. Wood, K. Mo, and N. t. , 2013: Overview of the North American Land Data Assimilation System (NLDAS). *Land Surface Observation, Modeling and Data Assimilation*, WORLD SCIENTIFIC, 337–377, doi:10.1142/9789814472616_0011, URL https://www.worldscientific.com/doi/abs/10.1142/9789814472616_0011.

Xia, Y., M. T. Hobbins, Q. Mu, and M. B. Ek, 2015: Evaluation of NLDAS-2 evapotranspiration against tower flux site observations. *Hydrological Processes*, **29 (7)**, 1757–1771, doi:10.1002/hyp.10299, URL https://onlinelibrary.wiley.com/doi/abs/10.1002/hyp.10299, _eprint: https://onlinelibrary.wiley.com/doi/pdf/10.1002/hyp.10299.

Xia, Y., D. Mocko, M. Huang, B. Li, M. Rodell, K. E. Mitchell, X. Cai, and M. B. Ek, 2017: Comparison and Assessment of Three Advanced Land Surface Models in Simulating Terrestrial Water Storage Components over the United States. *Journal of Hydrometeorology*, **18 (3)**, 625–649, doi:10.1175/JHM-D-16-0112.1, URL https://journals.ametsoc.org/view/journals/hydr/18/3/jhm-d-16-0112_1.xml, publisher: American Meteorological Society Section: Journal of Hydrometeorology.

Xia, Y., and Coauthors, 2012: Continental-scale water and energy flux analysis and validation for North American Land Data Assimilation System project phase

2 (NLDAS-2): 2. Validation of model-simulated streamflow. *Journal of Geophysical Research: Atmospheres*, **117 (D3)**, doi:10.1029/2011JD016051, URL http://agupubs.onlinelibrary.wiley.com/doi/abs/10.1029/2011JD016051, _eprint: https://onlinelibrary.wiley.com/doi/pdf/10.1029/2011JD016051.

Xie, P., M. Chen, S. Yang, A. Yatagai, T. Hayasaka, Y. Fukushima, and C. Liu, 2007: A Gauge-Based Analysis of Daily Precipitation over East Asia. *Journal of Hydrometeorology*, **8 (3)**, 607–626, doi:10.1175/JHM583.1, URL https://journals.ametsoc.org/view/journals/hydr/8/3/jhm583_1.xml, publisher: American Meteorological Society Section: Journal of Hydrometeorology.

Yang, L., G. Sun, L. Zhi, and J. Zhao, 2018: Negative soil moisture-precipitation feedback in dry and wet regions. *Sci Rep*, **8 (1)**, 4026, doi:10.1038/s41598-018-22394-7, URL https://www.nature.com/articles/s41598-018-22394-7, number: 1 Publisher: Nature Publishing Group.

Yang, Z., and F. Dominguez, 2019: Investigating Land Surface Effects on the Moisture Transport over South America with a Moisture Tagging Model. *Journal of Climate*, **32 (19)**, 6627–6644, doi:10.1175/JCLI-D-18-0700.1, URL https://journals.ametsoc.org/view/journals/clim/32/19/jcli-d-18-0700.1.xml, publisher: American Meteorological Society Section: Journal of Climate.

Yin, J., J. D. Albertson, J. R. Rigby, and A. Porporato, 2015: Land and atmospheric controls on initiation and intensity of moist convection: CAPE dynamics and LCL crossings. *Water Resources Research*, **51 (10)**, 8476–8493, doi:https://doi.org/10.1002/2015WR017286, URL https://agupubs.onlinelibrary.wiley.com/doi/abs/10.1002/2015WR017286, _eprint: https://agupubs.onlinelibrary.wiley.com/doi/pdf/10.1002/2015WR017286.

Yun, Y., C. Liu, Y. Luo, X. Liang, L. Huang, F. Chen, and R. Rasmmusen, 2020: Convection-permitting regional climate simulation of warm-season precipitation over Eastern China. *Clim Dyn*, **54 (3)**, 1469–1489, doi:10.1007/s00382-019-05070-y, URL https://doi.org/10.1007/s00382-019-05070-y.

Zeng, X., and M. Decker, 2009: Improving the numerical solution of soil moisture-based Richards equation for land models with a deep or shallow water table. *Journal of Hydrometeorology*, **10 (1)**, 308–319, doi:10.1175/2008JHM1011.1, URL https://arizona.pure.elsevier.com/en/publications/improving-the-numerical-solution-of-soil-moisture-based-richards-, publisher: American Meteorological Society.

Zhang, D.-L., and X. Wang, 2003: Dependence of Hurricane intensity and structures on vertical resolution and time-step size. *Adv. Atmos. Sci.*, **20 (5)**, 711, doi:10.1007/BF02915397, URL https://doi.org/10.1007/BF02915397.

Zhang, D.-L., L. Zhu, X. Zhang, and V. Tallapragada, 2014: Sensitivity of Idealized Hurricane Intensity and Structures under Varying Background Flows and

Initial Vortex Intensities to Different Vertical Resolutions in HWRF. *Mon. Wea. Rev.*, **143 (3)**, 914–932, doi:10.1175/MWR-D-14-00102.1, URL http://journals.ametsoc.org/doi/10.1175/MWR-D-14-00102.1.

Zhang, Y., M. G. Schaap, and Y. Zha, 2018: A High-Resolution Global Map of Soil Hydraulic Properties Produced by a Hierarchical Parameterization of a Physically Based Water Retention Model. *Water Resources Research*, **54 (12)**, 9774–9790, doi:https://doi.org/10.1029/2018WR023539, URL http://agupubs.onlinelibrary.wiley.com/doi/abs/10.1029/2018WR023539, _eprint: https://onlinelibrary.wiley.com/doi/pdf/10.1029/2018WR023539.

Zheng, Y., N. A. Brunsell, J. G. Alfieri, and D. Niyogi, 2021: Impacts of land cover heterogeneity and land surface parameterizations on turbulent characteristics and mesoscale simulations. *Meteorol Atmos Phys*, doi:10.1007/s00703-020-00768-9, URL https://doi.org/10.1007/s00703-020-00768-9.

Zhuo, L., Q. Dai, D. Han, N. Chen, and B. Zhao, 2019: Assessment of simulated soil moisture from WRF Noah, Noah-MP, and CLM land surface schemes for landslide hazard application. *Hydrology and Earth System Sciences*, **23 (10)**, 4199–4218, doi:https://doi.org/10.5194/hess-23-4199-2019, URL https://www.hydrol-earth-syst-sci.net/23/4199/2019/, publisher: Copernicus GmbH.

Ziegler, C. L., and E. N. Rasmussen, 1998: The Initiation of Moist Convection at the Dryline: Forecasting Issues from a Case Study Perspective. *Weather and Forecasting*, **13 (4)**, 1106–1131, doi:10.1175/1520-0434(1998)013⟨1106:TIOMCA⟩2.0.CO;2, URL http://journals.ametsoc.org/doi/abs/10.1175/1520-0434%281998%29013%3C1106%3ATIOMCA%3E2.0.CO%3B2.